SHAPE STABILIZED COMPOSITE PHASE CHANGE MATERIALS FOR THERMAL ENERGY STORAGE SYSTEMS

MOHAMMAD MEHRALI

THESIS SUBMITTED IN FULFILMENT OF

THE REQUIREMENT FOR THE DEGREE OF

DOCTOR OF PHILOSOPHY

FACULTY OF ENGINEERING

UNIVERSITY OF MALAYA

KUALA LUMPUR

2015

UNIVERSITI MALAYA

ORIGINAL LITERARY WORK DECLARATION

Name of Candidate: MOHAMMAD MEHRALI

Registration/Matric No: KHA110105

Name of Degree: **DOCTOR OF PHILOSOPHY**

Title of Project Paper/Research Report/Dissertation/Thesis ("this Work"):

SHAPE STABILIZED COMPOSITE PHASE CHANGE MAERIALS FOR THERMAL ENERGY STORAGE SYSTEMS

Field of Study: **ADVANCE MATERIALS / NANOMATERIALS**

I do solemnly and sincerely declare that:

1. I am the sole author/writer of this Work;
2. This Work is original;
3. Any use of any work in which copyright exists was done by way of fair dealing and for permitted purposes and any excerpt or extract from, or reference to or reproduction of any copyright work has been disclosed expressly and sufficiently and the title of the Work and its authorship have been acknowledged in this Work;
4. I do not have any actual knowledge nor do I ought reasonably to know that the making of this work constitutes an infringement of any copyright work;
5. I hereby assign all and every rights in the copyright to this Work to the University of Malaya ("UM"), who henceforth shall be owner of the copyright in this Work and that any reproduction or use in any form or by any means whatsoever is prohibited without the written consent of UM having been first had and obtained;
6. I am fully aware that if in the course of making this Work I have infringed any copyright whether intentionally or otherwise, I may be subject to legal action or any other action as may be determined by UM.

Candidate's Signature Date

Subscribed and solemnly declared before,

Witness's Signature Date

Name:

Designa

ABSTRACT

Phase change materials (PCMs) used for the storage of thermal energy as sensible and latent heat are an important class of modern materials which substantially contribute to the efficient use and conservation of waste heat and solar energy. The storage of latent heat provides a greater density of energy storage with a smaller temperature difference between storing and releasing heat than the sensible heat storage method. The main problems with most inorganic PCM materials are their incongruent melting and supercooling effects. Organic PCMs have a high thermal storage capability and also other properties such as good thermal stability and little supercooling but their disadvantage during cooling is their low thermal conductivity below 0.3 W/(m K), which leads to the low heat storage/retrieval rates and low utilization efficiency of the stored energy. This study presents state of the art of shape-stabilized PCMs for thermal energy storage applications and provides an insight into our efforts to develop new shape stabilized PCMs (SSPCMs) with enhanced performance and safety. Specific attention was given to the improvement of thermal conductivity and shape stabilization procedures. In addition, the thermal energy storage properties and performance are discussed for solar energy applications. SSPCMs with nano composite structures have been systematically studied. A series of SSPCMs were fabricated by using the novel carbon nano materials. The carbon nano materials were divided into two groups: graphene materials and porous carbons. The novel graphene materials, including graphene oxide, reduced graphene oxide, nitrogen doped graphene and graphene nanoplatelets were used to prepare novel SSPCMs. The porous carbons like carbon nanospheres and activated carbon also were employed to prepare other SSPCMs. The structural, morphological and thermal features of the newly developed SSPCMs were evaluated by a series of modern instruments and characterization technologies, including DSC, TGA, FT-IR, Raman spectroscopy, TEM,

SEM, XRD and LFA. The thermal reliability of prepared SSPCMs was investigated using a thermal cycler for a large number of heating and cooling process. In this research, a novel type of SSPCMs by using graphene materials have shown excellent multifunctional thermal properties and thermal stabilities that are far beyond those of the conventional SSPCMs. The graphene materials have shown better performance compare to the porous carbons. The novel SSPCMs can be used to develop advanced smart materials and products with prosperous and promising applications in a number of industries.

ABSTRAK

Bahan perubah fasa (PCMS) yang diguna pakai untuk menyimpan tenaga haba dalam bentuk haba sentuhan teraruh dan terpendam adalah kelas yang penting daripada bahan-bahan moden yang menyumbang sebahagian besar kepada kecekapan penggunaan dan pengembalian haba buangan dan tenaga solar. Penyimpanan haba pendam menyediakan penyimpanan tenaga dengan ketumpatan yang lebih besar dengan perbezaan suhu yang lebih kecil antara menyimpan dan melepaskan haba berbanding kaedah penyimpanan haba sentuhan teraruh. Masalah utama dengan bahan-bahan PCM adalah peleburan dan penyejukan melampau yang tidak bersesuaian. PCMs organik mempunyai keupayaan penyimpanan haba yang tinggi dan juga sifat-sifat lain seperti kestabilan terma yang baik dan sedikit penyejukan melampau tetapi kelemahan mereka semasa penyejukan adalah kekonduksian terma rendah iaitu di bawah 0.4 W / (m K), yang membawa kepada kadar penyimpanan atau pengembalian semula haba yang rendah dan kecekapan penggunaan tenaga yang rendah bagi haba yang disimpan.Kajian ini mempersembahkan kesenian baru bagi penstabilan-bentuk PCMS untuk aplikasi penyimpanan tenaga haba dan memberi perspektif mendalam bagi usaha membangunkan penstabilan-bentuk PCMS (SSPCMs) yang baru dengan prestasi dan keselamatan yang dipertingkatkan. Perhatian khusus diberikan kepada peningkatan kekonduksian terma dan prosedur penstabilan bentuk. Di samping itu, ciri-ciri penyimpanan tenaga haba dan prestasi dibincangkan untuk aplikasi tenaga suria.SSPCMs dengan struktur komposit nano telah dikaji secara sistematik. Satu siri SSPCMs telah direka dengan menggunakan bahan karbon nano yang baru. Bahan-bahan nano karbon telah dibahagikan kepada dua kumpulan: bahan graphene dan karbon berliang. Bahan-bahan graphene baru termasuk oksida graphene, penyahoksidaan graphene, nitrogen graphene yang didopankan dan nanoplatlet graphene telah digunakan untuk menyediakan SSPCMs yang baru. Karbon berliang seperti karbon nanosphera dan karbon diaktifkan juga telah digunakan untuk

menyediakan SSPCMs lain.Ciri-ciri struktur, morfologi dan terma SSPCMs yang baru dibangunkan telah dinilai menggunakan satu siri instrumen dan teknologi pencirian yang moden, termasuk DSC, TGA, FT-IR, spektroskopi Raman, TEM, SEM, XRD dan LFA. Keutuhan terma SSPCMs yang disediakan telah disiasat dengan menggunakan kitaran haba untuk jumlah pemanasan dan proses penyejukan yang besar. Dalam kajian ini, SSPCMs baru yang menggunakan bahan-bahan graphene telah menunjukkan sifat haba pelbagai fungsi yang sangat baik dan kestabilan haba yang jauh mengatasi SSPCMs konvensional. Bahan-bahan graphene telah menunjukkan prestasi yang lebih baik berbanding dengan karbon berliang. SSPCMs baru boleh digunakan untuk membangunkan bahan pintar yang canggih dan produk dengan aplikasi yang berpotensi cerah dalam pelbagai industri.

ACKNOWLEDGEMENT

I give all praise and thanks to Allah, the most merciful, who has given me the strength health and inspiration for completing this thesis.

I am deeply indebted to my supervisors, Associate Prof. Dr. Hendrik Simon Cornelis Metselaar and Dr Amalina for their constant guidance of this research project and thesis. Working with them have been a great experience.

I would like to thank to my wife Sara for her patience and support during my study. I would like to thank to my lovely brother Mr. Mehdi Mehrali for the useful discussions and helps, which we experienced in all steps of my study. Also, valuable helps from Mr Emad Sadeghinezhad and staff members are greatly appreciated.

I would also like to convey thanks to the University of Malaya, Bright Sparks Unit and Ministry of Higher Education (MOHE) of Malaysia, Grant number UM.C/HIR/MOHE/ENG/21, for providing the financial support and laboratory facilities.

Lastly but not the least, I would like to dedicate my love and deepest appreciation to my family especially my parents. Thank you for your help and excellent advice.

TABLE OF CONTENTS

LIST OF FIGURES

LIST OF TABLES

LIST OF SYMBOLS AND ABBREVIATIONS

Nomenclature

ΔH	latent heat
A	Area
C_p	specific heat
cm	Centimeter
g	Gram
k	Thermal conductivity
K	Kelvin
L	Length
M	Molar
mL	Milliliters
mm	Millimeter
Q	Heat
q	Magnitude of heat transmission
wt%	Weight percentage

Greek symbols

eφ	Spectrometer work function
Θ	Degree
α	Thermal diffusivity
ρ	Density

Subscripts

c	Calculated value
f	Freezing
m	Melting

p	Peak
t	Transition

Acronyms

AC	Activated carbon
AFM	Atomic force microscopy
ATR	Attenuated total reflectance
BE	Binding energy
BET	Brunauer, emmett and teller
CA	Capric acid
CNS	Carbon nanospheres
DP	Dropping point
DSC	Differential scanning calorimetry
DTG	Derivative thermogravimetric analyses
EG	Expanded graphite
EP	Expanded perlite
EVA	Ethylene–vinyl acetate
FESEM	Field emission scanning electron microscopy
FT-IR	Fourier transmittance infrared spectra
GNP	Graphene nanoplatelets
GO	Graphene oxide
HDPE	High density polythene
IFR	Intumescent flame retardant
KE	Kinetic energy

LFA	Laser flash analysis
LHS	Latent heat storage
LHTESS	Latent heat thermal energy storage systems
MA	Myristic acid
MFM	Magnetic force microscope
NDG	Nitrogen doped graphene
OMT	Organically-modified montmorillonite
PA	Palmitic acid
PCM	Phase change material
PE	Polyethylene
PEG	Polyethylene glycol
PET	Poly(ethylene terephthalate)
PMMA	Poly methyl methacrylate
PU	Polyurethane
RGO	Reduced graphene oxide
SA	Stearic acid
SS	Stearyl stearate
SSPCM	Shape stabilized phase change material
TEM	Transmission electron microscopy
TES	Thermal energy storage
TG	Thermal gravimetry
THW	Transient hot-wire
UV	Uv-vis spectroscopy
VMT	Vermiculite
XPS	X-ray photoelectron spectroscopy
XRD	X-ray diffractometry

CHAPTER 1
INTRODUCTION

1.1 Background

There has been a considerable increase in the levels of greenhouse gases due to large scale industrialization, in the last 150 years. Carbon dioxide being one of the main components of these gases has had an atmospheric emission of approximately 347 billion tons since 1751 from the consumption of fossil fuels and cement production(Nkwetta & Haghighat, 2014). Fossil fuels are combusted to generate electricity, fuel transportation and for heating and cooling purposes. Fossil fuels are a significant energy source, but they are depleting and their combustion is adversely affecting the climate. Experts around the world have warned that greenhouse gases have to be reduced globally, up to 50% in the next 50-100 years (Tatsidjodoung et al., 2013). This has generated an increased interest in renewable energy from natural sources, like wind, sunlight, hydropower as well as alternatives like nuclear and geothermal energy. Efforts are being made by scientists, engineers and policy makers worldwide, to develop, commercialize and deploy renewable energy technologies. Solar energy is one of the most promising renewable energy sources that is abundantly and freely available. The International Energy Agency has estimated that solar power will produce almost 21% of the world's electricity by 2050 (Frankl & Nowak, 2010). However, there are numerous problems that have to be resolved to successfully utilize solar energy. The intensity of solar radiation varies according to the time of the day, weather condition such as cloud cover; location and the season. This intermittent nature of the solar energy creates a mismatch between the energy supply and demand. This is where energy storage comes into play. Solar energy can be stored in various forms such as hydrogen energy storage, electrochemical storage and thermal energy storage (TES)(Goswami et al., 2000). The advantages of energy storage include

leveling supply with demand, improving the performance of energy systems and increasing the reliability. Without an energy storage system, the annual solar load fraction is low wherein a backup system or auxiliary energy meets the major energy load. This leads to increased consumption of fuels (Garg et al., 1985). These problems can be overcome by storing thermal energy when solar radiance is available abundantly and used whenever it is required. The excess heat from solar radiation during the daytime can be collected and stored for use during the night time. This is especially useful in the areas of heat recovery systems and electricity generation, where the energy availability and utilization periods are different (Farid et al., 2004). In the case of electricity consumption, the load varies drastically according to the time of the day. This is a crucial issue in locations which have extremely cold or hot climate, where space heating and cooling (e.g. air conditioning) is the main cause of such variation. TES is used to store the energy generated during off-peak hours to meet the demand during peak hours, which leads to a more efficient power distribution (Farid et al., 2004). Thus, TES is critical to the success of solar energy applications. Apart from the utility applications, TES also has its uses in active and passive solar heating, water heating and building heating and cooling. The benefits of TES are:

- Saving of fossil fuels,
- Increasing plant efficiency,
- Load leveling.

1.2 Importance of the Study

There are three types of TES systems, namely, sensible heat storage systems, latent heat storage systems and thermochemical systems. However, due to a lack of certainty in physio-chemical and thermodynamic properties, the use of chemical storage is highly limited. In sensible heat systems, energy is stored in materials as the temperature rises,

and this stored energy is utilized when it is released during temperature decrease whereas latent heat storage systems utilize the stored energy during phase change. The most common sensible heat storage materials in use today are rock, concrete and others. However, some of its disadvantages include low energy density, bulky storage system, high range of operating temperature which reduces plant efficiency (Hawlader et al., 2003). On the other hand, latent heat storage materials can store a large amount of energy in a small volume and can operate at an almost constant or extremely small range of temperature. This can be illustrated when sensible heat capacity of rock which is 2.326 kJ/kg K is compared with the latent heat capacity of calcium chloride hexahydrate which is 193 kJ/kg (Khudhair & Farid, 2004).These latent heat storage materials are known as phase change materials (PCMs). Due to this inherent property of PCMs, they make very promising candidates as storage materials for solar applications and are being researched extensively throughout the world. A few favorable characteristics of PCMs are listed below (Dincer & Dost, 1996).

- Heat storage is over a narrow range of temperature. Thus, thermal stratification is not mandatorily considered in the design.
- They make strong candidates in passive storage due to their isothermal nature.
- They store a considerably higher amount of energy per unit volume as compared to sensible heat storage materials.

1.3 Research Problem Statement

There are a wide variety of PCMs available which melt and solidify at a broad range of temperatures and are utilized in many applications. One of the most widely used low temperature PCMs is paraffin wax, which is cheap and has moderate thermal conductivity values. Salts are higher temperature materials with higher volumetric energy

density and thermal conductivity. Other materials which have been studied in the last several decades are fatty acids and eutectics of organic and inorganic materials. Though these PCMs have properties that make them attractive for storage applications, not all PCMs possess all the properties which would make them ideal for any application. Different materials have different drawbacks, which includes, low thermal conductivity, high cost, subcooling, phase segregation, volumetric expansion, poor stability at extended temperature cycling and so on (Farid et al., 2004). Many techniques have been investigated and applied to overcome the limitations. Some of these methods are adding nucleating agents, thickening agents, stabilizers, additives to reduce subcooling and phase segregation; metal and matrix, and fillers, finned tubes to increase the heat transfer rate (Khudhair & Farid, 2004). When the costs of encapsulation and those related to the increase of PCM conductivity are analyzed, the increasing attention being given to the development of form–stable, shape stabilized, composite materials, is clearly the rational approach. In a shape stabilized composite the nanofiller prevents leakage of the molten PCM from the composite at temperatures above the melting temperature of the PCM. Various materials are applied as matrices in shape-stabilized PCMs and they are described along with new form-stable composite PCMs in the following sub-chapters.

1.4 Objective of Present Work

The aim of the present work is to investigate low cost methods and materials for shape stabilizing medium temperature phase change materials, for thermal energy storage applications. The project will focus on the fabrication, characterization, structures and properties of shape stabilized composite PCMs. In the study, efforts will concentrate on the following areas including:

- To characterize the structural features of the shape stabilized composite PCMs prepared by using different carbon additives with different loading rate.

- To investigate the thermal behavior of SSPCMs in terms of latent heat enthalpy, super-cooling, crystallization, melting features, thermal conductivity and etc.
- To study the relationship between structural features, physical properties and mechanisms involved.
- To investigate the thermal reliability and chemical stability of prepared SSPCMs for high number of thermal cycling process.

1.5 Thesis Structure

The entire work is presented as five chapters in this thesis and the gist of them is provided below. Chapter 1 provides an introduction which portrays the importance of solar energy and gives a general overview of the research work. Chapter 2 gives a literature review on the thermal energy storage, performance enhancement techniques, PCMs and shape stabilization of PCMs for latent heat thermal energy storage systems (LHTES). Chapter 3 includes preparation of composite PCMs and various characterization methods adopted for evaluation the shape stabilized PCMs. Chapter 4 describes the experimental results and discussions on the prepared form-stable PCMs. Chapter 5 gives a summary and conclusion of the current work and recommendations for future work.

CHAPTER 2

LITERATURE REVIEW

The energy crisis and global warming have become serious concerns, thus, outstanding attempts have been made for the efficient utilization of alternative energy, like solar energy. Nevertheless, the fluctuation of solar radiation makes latent heat thermal energy storage (LHTES) indispensable within the solar thermal energy applications. Phase change materials (PCMs) are recognized to become critical for LHTES since they can store and release considerable amounts of latent heat during their phase transition for efficient utilization of thermal energy (Moreno et al., 2014; Rathod & Banerjee, 2013; Tay et al., 2013b). PCMs are usually categorized into organic and inorganic materials based on their components. Organic PCMs have obtained extensive attention because of their higher latent heat density, suitable phase-transition temperature and stable physical and chemical properties (Amin et al., 2014; Castell et al., 2011; Mahmoud et al., 2013; Pitié et al., 2013). The pure organic PCMs possess some shortcomings that hinder their application in practice, including low thermal conductivity, high volume change and liquid seepage during phase transition. There are several strategies to eliminate these particular difficulties such as encapsulation and shape stabilization of PCMs (Tahan Latibari et al., 2013; Tahan Latibari et al., 2014). Nowadays, form-stable PCM composites with good thermal conductive supporting materials which could maintain the solid shape even if the temperature is more than the melting point of PCMs have become the main focus of scientific studies (Fang et al., 2010; Zeng et al., 2013; Zhong et al., 2013). This method is among the most effective ways to resolve the leakage and low thermal conductivity problems of PCMs.

This study reviews the present state of the art of phase change materials for thermal energy storage applications and provides a deep insight into recent efforts to develop new

PCMs showing enhanced performance and safety. Specific attention is given to the improvement of thermal conductivity and shape stabilization procedures, as well as flame retarding properties. The broad range of PCM applications in the industries is presented and future research directions are outlined.

2.1 Thermal Energy Storage (TES)

Thermal energy storage occurs when heat is either added or removed from a storage medium. Examples of TES are found everywhere. Hot water that is used for household heating is a form of TES, as are ice used for cooling, hot and cold packs, and the hot rocks used in saunas. In all of these examples, the object undergoes a temperature change, which causes a change in the enthalpy of the medium. This change in enthalpy corresponds to the amount of thermal energy that has been stored or removed from the medium. TES is divided into three major classifications; sensible heat storage, latent heat storage, and chemical storage.

2.1.1 Sensible Heat Storage

The most common form of TES is that of sensible heat storage. Sensible heat storage takes advantage of the mass of the material, the temperature difference that the material is exposed to, and the appropriate heat capacity of the material depending on the state of the material. With sensible heat storage, there is no phase change in the material during the energy storage process. Some common materials that are used for sensible heat storage include rocks, bricks, water, and oils. An example of sensible heat storage is that of a hot water bottle. The amount of heat stored is a function of the specific heat of the medium, the temperature change and the mass of storage medium as it's represented by the following equation(Zalba et al., 2003):

$$Q = \int_{T_i}^{T_f} mC_p \,.\, dT = mC_{ap}(T_f - T_i) \qquad (2\text{-}1)$$

Where Q(J)-quantity of heat stored, T_i(℃)-initial temperature, T_f (℃)-final temperature, m(kg)- mass of heat storage medium, C_p (J/kg K)-specific heat , C_{ap}(J/kg K)-average specific heat between T_i and T_f.The storage materials absorb heat by the conventional heat transfer mechanisms of radiation, conduction and convection. However, a drawback of using sensible heat storage alone as the method of TES is the large volume of material needed ($10^6 m^3$) to store and release the required amounts of energy over the large time intervals experienced at CSP plants, in the order of 100MWe for over six hours(Hasnain, 1998).

2.1.2 Latent Heat Storage

To decrease the volume of material required when using sensible heat storage alone, one could utilize the latent heat of phase change. Unlike sensible heat storage, which requires a temperature difference, latent heat storage occurs at a constant temperature while the material is undergoing a phase change as shown in Figure 2-1 .

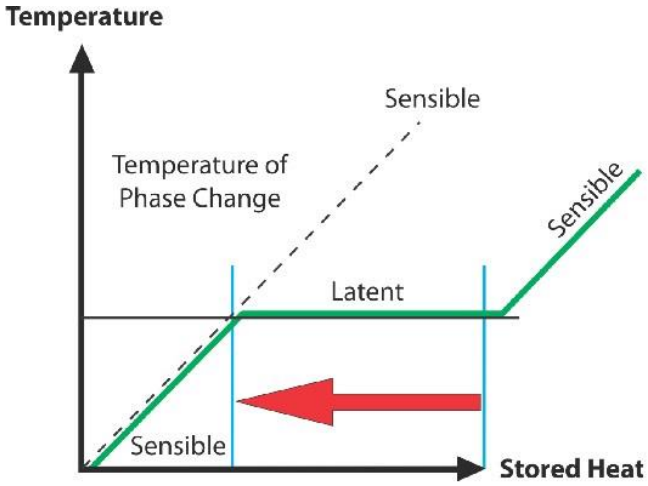

Figure 2-1: Heat storage as latent heat for the case of solid-liquid phase change

The thoughtful choice of material, taking into consideration its melting temperature, a greater amount of thermal storage can take place per unit mass by utilizing latent heat storage along with sensible heat within a temperature range bracketing the

materials melting point than with the use of sensible heat storage alone. The amount of energy that is stored over the phase change temperature range is thus the sum of the latent heat and the sensible heat over this temperature range (Zalba et al., 2003):

$$Q_t = \int_{T_i}^{T_m} mC_p \,.\, dT + \, ma_m \Delta H_m \, + \int_{T_m}^{T_f} mC_p \,.\, dT \tag{2-2}$$

Where a_m-fraction melted, ΔH_m -heat of melting per unit mass (J/kg).

Latent heat storage systems are also more energy efficient as they operate at a much smaller temperature difference during the charge-discharge process which ultimately increases the plant efficiency and possesses a higher energy density. With all of the advantages offered by the utilization of latent heat storage as a form of TES, it has become a rapidly growing field of research and development. In particular, research into the use of phase change materials (PCMs) that undergo a solid-liquid transition at ever-increasing temperatures has become a topic of great interest.

2.1.3 Chemical Energy Storage

The third and final form of TES is that of chemical energy storage, which stores and releases energy through endothermic and exothermic reactions. Due to its high-energy storage density and controllability, chemical energy storage is a highly attractive method for TES. However, due to a lack of certainty in physio-chemical and thermodynamic properties, the use of chemical storage is highly limited (Herrmann & Kearney, 2002).

2.2 Phase Change Materials

In the past, applying the latent heat storage (LHS) method to solar energy systems has been greatly explored. It is crucial that LHS systems have the ability to store thermal energy during the day so such energy can be used at night. Thermal Energy Storage (TES) technologies rely on high-quality Phase Change Materials (PCMs), which should have

high heat storage capacity and excellent heat transfer performance. PCMs include the solid-solid type (low phase change enthalpy) in which the phase transition occurs within the solid state, the solid-liquid type (high phase change enthalpy) in which the phase changes from solid to liquid, and the liquid-gas type (very high phase change enthalpy) in which the phase changes from liquid to gas. The large volume change in the liquid-gas PCMs restricts their application in TES. The relatively low phase change enthalpy of the solid-solid PCMs also restricts their application in TES. Relatively high phase change enthalpy and small volume change make the solid-liquid PCMs the ideal option for TES. Materials that can be used for thermal energy storage must have a large latent heat, high thermal conductivity, a melting temperature that lies within a useful range for its desired application, and melt homogeneously with minute sub-cooling. It is also important, especially for this project, that they be low cost, safe, noncorrosive, and chemically stable. For the latent heat method of storage, phase change materials are valid and widely accepted for applications. When the PCM's peak temperature is reached, it is able to continue to store additional energy by transitioning phases. Once the temperature begins to cool, this absorbed energy can be discharged through the reverse process. Prior to the melting of a solid, the binding forces that preserve the solid structure must be overcome. By absorbing enough energy these forces can be weakened, resulting in a phase change from solid to liquid. The latent heat, or heat of fusion, is the energy required for the entire melting of the material. It signifies the variation in thermal energy levels concerning the material's liquid and solid states. PCMs are materials that are known to have a high heat of fusion. Consequently, the solidification of the liquid entails the elimination of the latent heat with the resulting configuration of atoms as a more stable lattice. This can all be seen in Figure 2-2.

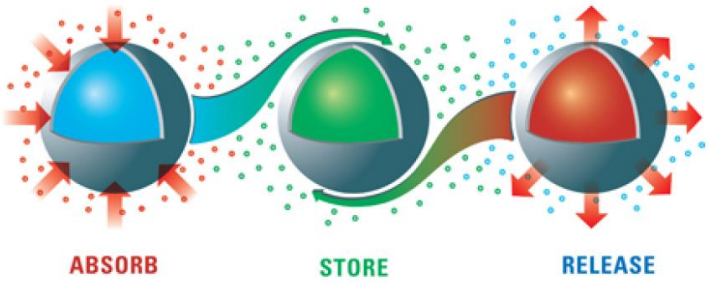

Figure 2-2: The melting and solidification processes of PCMs

Given below is a list of properties of PCMs which make them useful for the solar applications:

Thermo-physical Properties:

- PCMs could be selected with melting temperature in the required temperature range of operation.
- Comparatively higher latent heat per unit volume.
- High specific heat for additional heat storage through sensible heat.
- High thermal conductivity in solid as well as liquid phases to accelerate the charging and discharging time of energy storage systems.

Kinetic Properties:

- Nucleation rate is high which is beneficial for avoiding super cooling of the liquid phase.
- Crystal growth rate is high, which assists the system to meet demands of heat recovery from the storage system.

Chemical Properties:

- Chemical stability.

- Complete reversible freeze / melt cycle.
- Almost no degradation after a large number of freeze / melt cycles.
- it should be non-toxic, non-flammable and non-explosive to ensure safety

2.3 Assortment of PCMs

Over the past 40 years various types of components, including hydrated salts, paraffin waxes, fatty acids, the eutectics of organic and non-organic compounds and polymers have been regarded as potential PCMs. PCMs could be separated into three main groups – depending on the temperature ranges over which the TES phase change happens: (i) low temperature PCMs – with phase change temperatures below 15℃, typically employed in air conditioning applications as well as the food industry; (ii) mid temperature PCMs, the most famous – with phase transition temperatures within the range 15–90℃ with solar, medical, textile, electronic and energy-saving applications in building design; (iii) high temperature PCMs having a phase change above 90℃ designed primarily for industrial and aerospace applications (Liu et al., 2012). PCMs is usually listed in their mode of phase change: gas–liquid, solid–gas, solid–liquid and solid–solid systems.

The applications of PCMs which has a solid–gas or liquid–gas phase change are restricted in TES systems due to the significant volume changes linked to the transition – even when they contain a substantial phase change latent heat(Abhat, 1983). Significantly smaller volume changes happen, normally ca. 10% or less, with solid–solid and solid–liquid transformations. This will make them economically and practically interesting as materials for TES systems regardless of their smaller heat of phase transition(Sharma et al., 2009). Solid–solid PCMs utilize the heat from the phase change one to another crystalline form which enables it to be considered as an alternative to solid–liquid PCMs. In general, the heat of phase transition for solid–solid PCMs is lower compared to solid–

liquid PCMs. However, employing the former group of materials can preclude the problems of PCM leakage at temperatures over the phase change temperature, a substantial technical challenge with solid–liquid PCMs (Pillai & Brinkworth, 1976).

2.4 Solid–Liquid PCMs

Various sorts of solid–liquid PCMs are utilized for thermal storage applications, including water, salt hydrates, paraffin, selected hydrocarbons, polymers and metal alloys. Within the next sub-sections, different classes of solid–liquid PCMs will be described (Figure 2-3).

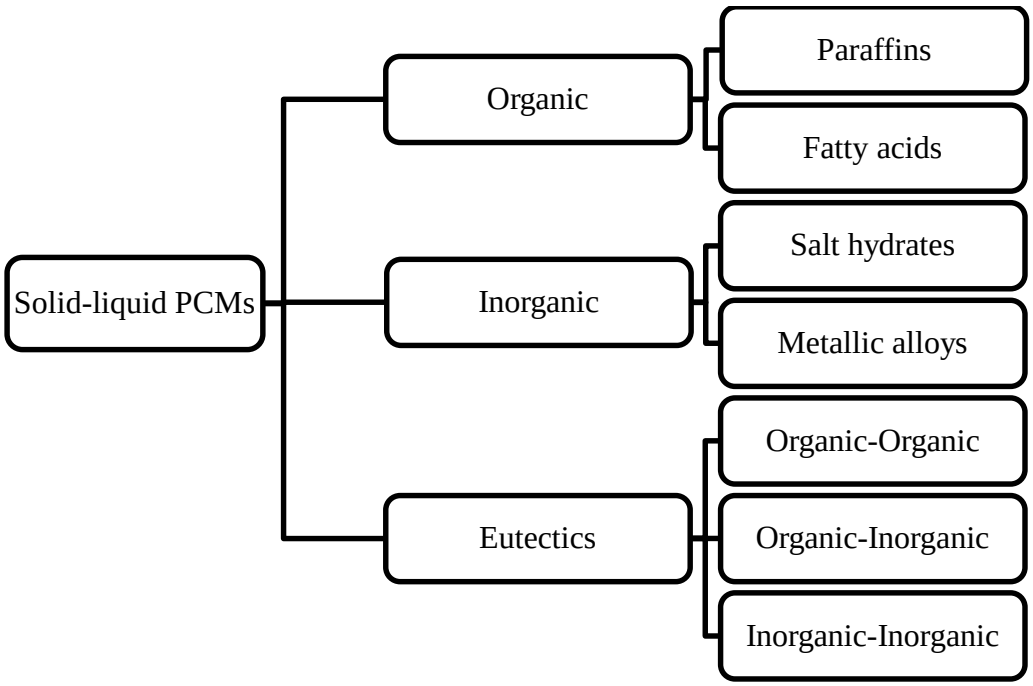

Figure 2-3: Solid-liquid PCMs classification

2.4.1 Organic PCMs

2.4.1.1 Paraffins

Paraffins (saturated hydrocarbons with C_nH_{2n+2} formula), which constitute the broadly used solid–liquid PCMs, possess a high latent heat storage capacities over a narrow temperature range and are considered as non-toxic and ecologically harmless.

Commercial paraffin waxes are cheap with moderate thermal storage densities (~200 kJ/kg or 150 MJ/m^3) and a wide range of melting temperatures. They undergo negligible subcooling and are chemically inert and stable with no phase segregation. However, they have low thermal conductivity (~0.2 W/mK), which limits their applications. Metallic fillers, metal matrix structures, finned tubes and aluminum shavings were used to improve their thermal conductivity. The latent heat of paraffin is molar mass-based and their various phase change temperatures give the flexibility to select an appropriate PCM for a specific LHTES application. Paraffin waxes are safe, non-reactive and are compatible with metal containers as they do not promote corrosion. Recently, many research programs have studied the thermal characteristics of paraffins during their melting and solidification processes. Thermo-physical properties of some paraffins are given in Table 2-1.

Table 2-1: Thermo-physical properties of paraffins

Material	**Melting point (℃)**	**Latent heat (kJ/kg)**
N-tetradecane	5.5	226
N-pentadecane	10	205
N-hexadecane	16.7	237
N-henicosane	40.5	161
N-pentacosane	53.7	164
N-hexacosane	56.3	255

2.4.1.2 Fatty Acids

The general chemical formula of fatty acids is $CH_3(CH_2)_{2n}COOH$ and they have relatively high phase change enthalpy. Fatty acids have high thermal stability with no subcooling. However, being more expensive than paraffins and being corrosive are their

disadvantages(Abhat, 1983). Thermo-physical properties of some fatty acids are given in Table 2-2 (Sharma et al., 2009).

Table 2-2: Thermo-physical Properties of Fatty Acids

Material	**Formula**	**Melting point (°C)**	**Latent heat of fusion (kJ/kg)**
Acetic acid	CH_3COOH	16.7	184
Polyethylene glycol 600	$H(OC_2H_2)_n.OH$	20-25	146
Capric acid	$CH_3(CH_2)_8.COOH$	36	152
Eladic acid	$C_8H_7C_9\ H_{16}.COOH$	47	218
Lauric acid	$CH_3(CH_2)_{10}.COOH$	49	178
Pentadecanoic acid	$CH_3(CH_2)_{13}.COOH$	52.5	178
Tristearin	$(C_{17}H_{35}COO)C_3H_5$	56	191
Myristic acid	$CH_3(CH_2)_{12}.COOH$	58	199
Palmatic acid	$CH_3(CH_2)_{14}.COOH$	55	163
Stearic acid	$CH_3(CH_2)_{16}.COOH$	69.4	199
Acetamide	CH_3CONH_2	81	241
Methyl fumarate	$(CHCO_2NH_3)_2$	102	242

With an increasing number of carbon atoms in the fatty acids molecule, the melting and freezing points, the heat of melting and the degree of crystallization gradually increase. Carboxylic acids with an even number of carbon atoms in the structure possess higher values of thermal parameters than those with odd numbers of C-atoms (Tatsidjodoung et al., 2013). The melting and boiling points of fatty acids are relatively high and the saturated fatty acids exhibit low phase transition volume changes with very little or no supercooling when freezing.

2.4.2 Inorganic PCMs

2.4.2.1 Salt Hydrates

Salt hydrates are one of the most important group of PCMs due to their high volumetric heat storage capacity. The most important properties of salt hydrates are the following:

- High melting temperature
- High melting enthalpy
- High thermal conductivity

They consist of salts and water which combine in a crystalline matrix when the material solidifies. Salt hydrates behave in three different ways: congruent, incongruent and semi-congruent. Salt hydrates: are cheaper; tend to have relatively higher heat storage capacity per unit volume; and have higher thermal conductivity, than organic PCMs. They are the best options for low temperature ranging from 0℃ to 99℃, based on their thermal properties. However, they have a tendency to subcool and not melt congruently. They also have sharp melting points and low volume change during phase transformation, but tend to corrode metal containers that are commonly used in thermal storage (Tatsidjodoung et al., 2013). Thermo-physical properties of some salt hydrates are given in Table 2-3.

Table 2-3: Thermo-physical Properties of salt hydrates

Material	Melting point (℃)	Latent heat (kJ/kg)
$K_2HO_4.6H_2O$	14	108
$KF.4H_2O$	18	330
$K_2HO_4.4H_2O$	18.5	231
$LiBO_2.8H_2O$	25.7	289
$FeBr_3.6H_2O$	27	105
$CaCl_2.6H_2O$	29-30	170-192
$Na_2SO_4.10H_2O$ (Glaubeur's salt)	32	251-254

However, a major problem with salt hydrates may result from the decrease of their energy storage density with cycling. Incongruent melting is one of the causes of this problem. (Sharma et al., 2009) described it as follows: during the melting of most salt hydrates, the released water is not sufficient to dissolve all the crystals present. Consequently, due to their density, crystals settle at the bottom of the container and will not reform a hydrated crystal during the subsequent solidification of the compound. This causes irreversibility in the process. Subcooling before crystallization is another serious problem associated with hydrated salts. Several techniques such as the use of nucleating agents (Telkes, 1952).

2.4.2.2 Metallic alloys

Metallic alloys are employed as high-temperature PCMs since they provide high thermal reliability (Liu et al., 2012). The largest phase change heat, over a mass or volume basis, has been discovered for binary and ternary alloys from the relatively plentiful elements Al, Cu, Mg and Zn, but not all of the probable materials are ideal for utilization in TES systems (Birchenall & Riechman, 1980). In comparison with other latent heat

energy storage materials eutectic aluminum alloys were principally examined to be used as PCMs in high temperature TES systems due to their appropriate phase transition temperature, high latent heat density and great thermal stability (Renyun, 2005). Some of the features of these materials are as follows: (i) low heat of fusion per unit weight (ii) high heat of fusion per unit volume, (iii) high thermal conductivity, (iv) low specific heat and (v) relatively low vapor pressure.

2.4.3 Eutectic PCMs

Eutectic mixtures or eutectics, i.e. a combination of several solids in such ratios which the melting point can be as low as possible, normaly possess sharp melting points as well as higher volumetric storage density compare to the organic compounds. However, minimal data can be found for their thermal and physical properties. Eutectics can be separated in 3 groups based on the materials of which they consist: (i) organic–organic, (ii) inorganic–inorganic and (iii) inorganic–organic eutectics. Eutectic nearly always melts and freezes without segregation since they freeze to an intimate mixture of crystals, leaving little opportunity for the components to separate. On melting both components liquefy simultaneously, again with separation unlikely(Baetens et al., 2010).

2.5 PCMs Advantages and Limitations

Comparison of organic and inorganic PCMs is shown in Table 2-4. Advantages of PCMs in general are their availability in a large temperature range for different working requirements, their high thermal energy storage density and quasi-constant phase change temperature(Oró et al., 2012). Some key characteristics of organic materials are their self-nucleating property, small subcooling, non-corrosiveness towards metallic container, and small phase segregation(Kuznik et al., 2011). Inorganic materials have generally higher thermal conductivity, hence more suitable for active TES systems; they are non-flammable, so ideal for use in buildings; and compatible with plastic containers(Memon, 2014). Eutectics are presented as a parallel category for comprehensibility; they are

mixtures of organic and/or inorganic materials at specific composition providing a sharp phase change temperature (Cabeza et al., 2011). One major limitation of using PCMs in an active storage system is their low heat transfer performance. Although inorganic PCMs exhibit higher thermal conductivity, it rarely surpasses 0.7 W/m.K (Pasupathy et al., 2008; Zalba et al., 2003).Various approaches have been taken to enhance the heat transfer rate in LHTES. Typical solutions are extension of heat transfer surface and improvement of material's thermal conductivity. The surface extension is done through the addition of fins (Agyenim & Hewitt, 2010; Castell et al., 2008; Ismail et al., 2001; Tay et al., 2013a),impregnation of PCM to highly conductive matrices (Mesalhy et al., 2006; Siahpush et al., 2008; Yin et al., 2008; Zhao et al., 2011), insertion of high conductive fibrous materials (Frusteri et al., 2005; Nakaso et al., 2008), and encapsulation (Regin et al., 2008; Salunkhe & Shembekar, 2012), among others. Material property enhancement is achieved with dispersion of highly conductive particles (Oya et al., 2013; Pincemin et al., 2008; Wang et al., 2009c). Results have shown the largest heat transfer improvement with impregnation methods reaching 130 to 180 times higher thermal conductivity (Mills et al., 2006; Zhong et al., 2013).

Table 2-4: Advantages and Limitations of PCMs

	Advantages	Disadvantages
Organic PCMs	1. Availability in a large temperature range 2. High heat of fusion 3. No supercooling 4. Chemically stable and recyclable 5. Good compatibility with other materials	1.Low thermal conductivity (around 0.2 W/m K) 2.Relative large volume change 3.Flammability
Inorganic PCMs	1. High heat of fusion 2. High thermal conductivity (around 0.5 W/m K) 3. Low volume change 4. Availability in low cost	1. Supercooling 2. Corrosion 3. Phase segregation
Eutectics	1. Sharp melting temperature 2. High volumetric thermal storage density	Lack of currently available test data of thermo-physical properties

Subcooling is yet another hindrance to the use of inorganic materials in active systems. Subcooling, sometimes also referred to as supercooling, occurs when solidification initiates below the melting temperature. (Ryu et al., 1992) reported that Sodium Sulfate Decahydrate may have subcooling reaching 20 ℃ below its melting point in its original form. Cold finger, which is a cold point in the storage unit, may initiate crystal-lization and lower the subcooling.

Other properties, such as flammability, volume change, and corrosion issues also limit the use of PCMs in building structures, and impose constraints on the storage containers as well as on the heat exchanger materials (Tyagi & Buddhi, 2007). These

issues can however be overcome with adequate choice of storage container and heat exchanger material.

2.6 Heat Transfer Enhancement Methods of PCMs

Heat Transfer Enhancement Methods Enhancement techniques are supporting tools for thermal energy storage systems. The compact enhanced design yields good results in thermal systems. The rapid growth of world literature on this subject indicates that enhancement is now a major specialty area in thermal energy (heat transfer) research and development. Hence the industrial and domestic utilization of enhancement techniques increases day by day.

In spite of all the desirable properties of PCMs mentioned earlier, there is one property, which effects, the charge and discharge time drastically. This property is the low thermal conductivity of most of the PCMs. To account for this downside, techniques to enhance the thermal conductivity are employed (Figure 2-4). Studies conducted in this area are: finned tubes (Castell et al., 2008; Shon et al., 2014; Solomon & Velraj, 2013; Velraj et al., 1997, 1999; Zhang & Faghri, 1996), bubble agitation (Mohamed, 2005) , metal matrix in PCM (Mehling & Cabeza, 2008; Zalba et al., 2003), high conductivity particles dispersion in PCM (Oya et al., 2013; Wen & Ding, 2004; Wu et al., 2010), shell and tube (Akgün et al., 2008; Trp, 2005) , micro-encapsulation of the PCM (Hawlader et al., 2003; Özonur et al., 2006; Tahan Latibari et al., 2013)or Shape-Stabilized PCMs (Cheng et al., 2010; Xiao et al., 2002; Zhang et al., 2006a; Zhang et al., 2006c).

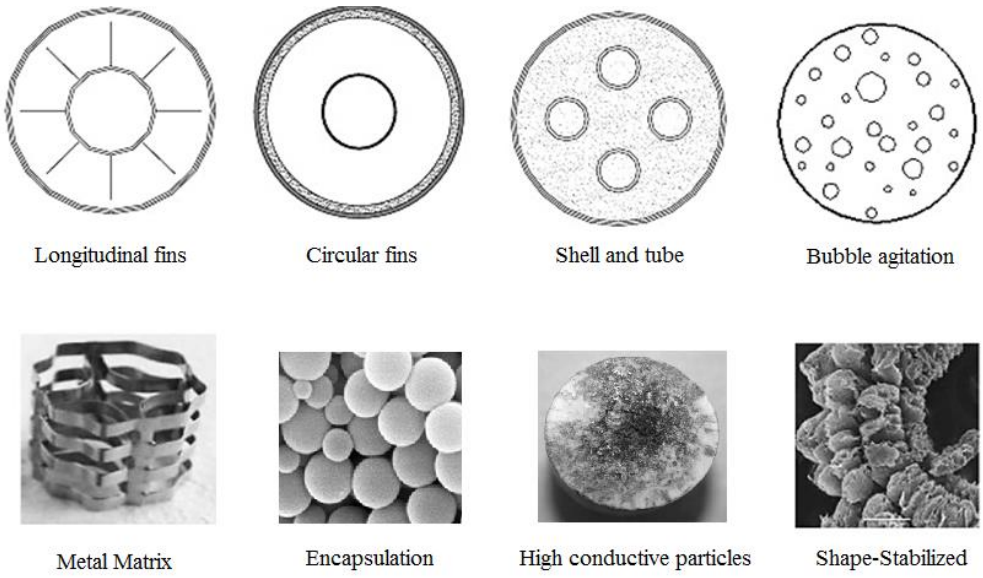

Figure 2-4: Heat transfer enhancement methods employed for PCMs (Salunkhe & Shembekar, 2012)

Once the expenses of encapsulation and those relevant to the enhance of PCM conductivity are reviewed, the increasing interest being directed to the development of form–stable, shape stabilized, composite materials, is clearly the reasonable strategy.

2.7 Form‑Stable (Shape-Stabilized) PCMs

As opposed to granular PCM, shape stabilized PCM (SSPCM) refers to the PCM being embedded in a support matrix, which allows it to keep its shape during phase transitions. The leakage of PCM, the selection of suitable container material, the additional thermal resistance of the container and container cost are often problematic when using granular forms of PCM, but shape stabilized PCM eliminates these drawbacks (Zhang et al., 2006b). In the case of building walls, it should be noted that the effect of surface tension in the host material prevents the PCM from leaking from the wall, even in the liquid phase (Kelly, 2000). The common PCMs used in SSPCMs consist mainly of various types of paraffin and fatty acids with different melting temperature, due to their stable properties. The supporting material matrix essentially provides a form of

encapsulation to the PCM during phase change. Common supporting materials include high density polythene (HDPE), silica and carbon graphite (which also enhances the thermal conductivity), and these should have a melting temperature higher than the PCM. SSPCMs can be classified by their supporting materials: polymers, expanded graphite and other materials.

2.7.1 Shape Stabilized PCMs with Polymer Matrix

Polyethylene (PE), because of its properties and chemical attraction to paraffins, as commonly employed in shape stabilized PCMs to be a supporting material (Hong & Xin-shi, 2000). The paraffin/HDPE composites as SSPCMs by melt mixing was prepared by (Sarı, 2004).The maximum weight percentage of paraffin that was hold by HDPE was found to be 77% while paraffin was well distributed in the composite PCM. Moreover, the expanded and exfoliated graphite was added to enhance the thermal conductivity of the SSPCM by 14-24% (Kaygusuz & Sari, 2007). (Cai et al., 2006) reported the results for SSPCMs based on HDPE–ethylene–vinyl acetate (EVA) alloy, organically-modified montmorillonite (OMT), paraffin and intumescent flame retardant (IFR), processed in a twin-screw extruder. The outcomes revealed that the HDPE–EVA/OMT nanocomposites behaved as the supporting material and created a three-dimensional network structure, while the paraffin PCM was dispersed within the network.(Alkan et al., 2006) used the acrylic polymers such as Poly methyl methacrylate (PMMA) as a polymer matrix while Polyethylene glycol (PEG) was employed as PCM. The PEG was shape stabilized with maximum weight percentage of 80wt% without leakage. They also investigated blends of PMMA with stearic acid (SA), palmitic acid (PA) and myristic acid (MA) and the maximum mass percentage of fatty acids in the blends to avoid their seepage in the molten state was found to be 70%.(Zhang et al., 2011) added aluminum nitride as a thermal conductive material to enhance the PMMA/PEG composite PCM. The results indicated that the thermal conductivity of the composite was increased by 53% by using 30wt% of

aluminum nitride. The poly(vinyl chloride) (PVC) was used by (Sari et al., 2006) for shape stabilizing the fatty acids without any leakage in the molten state while the highest miscibility ratio of fatty acids was identified at the level of 50%. Polyurethane(PU) foams containing PCMs were introduced by (Sarier & Onder, 2007) for PU-PCM production on an industrial scale. A unique method was adopted by (Chen et al., 2009) to obtain ultrafine SSPCMs fibers of stearyl stearate/poly(ethylene terephthalate) (SS/PET) by using electrospinning. The major problem with polymers is their low thermal conductivity and thermal stability that will hinder their application in practice.

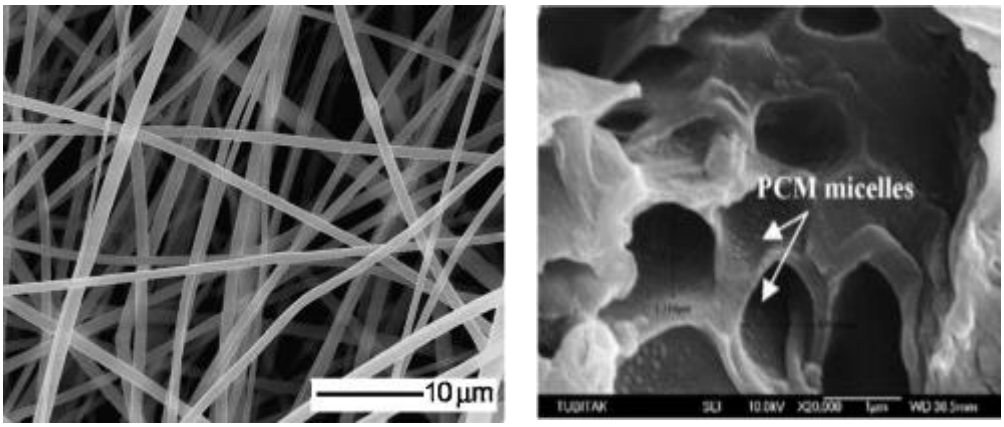

Figure 2-5: Shape stabilized PCMs with polymer matrix(Nkwetta & Haghighat, 2014)

2.7.2 Shape Stabilized PCMs with Expandable Graphite Matrix

In recent years, porous graphite matrices have been used to improve thermal conductivity of the PCMs.(Sarı & Karaipekli, 2007) introduced Paraffin/expanded graphite (EG) SSPCM that was prepared by vacuum impregnation method. The shape stabilization was achieved by adding 10% mass fraction of EG while the capillary and surface tension forces between paraffin and EG avoided the leakage (Figure 2-6). The thermal conductivity of paraffin was enhanced from 0.22 to 0.85 W/m K. The fatty acids with EG composites also were investigated by (Sari et al., 2008) and results suggested that the shape stabilization was done by using 20 wt% of EG. The melting and solidifying

temperatures were almost identical to those of the fatty acids while the latent heats were lower than those pure fatty acids (Sarı & Karaipekli, 2009).

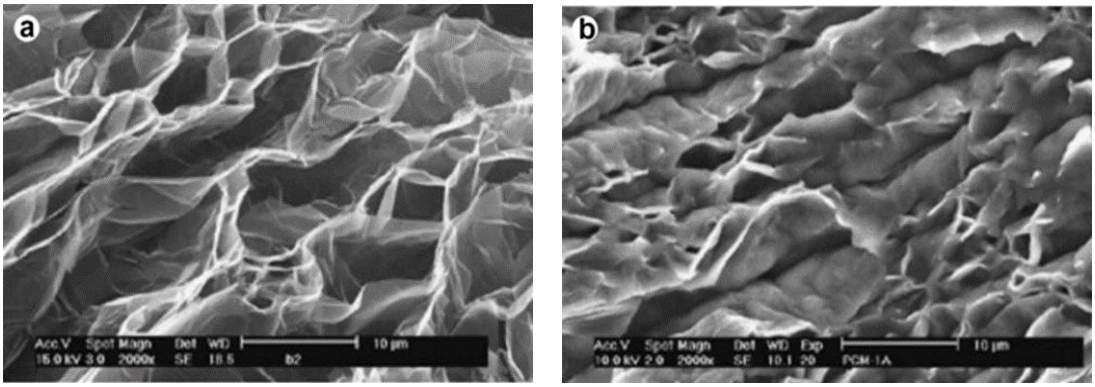

Figure 2-6: SEM images of a) Expanded graphite b) Paraffin/expanded graphite composite PCM(Sari et al., 2008)

The PEG/EG composite PCM was prepared by (Wang et al., 2009d) and results indicated that PEG was adsorbed by EG network by 90wt%. The conductivity of blends was improved significantly with the high value of 1.324 W/m.K compared to the pure polyethylene glycol conductivity of 0.2985 W/m.K. (Xia et al., 2010) examined EG/paraffin composite PCMs by having an EG weight percentage from 0 to 10 wt.%. Thermal characterization of the SSPCMs by DSC exposed some changes in the phase transition temperatures. In the beginning the latent heat of the paraffin within the composite PCMs improved however it was decreased by rising the fraction of EG.

2.7.3 Other Shape Stabilized PCMs

There are many materials that were employed in shape stabilization of the PCMs. The PEG/SiO2 from-stable PCM were prepared by (Wang et al., 2009b) and results are shown that up to 85% PEG could be held by SiO2 pores without any leakage of the molten PEG while the thermal conductivity of the composite was enhanced. (Tang et al., 2012) improved the thermal conductivity of PEG/SiO2 hybrid composite PCM by doping the Cu via the chemical reduction of CuSO4 .The thermal conductivity of

Cu/PEG/SiO_2 SSPCM was enhanced by 38.1% compared to pure PEG. The expanded clay, expanded fly ash and expanded perlite was used by (Zhang et al., 2005) to prepare the granular SSPCMs with vacuum impregnation method. This technique allowed that 65wt% of PCMs be impregnated into porous materials. The composite of myristic acid(MA) and capric acid(CA) with expanded perlite (EP) was prepared by vacuum impregnation and the maximum MA/CA absorption of EP was found to be 55–60 wt% without any leakage (Karaipekli & Sarı, 2008; Sarı & Karaipekli, 2008). The thermal reliability of composite PCM were examined by 5000 thermal cycles and the thermal conductivity was improved by about 58% by addition of 10 wt% of EG (Sarı et al., 2009). Afterwards, the eutectic mixture of CA/MA was impregnated to the vermiculite (VMT) with a maximum percentage of 20 wt% and thermal conductivity was enhanced by about 85% with introducing of 2 wt% of EG (Karaipekli & Sarı, 2009) .(Li et al., 2011a) prepared CA–PA binary blends impregnated into attapulgite. The pore structure of the CA–PA/attapulgite composite PCM was found to be an open-ended tubular capillary type, which was beneficial for the adsorption processes. The same group of researchers also investigated binary fatty acid/diatomite shape-stabilized PCMs. Taking account of the phase diagrams, a series of binary fatty acids composed of CA, LA, PA and SA was prepared. The binary fatty acids were absorbed into four types of diatomites having different specific areas, which then acted as the supporting material. The results showed that there is an optimum absorption ratio between the binary fatty acids and the diatomite (Li et al., 2011a). (Mesalhy et al., 2006) studied on a porous medium infiltrated with PCM by employing different carbon foam matrices with paraffin wax as the PCM. The outcomes indicated that the porosity and thermal conductivity of the SSPCMs performed critical roles in the thermal performance of the composite PCMs. Recently, (Zhou et al., 2013) have prepared highly conductive 3D porous graphene/Al_2O_3 composites using ambient pressure chemical vapor deposition. The formation mechanism of graphene was

attributed to the carbothermic reduction occurring at the Al_2O_3 surface to initiate the nucleation and growth of the graphene. It was shown that such a porous composite is attractive as a highly thermally conductive reservoir for PCMs (SA).

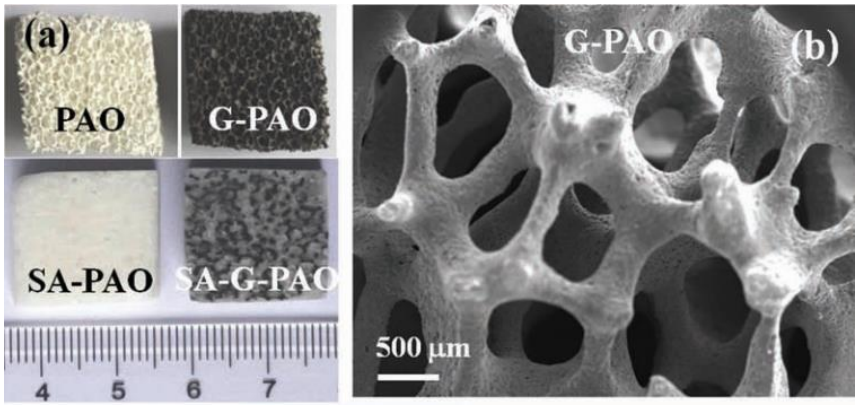

Figure 2-7: Photographs and SEM of large porous alumina (PAO) and SSPCMS (Zhou et al., 2013)

2.8 Summary

CHAPTER 2 introduced the concept of phase change materials, with a focus on solid-liquid PCMs. The important aspect of high heat content at narrow ranges of temperature supports the use of PCM in solar applications, but various other thermo-physical, kinetic and chemical properties have also been identified as essential to the proper utilization of PCMs. The lack of certain desired properties can be overcome through appropriate system design. The classification of PCMs into organic, inorganic and eutectics has been presented.

Solid-liquid PCMs are found to have poor heat transfer properties and hence are not used directly as a heat transfer medium. Shape stabilization, heat transfer enhancements and efficient system designs have been popular methods to improve the heat transfer properties. When the costs of encapsulation and those related to the increase of PCM conductivity are analyzed, the increasing attention being given to the development of form–stable, shape stabilized, composite materials, is clearly the rational approach. The classification of SSPCMs were presented by introducing previous researches that have been done. The

majority of PCM systems encountered in the literature have been studied for the SSPCMs that could preserve the PCM by mass percentage of between 50 to 80% with moderate thermal conductivity enhancement.

The following chapters describe the novel materials and SSPCMs employed in this study to enhance the performance of SSPCMs.

CHAPTER 3

MATERIALS AND METHODS

3.1 Introduction

This chapter deals with fundamentals theory and technologies of manufacturing the SSPCMs incorporated with novel carbon materials. The processing techniques involving material selection, determination of specific parameters and material pretreatment are thoroughly discussed. A full factorial experimental design and its principals are determined. Characterization of these composites and their preparation methods are addressed in this chapter. A number of modern characterization techniques were adopted to study the structure and morphology features of novel SSPCMs. These techniques included, Field Emission Scanning Electron Microscopy (FESEM) and Transmission Electron Microscopy (TEM) for surface and inner structure observation; Fourier Transmittance Infrared Spectra (FT-IR), Atomic Force Microscopy (AFM), X-ray photoelectron spectroscopy (XPS), Raman Spectroscopy, X-ray Diffractometry (XRD), Differential Scanning Calorimetry (DSC), Thermal Gravimetry (TG) and Derivative Thermogravimetric analyses (DTG). These instruments were applied to the objective evaluation of chemistry and identification of physical structure. The thermal cycling and solar adsorption test also were introduced to investigate thermal performance of the prepared SSPCMs. The thermal conductivity of the prepared PCMs also were measured by two methods and explained in this chapter.

The materials research for TES applications and some fundamental aspects should be considered as shown in Figure 3-1 which was followed in this research.

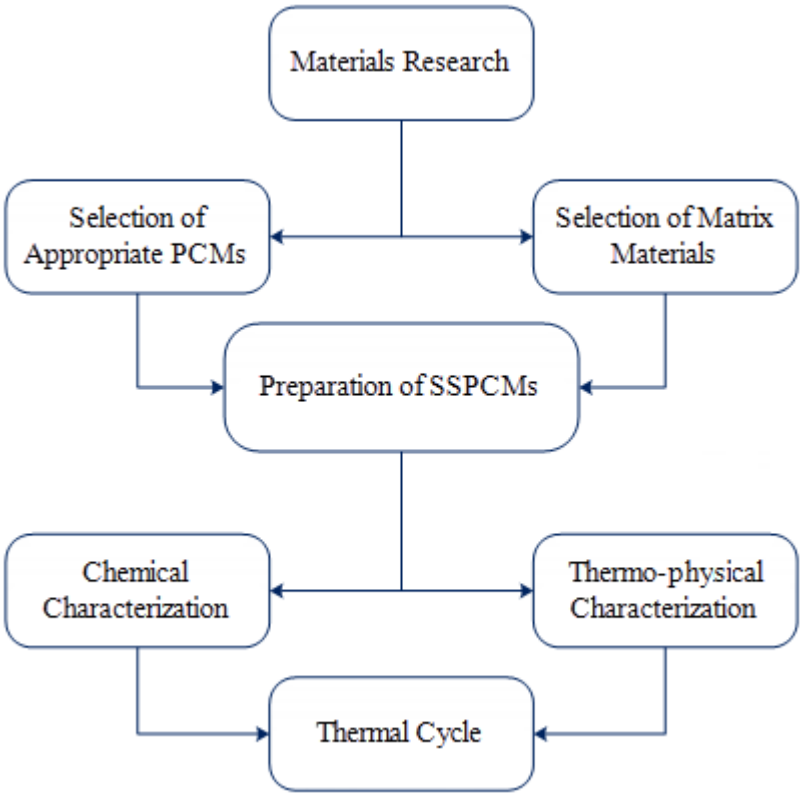

Figure 3-1: Flowchart of SSPCMs preparation and characterization process

3.2 The Selection of PCMs

Thermal-regulating solar applications aiming to work in the environment of outdoor with sharp temperature fluctuation of 50~70℃ is one of the objectives in the present study. To fulfill the target, the selection of phase change materials is an essential work in the project. Paraffin compounds are the first choice due to the merit of the materials that have been addressed in CHAPTER 2.

Usually, PCMs used in solar applications are belonged to the type of medium melting point paraffin (50~70℃) and most of them are in solid form under normal conditions. The shape stabilization technology enables PCM to be in particulate form above melting point which is more easily to handle. In this study the organic PCMs were considered due to their appropriate malting temperatures and good thermal stability and properties.

3.2.1 Paraffin Wax

Among the paraffin compounds, paraffin wax is the material that can meet this demand. More importantly, the melting point of it is around (50~70℃), which is just in the temperature range of the solar working condition. Normal paraffins are hydrocarbons whose generalized chemical formula is given by C_nH_{2n+2}. , where n is greater than about 20. The chemical structure is shown in Figure 3-2.

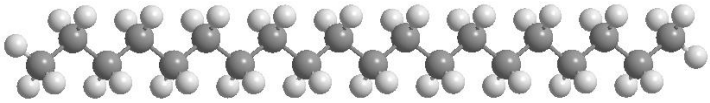

Figure 3-2: Chemical structure of paraffin wax

The PCM used was an industrial-grade paraffin wax acquired from Sigma-Aldrich, Inc. with a melting range of 53-57℃. This wide melting range is caused by impurities in the refining process, but is necessary for testing because of its low cost and wide scale availability. The physical properties of paraffin wax are listed in Table 3-1.

Table 3-1: Physical properties of paraffin wax

Name	Paraffin Wax
Molecule weight (g/mol)	352
Density (g/cm3)	at 25℃ 0.801
Melting Point (℃)	53-57℃
Boiling point (℃)	402
Heat conductivity (W/m.K)	0.2-0.305
Thermal capacity ΔH (J/g)	132

3.2.2 Palmitic Acid

Fatty acids are one of the organic phase change materials. They possess some superior properties over other PCMs such as melting congruency, good chemical stability, non-toxicity and suitable melting temperature range for solar passive heating applications. Palmitic acid (PA), also known as hexadecanoic acid, is probably the most

popular saturated fatty acids obtained from animals and plants. It's a white solid that melts at ~63℃ and its formula is $CH_3(CH_2)_{14}COOH$. Since its name tells us, it can be found in palm oil and also in butter, cheese, milk and meat. The chemical structure is shown in Figure 3-3.

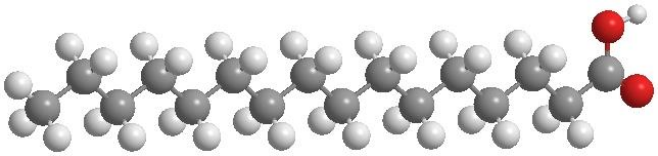

Figure 3-3: Chemical structure of palmitic acid

PA used was supplied by Acros Organics, with a melting range of 59-63℃. The physical properties of PA are listed in Table 3-2.

Table 3-2: Physical properties of the palmitic acid

Name	Palmitic acid
Purity	98%
Molecule weight (g/mol)	256
Density (g/cm3)	at 25℃ 0.853
Melting Point (℃)	59-63℃
Boiling point (℃)	351
Heat conductivity (W/m.K)	0.21-0.3
Thermal capacity ΔH (J/g)	208

3.2.3 Stearic Acid

Stearic acid (SA) is a saturated fatty acid having an eighteen-carbon chain that also called Octadecanoic acid. It is a wax-like solid, that has chemical formula of $CH_3(CH_2)_{16}COOH$. Octadecanoic acid is probably one of the most common saturated fatty acids existing in nature following palmitic acid. The chemical structure is shown in Figure 3-4.

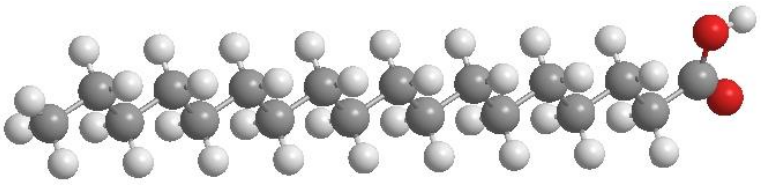

Figure 3-4: Chemical structure of stearic acid

The SA was supplied by Ajax Finechem with a melting range of 54-57.5℃. The physical properties of stearic acid are listed in Table 3-3 .

Table 3-3: Physical properties of stearic acid

Name	Stearic acid
Purity	99%
Molecule weight (g/mol)	284
Density (g/cm3)	at 25℃ 0.984
Melting Point (℃)	54-57.5℃
Boiling point (℃)	350
Heat conductivity (W/m.K)	0.2-0.25
Thermal capacity ΔH (J/g)	184

3.3 The Selection of Matrix Materials

Phase change materials will be incorporated into supporting materials structures by in order to prevent them from leakage while PCMs are in the liquid state as well as improving thermal properties. Another advantage of some SSPCMs is the granulation which is benefit for both PCM application and transportation. Therefore, matrix materials of the SSPCMs should be heatproof and chemically stable.

Carbon materials have comprehensive pore structures, high specific surface area and reasonably significant sorption capabilities, therefore they plays a crucial role in advanced research and engineering science, as an example in the refinement of liquids and gases (Ma et al., 2008; Simpson, 2008), the separation of mixtures (Chan et al., 2009),

the catalysis field (Fukuyama & Terai, 2008), as well as the hydrogen storage (Hu et al., 2007). Even with many studies on carbon materials, an investigation about the application of novel carbon materials in PCMs remains insufficient. There are some studies on the preparation and investigation of the form-stable PCMs using porous carbon materials, including graphite (Moeini Sedeh & Khodadadi, 2013), expanded graphite (Lee et al., 2014; Li et al., 2012; Sarı & Karaipekli, 2009; Zhang et al., 2012c), carbon nanofibers (Ehid et al., 2012; Elgafy & Lafdi, 2005; Fan et al., 2013), carbon nanotubes(Teng et al., 2013; Wang et al., 2009a), graphite nanoplatelets (Fan et al., 2013).The accessible research outcomes indicate that the form-stable composite PCMs based on porous minerals possess a good application possibility within the thermal storage fields.

This study focused on the novel carbon materials for the SSPCMs as it's shown in Figure 3-5.

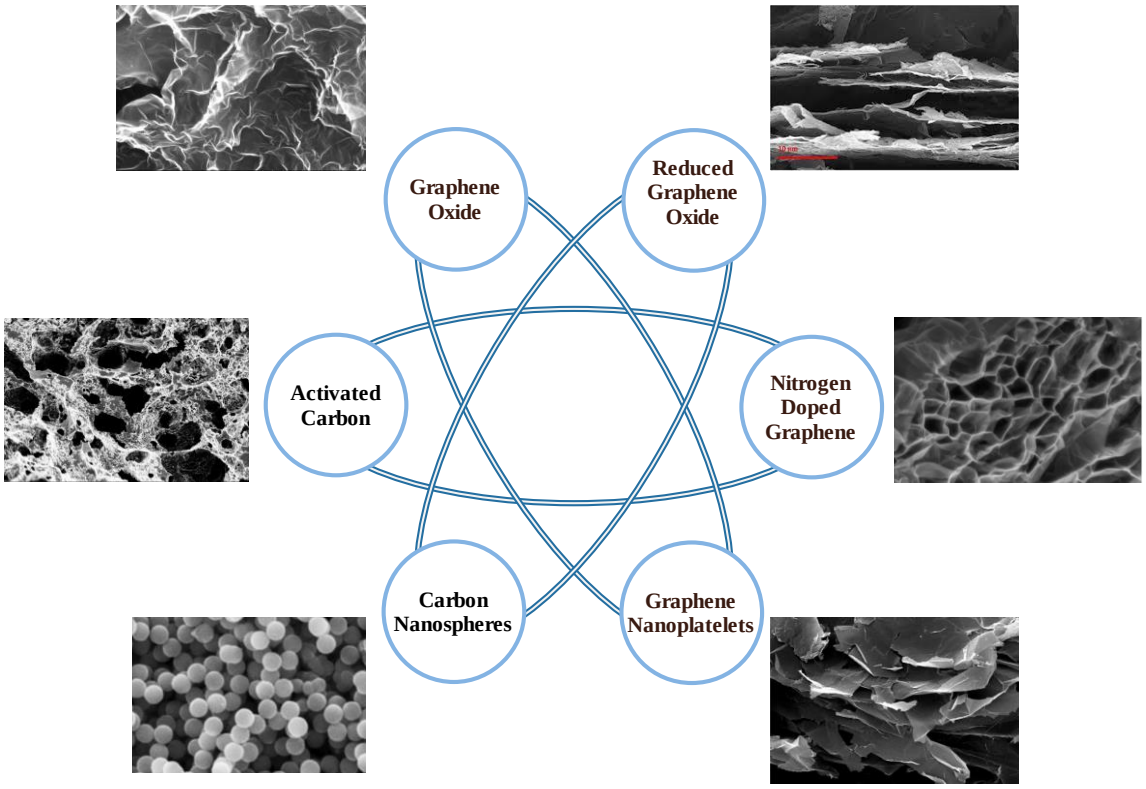

Figure 3-5: Novel Graphene materials for SSPCMs

The principal attractions of using carbon materials are excellent thermal properties, outstanding chemical stability, as well as stable and good heat resistance. The advantages described in the following paragraphs are the main reasons for the selection of carbon materials for preparation of the SSPCMs:

1. Resistant to heat and chemically stable.

The physical properties of this material remain unchanged at the high temperature of above 300℃. The inert chemistry properties give a better protection of PCM materials.

2. Compatible with the paraffin and fatty acid.

This will make it possible to successfully fabricate PCMs the unique 3D structures and formation of nano-composite SSPCMs.

3. Carbon indicates several interesting properties such as high thermal conductivity. For example the value of thermal conductivity (k) for single layer graphene is claimed to be in the range of 4840−5300 W/mK, (Balandin et al., 2008) that is higher than an order of magnitude more than that of copper. Graphene can be a promising thermally conductive filler due to its ultrahigh thermal conductivity and low density.

3.3.1 Graphene Oxide (GO)

Graphene is a two-dimensional all-sp^2-hybridized low density carbon with fascinating thermal, electrical and mechanical properties and has generated a rapidly growing research interest. Graphene sheets have high thermal conductivity, high specific surface area , and good electrical properties compared to other carbon based materials. The potential of using graphene-based products for PCMs has drawn much interest recently because it can be simply obtained by basic chemical processing of graphite. The thermal conductivity of composite PCMs depends not merely on the innate thermal

conductivity of the additives, but is also strongly related to the compatibility between additives and pure PCMs (Wang et al., 2010).

Ever since its discovery, graphene has been successfully prepared in various methodologies such as mechanical stretching (Becerril et al., 2008), epitaxal (Inagaki, 2000) and CVD growth (Bundy et al., 1996), chemical developments (Szabó et al., 2006) , etc. Among these, preparation of chemically developed functionalized graphene from graphene oxide (GO) has significantly high productivity and low cost, thereby has been extensively interested.

The controlled oxidation of graphite to GO leads to the decoration of the individual graphene layers with various oxygen functional groups. The repulsive forces between these highly electronegative oxygen moieties exfoliates the individual GO sheets while also promoting their dispersion in polar solvents. These oxygen functional groups vary in their number density but may include epoxides and hydroxyls on the GO surface and carboxylic groups along the edges. Other domains within the GO may be completely oxidized during the synthesis, leaving gaps in the lateral structure of the sheets. Furthermore, the effect of graphite oxidation and thus sp^2 to sp^3 conversion renders the material insulating in nature. Figure 3-6 illustrates the chemical and structural characteristics of a typical GO sheet.

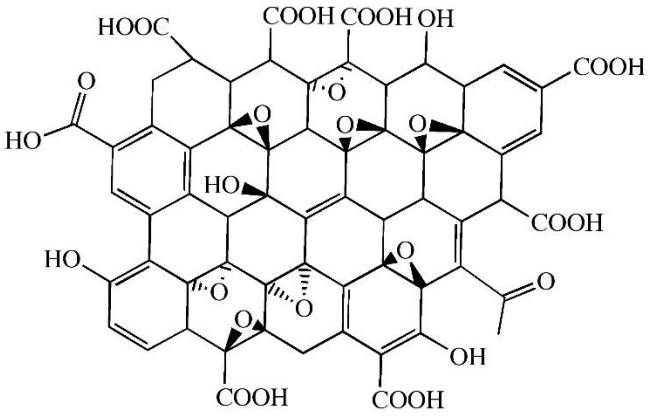

Figure 3-6: Chemical and structural characteristics of the functional groups tethered to the surface of pristine graphene to yield graphene oxide

Characterization of graphene oxide provides an important part of graphene research and involves measurements based on various spectroscopic and microscopic techniques. In this study the effect of GO on shape stabilization of the paraffin and palmitic acid as a fatty acid was investigated. The preparation methods for synthesis of the GO and SSPCMs were presented in next sections.

3.3.1.1 Preparation of Graphene Oxide

In the study, GO was prepared by a simplified Hummers' method. GO was synthesized by reacting 1g graphite flake (+100 mesh-Sigma Aldrich) with a mixture of 120 mL of H_2SO_4 and 13 mL H_3PO_4. Subsequently, 6g $KMnO_4$ (≥99.0% - Fisher Scientific) was added in to the reaction gradually and the reaction system was stirred at room temperature for 3 days to ensure the complete oxidation of the graphite. After cooling down to room temperature, the reaction system was stopped by pouring into a mixture of 250 mL of ice and H_2O_2 (30%) till the gas evolution stopped. This was carried out to be sure the reduction of the remainder permanganate into soluble manganese ions. Following the synthesis, prepared GO was washed by diluting in 1 M HCl and then with fresh DI water repeatedly until a pH of 5 was achieved. The ending product was separated from the mixture simply by using a centrifuge rotating at 11,000 rpm. The last product

will be dark brown color (Figure 3-7). The prepared GO was transferred to ultrasonication bath for 15 min and then dried in vacuum oven at 40℃.

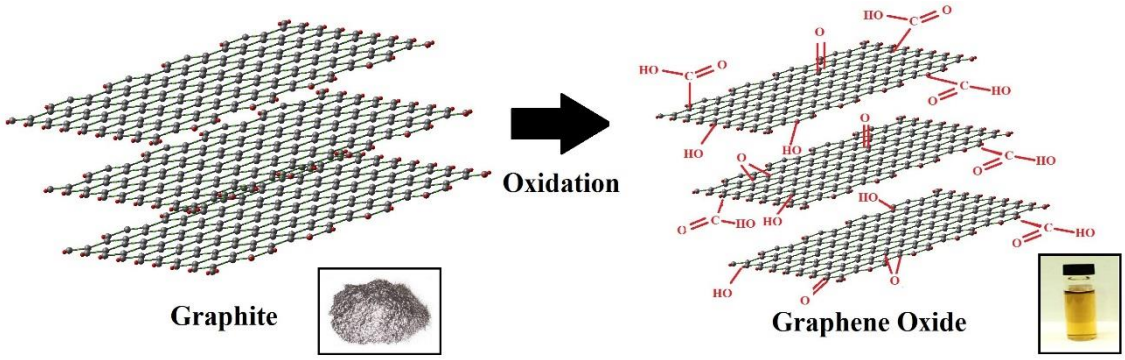

Figure 3-7: Schematic illustration for the possible formation mechanism of GO.

3.3.1.2 Preparation of Graphene Oxide SSPCMs

In this research impregnation method was used for incorporation of paraffin wax and palmitic acid as a PCMs in porous composite (GO). Vacuum impregnation has been confirmed to become quite effective in preparing composite PCM (Xiao et al., 2013). The schematic procedure of the impregnation process with vacuum assistance was shown in Figure 3-8.

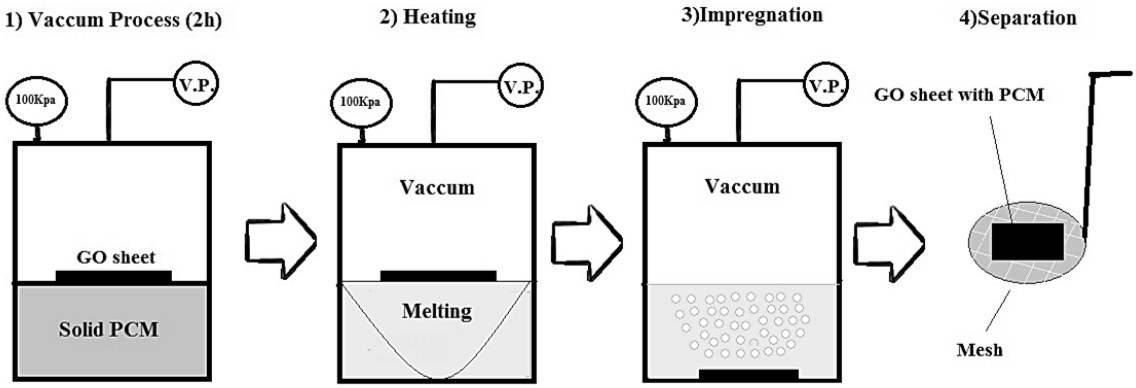

Figure 3-8: Procedure of vacuum impregnation

The PCM materials and GO sheets were positioned in a vacuum furnace. First of all, the vacuum procedure was done by vacuuming furnace for 2 h in order to discharge

air from pores of GO sheets. Second, PCM was melted at 90℃ in the vacuumed furnace and GO sheets were physically immersed in liquid PCM for 3h. The vacuum pump was switched off to allow the air to reenter the furnace and then composite PCM was removed from liquid PCMs by using a stainless mesh. The liquid PCMs that had not been infiltrated in the pores of the GO sheets were removed by keeping the composite PCMs in the furnace at 120℃. The procedure was done for four different graphene oxide (GO) sheets and all analyses were done for different sheets to get maximum mass percentage of the impregnated PCMs into the pores of the GO. The samples were named PCM1 to PCM4.

3.3.2 Nitrogen Doped Graphene (NDG)

The potential of using graphene-based products for PCMs has drawn much interest recently because it can be simply obtained by basic chemical processing of graphite. Since graphene properties are directly linked to the nano structure of the graphene sheets, quite a few attempts have been carried out to improve the electrical and thermal properties of graphene flakes by modifying their structures, as well as using novel synthesis methods, chemical functionalization and chemical doping with external atoms (Geng et al., 2011) . On the whole, chemical doping with sulfur(S), boron (B) or nitrogen (N) is regarded as a highly effective technique to modify the inherent properties of graphene-based materials. Particularly N-doping performs an important role in regulating the electronic, thermal and chemical properties of carbon materials because of the similar atomic size and the availability of five valence electrons to form strong valence bonds with carbon atoms. There is a fundamental interest to examine how nitrogen doping influences the structure of graphene and to see whether the chemical properties can be modified accordingly. A few works have been carried out to investigate the structural difference between graphene and N- doped graphene (NDG) but there have been no reports related to the effect of N-doping on the thermal conductivity of graphene. The NDG exhibits an excellent adsorption capacity for various classes of organic liquids including organic

solvents .In particular, NDG can adsorb amounts of the liquids up to 200 to 600 times its own weight, which is much higher than other typical carbonaceous sorbents such as graphene foam .

3.3.2.1 Preparation of Nitrogen Doped Graphene

Graphene oxide was synthesized from natural graphite powder (99.99%, <45 μm, Sigma Aldrich) employing a simplified Hummers' method. NDG was synthesized by a hydrothermal process with GO as raw material. In a typical method for preparing NDG, the pH of a dispersion of 50 mg GO in 100 ml H_2O after 1 h ultrasonication was adjusted to 11 using ammonia. The dispersion was treated hydrothermally in a Teflon-lined autoclave at a temperature of 160 ℃ for 12 h. A black precipitate was washed with deionized water and dried at 50 ℃ under vacuum. The schematic of NDG preparation process is shown in Figure 3-9.

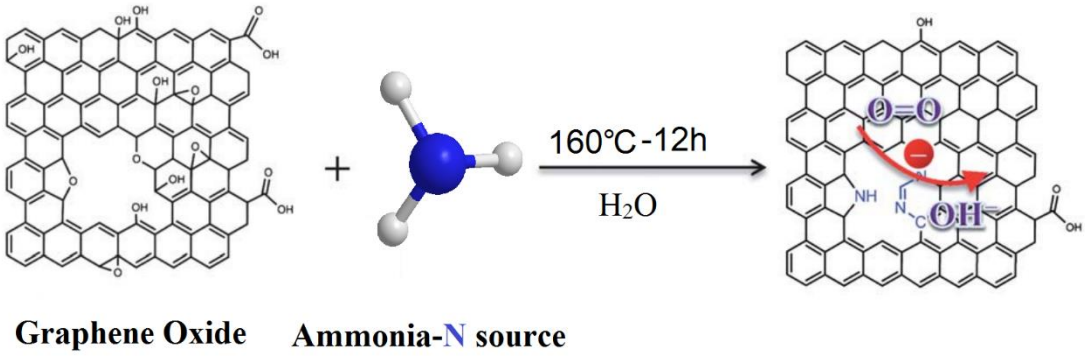

Figure 3-9: Representative synthetic pathway for N-doped graphene preparation

3.3.2.2 Preparation of PA/NDG Composite PCMs

The preparation procedure for the composite PCMs is demonstrated in Figure 3-10. 2 g of palmitic acid (PA) was dissolved in 50 ml toluene at 80 ºC, after which NDG with different mass percentages (1 to 5 wt %) was added to the solution. The solution was sonicated for 30 min at 150W to break down the NDG aggregates and obtain

a homogeneous dispersion of the nano particles. The mixture was then left inside a fume hood at 130 ºC to evaporate the toluene and poured into a mold. Finally, the PCM samples have been dried inside a vacuum oven overnight at 120 ºC to eliminate PA which had not been absorbed by NDGs.

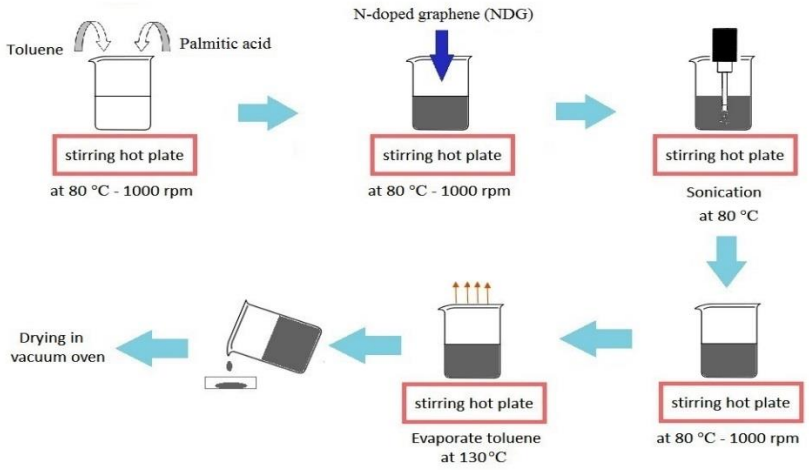

Figure 3-10: Schematic route for the sample preparation

The PA/NDG samples that were prepared by this process are seems to be naturally isotropic by taking into consideration that the NDG nano sheets had no preferential direction and haphazardly oriented. The samples were named S1to S5 for NDG mass percentage of 1 to 5wt%.

3.3.3 Reduced Graphene Oxide (RGO)

GO is highly hydrophilic due to the existence of various oxygen functional group such as hydroxyl, epoxy, carbonyl, and carboxyl functional groups on the basal plane and at the edge of each graphitic layer during oxidation. Thus, GO is easily exfoliated in polar solvents, particularly well in water by sonication or mechanical stirring because the Van der Waals interaction between the inter-sheet gallery becomes weak due to intercalated water molecules. After that, the colloidal dispersion of graphene oxide can be reduced to prepare reduced graphene oxide using several reducing agents such as

hydrazine, hydroquinone, sodium borohydride, ascorbic acid, and so forth. Among various reducing agents, hydrazine or hydrazine hydrate was one of the first reducing reagents to be used to reduce graphene oxide. However, because hydrazine or hydrazine hydrate is highly poisonous and explosive, precautions must be considered when a large amount of hydrazine is used. Many researchers have tried to look for safer and greener reducing agents with similar or more effective reduction of graphene oxide.

Reduced graphene oxide (RGO) has been shown to have promising potential in various applications due to the great thermal and electrical conductivity properties. In this study the simple method was used to prepare the PA/RGO SSPCMs by using the n-butylamine as a reducing agent and surfactant. n-butylamine is an organic compound (an amine) with the formula $CH_3CH_2CH_2CH_2NH_2$ that could be used Instead of hydrazine. Self-assembly of PA/RGO composite PCMs were achieved by using this method with low concentration of GO.

3.3.3.1 Preparation of PA/RGO Composite PCMs

The preparation procedure for the composite PCMs is shown in Figure 3-11. First 1 g of PA was melted at 80 ºC and then 0.5 ml n-butylamine was added gradually and stirred for 5 min. After that GO with different mass percentages (0.5 to 2 wt %) was added to the solution. The solution was stirred till the gelation occurred. As seen in Figure 3-11 , the prepared gels were dark-brown and highly viscous, retaining their initial shape even when the beakers were inverted. The gelation time was dependent upon the content of GO. Finally, the gels have been dried inside a vacuum oven overnight at 120 ºC to complete the reduction process. The samples were named S1to S4 for RGO mass percentage of 0.5 to 2wt%.

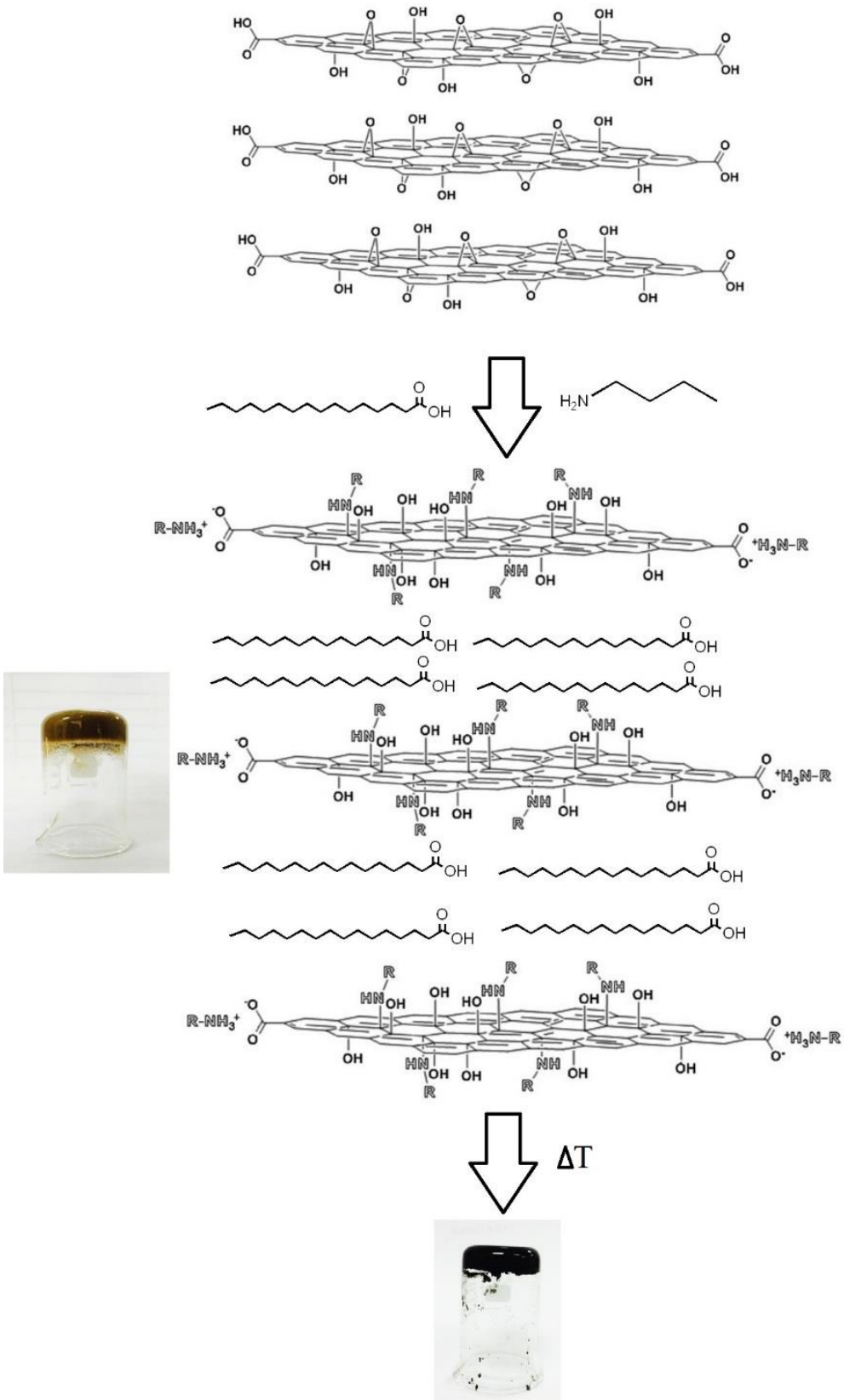

Figure 3-11: The self-assembly process of PA/RGO SSPCMs

3.3.4 Graphene Nanoplatelets

Graphene nanoplatelets (GNPs) are two-dimensional (2D) with an average thickness of 5–10 nanometers and a specific surface area of 50-750 m^2/g and can be produced of different sizes, 1 to 50 microns. These interesting nanoparticles, including short stacks of platelet-shaped graphene sheets which are identical to those found in the walls of carbon nanotubes, but in a planar form. The graphene nanoplatelets (GNPs) have drawn a lot of interest due to their excellent electrical conductivity, high mechanical properties and the in-plane thermal conductivity of GNPs is reported to be as high as 3000-5000 W/m.K (Kim et al., 2014). Further, as this is a 2D material, the heat transfer properties are expected to be much different from the zero dimensional nanoparticles and one dimensional carbon nano-tubes. Moreover, GNPs itself being an excellent thermal conductor, the graphene based nanofluids are normally expected to display significant thermal conductivity enhancement (Fang et al., 2013). The graphene nanoplates are also offered in granular form which could be dispersed in water, organic solvents and polymers with the right choice of dispersion aids, equipment and techniques.

Graphene nanoplatelets (GNPs) have special properties dependent on the number of layers, such as the saturable absorption, linear monochromatic optical contrasts and electric field assisted band gaps, which are not found in previously produced materials. These materials (Grade C, XG Sciences, Inc., USA) were used for the preparation of SSPCMs. Each grade contains particles with a similar average thickness and specific surface area. Grade C particles have an average thickness of a few nanometers and a particle diameter of less than 2 μm. The average specific surface areas are 300, 500 and 750 m^2/g and all specifications are shown in Table 3-4.

Table 3-4: Nanoparticle specification

Particle	Graphene nanoplatelets (GNPs)
Color	Black granules/powder
Carbon content	>99.5
Bulk density	0.2-0.4 g/cm^3
Relative gravity	2.0-2.25 g/cm^3
Specific surface area	300, 500 and 750 m^2/g
Particle diameter	2 µm
Peak in UV-vis spectrophotometer	265-270 nm
Thickness	2 nm
Thermal conductivity (parallel to surface)	3000 W/m.K
Thermal conductivity (perpendicular to surface)	6 W/mK
Electrical conductivity (parallel to surface)	10^7 siemens/m
Electrical conductivity (perpendicular to surface)	10^2 siemens/m

3.3.4.1 Preparation of PA/GNPs Composite PCMs

The form stable nanocomposite PCMs were prepared by vacuum impregnation method and the setup was shown in Figure 3-12 (a).The setup includes vacuum chamber, vacuum pump, vacuum meter and heater. The first step was to evacuate exiting air in GNPs pores while the vacuum pressure was monitored and controlled by vacuum meter. The GNPs were heated to 90℃ for 2h while vacuum pressure was controlled. In previous researches the melted PCM was directly impregnated but it has a high viscosity and this will affect impregnation as penetration of PCM into the porous structure becomes more challenging. In this study PCM (95 wt%) was mixed with toluene to avoid this effect and the mixture was allowed to enter the flask to cover the GNPs (5 wt%) at a temperature of 90℃.This process was done slowly to let the toluene evaporate from the mixture and only PCM will cover GNPs. This step was done in 2h to make sure that impregnation was done completely then air was allowed to enter the flask. After 30 minutes the composite PCM

was placed in the mold at room temperature to make sure that composite PCM becomes solid. The amount of PCM retained by the pores of GNPs was determined after removing extra PCM by keeping composite PCM in oven at 80℃ for 24h.The granular sample was compacted by a hydraulic press powder pelletizer under pressure of 1.5 ton as shown in Figure 3-12 (b) into pellets in a steel mold with a diameter of 20 mm. The three different samples were prepared with same method and named S1, S2 and S3 for surface area of 300, 500 and 750 m^2/g, respectively.

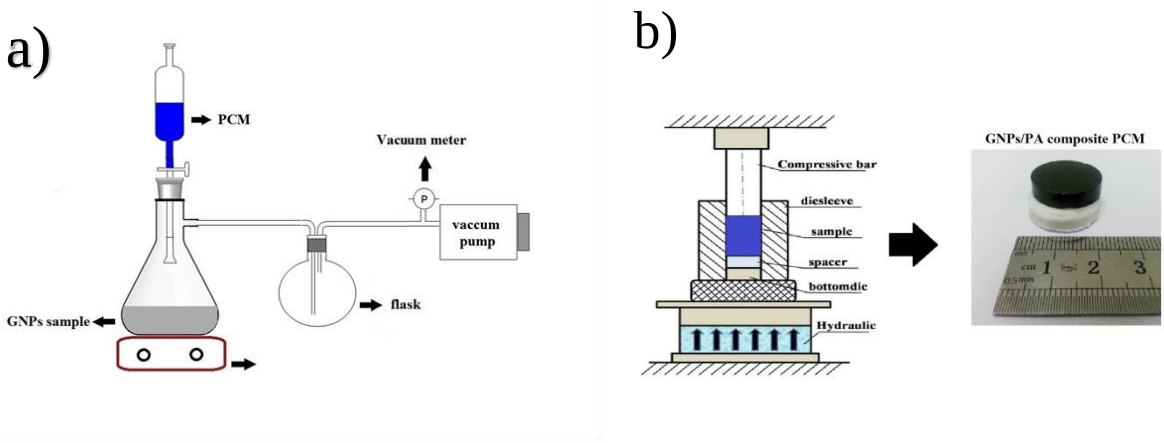

Figure 3-12: (a) Schematic diagrams of impregnation process (b) Scheme for the sample compaction apparatus

3.3.5 Carbon Nanospheres

Carbon spheres with different structure from the C_{60} cage and carbon onions have unclosed graphene layers. Compared to the studies of fullerenes, carbon nanotubes and nanofibers, reports on the research of carbon spheres are relatively few in number. Carbon spheres have similar properties to graphite or fullerene, which allows them to fabricate diamond films, lubricating materials and special rubber additives. However, an economic method of preparing large amount of carbon spheres under reasonable experimental conditions is still lacking to date. CNSs have several attractive properties that make it suitable for the energy storage applications. It has high thermal conductivity and high specific surface area (200-300 m^2/g) of CNSs is advantageous for shape-stabilization

during the phase transition of PCMs since it helps to grasp the liquid by surface tension and capillary forces (Yuan et al., 2008).This new composition has good thermal conductivity and stability during the phase change process to use in energy storage applications including solar and buildings.

3.3.5.1 Preparation of Carbon Nanospheres

Carbon nanospheres were made by the simple hydrothermal method.4g glucose (ACS reagent- Fisher Scientific) and H_2O (50ml) were mixed by stirring into a homogeneous aqueous glucose solution. The mixture was transferred into a Teflon autoclave of 60 ml capacity and placed in a reaction furnace that was maintained at 180 ℃ for 12 h, and then cooled to ambient temperature naturally. A dark precipitate was washed with absolute ethanol and dried in a vacuum oven at 60 ℃ for 8 h.

3.3.5.2 Preparation of SA/CNSs composite PCMs

2 g of Stearic acid (SA) was first dissolved in 50 ml toluene at 70 ℃, and then CNSs with various amounts (0.25 g, 0.5 g, 1 g and 2 g) was added into the solution afterwards. The solution was sonicated for 30 min at 150W to break down the CNS aggregates and obtain a homogeneous dispersion of the nano particles. The mixture was then left in a fume hood at 130 ℃ to evaporate the toluene and poured into a mold. Finally, the PCM samples have been dried in a vacuum oven overnight at 120 ℃ to eliminate SA which had not been absorbed by CNSs. The prepared composites were named PCM1 to PCM4 for different amount of CNSs that was added.

3.3.6 Activated Carbon

The potency of activated carbon (AC) as an adsorbent material is due to its distinctive properties, such as significant surface area, a high level of surface reactivity, widespread adsorption effect, and advantageous pore size. The last decade has observed much study into the synthesis of enhanced porous carbon components, motivated by

prospective applications including electrodes of supercapacitors, hydrogen storage and catalysis. The development of biomass-based porous carbon products continues to be the most productive areas in the carbon materials research owning to their exclusive characteristics such as sustainability, environmental friendliness, and continuous availability. In this research we employed a facile and cost-effictive method to make ultrahigh specific surface area and large pore volume porous carbon by using a biomass-based product, i.e., rice hull, as a precursor. We remarkably observed that by employing a simple three-section heat program, the resulting porous carbon have remarkable surface area and high pore volume that will be useful for shape stabilization of the PCMs. Because of the low thermal conductivity of the AC, GNPs were used as a filer to increase the thermal conductivity.

3.3.6.1 Preparation of Activated Carbon

As it is shown in Figure 3-13, in a regular process, the rice hull was pre-carbonized at 400 $°C$ with 5 $°C$/min for 2 h in N_2 atmosphere. Subsequently, the resulting rice hull carbon (RC) was ground into powder and carefully mixed with NaOH pellets with mass ratio of 3:1, the mixture was heated up (heating rate 5 $°C$/min) to 800$°C$ under the N2 atmosphere. The activated sample ended up being completely washed with 10 wt% HCl to eliminate any inorganic impurities after which distilled water until neutral pH, and finally dried at 80 $°C$ for 6 h.

Figure 3-13: Activated Carbon production process from rice hulls

The prepared activated carbon (AC) was mixed with water and then GNPs (750 m^2/g) with mass ratio of 1,2,4 and 6 wt% were added and bath sonicated for 10 min and finally dried at 80 $°C$ for 6 h.

3.3.6.2 Preparation of PA/AC composite PCMs

The form stable nanocomposite PCMs were prepared by vacuum impregnation method following the same process in section 3.3.4.1. The samples were named S1 to S5 for PA/AC and PA/AC/GNPs composites.

3.4 Properties Characterization

In order to optimally implement PCMs into the design of energy efficient systems, the selection of a suitable material is important. This requires the measurement of the PCMs' thermophysical properties (Yinping & Yi, 1999). Other physical and chemical properties in regards to density, chemical stability, etc. are also important, but these can be obtained with reasonable accuracy from the manufacturers. 'Thermophysical properties' are defined as the material properties affecting the transfer and storage of heat which vary with the state variables temperature, pressure, composition and other relevant variables, without altering the material's chemical identity. Past literatures have reported

that the phase change temperature, latent heat, heat capacity and thermal conductivity are the most important parameters in the experimental and numerical study of PCMs (Dolado et al., 2011; Yin et al., 2008). After the synthesis of shape stabilized composite PCMs according to the full experiment design and their powders were prepared properly, objective characterizations were carried out to assess the structure features of these novel composites by using a series of modern instrument for material analysis. The instruments involved in the study are divided to thermal, chemical and physical characterizations. The instruments involved in this study are summarized in Table 3-5.

Table 3-5: The instruments involved in the objective measurement of SSPCMs

Instruments In Full Name	Shorten	Instrument Model And Brand	Properties
Differential Scanning Calorimetry	DSC	METTLER TOLEDO 820C	Thermal Features
Thermal Gravimetry	TG/DTG	METTLER TOLEDO SDTA 851	Thermal Stability
Thermal Conductivity	KD2-PRO	DECAGON DEVICES	Thermal Features
	LFA	NETZSCH LFA 447	
Fourier Transmittance Infrared Spectra	FT-IR	PERKIN ELMER SYSTEM 2000	Chemical Structure Analysis
X-Ray Diffraction And Scattering	XRD	EMPYREAN-PANALYTICAL	System Physical Structures
Raman Scattering Spectroscopy	RAMAN	RENISHAW INVIA RAMAN MICROSCOPE	Chemical Structure Analysis
Scanning Electron Microscope	SEM	CARL ZEISS-AURIGA 60	Surface Morphology Observation
Transmission Electron Microscopy	TEM	CARL ZEISS-LIBRA120	Inner Morphology Observation
X-Ray Photoelectron Spectroscopy	XPS	PHI 5400 ESCA	Chemical Structure Analysis
Surface Area Analysis	BET	BET-AUTOSORB-IQ2	Surface Physical Properties
Atomic Force Microscopy	AFM	MULTIMODE 8, BRUKER,	Nanoscale Properties
Uv-Vis Spectrophotometer	UV	SHIMADZU (UV-1800)	Chemical Structure Analysis
Dropping Point Test	DP	METTLER TOLEDO FP83HT	Physical Structure
Electrical Resistivity	---	LCR HITESTER 3532	Electrical Properties
Infrared Camera	---	FLIR i5	Thermal Images
Thermal Cycler	---	----	Thermal Reliability
Solar-Thermal Test	----	----	Solar Performance

3.4.1 Differential Scanning Calorimetry (DSC)

Differential Scanning Calorimetry (DSC) refers to a technique whereby the thermal properties of a material can be determined through the analysis of heat flows into and out of the sample material relative to a reference sample, under different heating/cooling temperature rates. The reference is usually an empty pan identical to the sample pan (Figure 3-14). The differential heat flows are plotted against temperature, and various micro-structural transitions and thermophysical properties can be deduced from the plot. The test is done in an inert atmosphere usually nitrogen gas, which is used to remove any corrosive gases from the sample and to minimize the risk of condensation inside the DSC instrument when the temperature gets below the air dew point.

The heating/cooling temperature rates are important features of the analysis. These are usually limited to 40℃/min, above which the effects of non-linearity becomes dominant and the calibration parameters become no longer applicable (Bershteæin & Egorov, 1994). Faster temperature rates give more inherent sensitivity, but better resolution can be obtained at lower temperature rates. Resolution refers to the ability to separate close thermal events, while sensitivity refers to the ability to detect weak events. Increased resolution is always at the expense of sensitivity, and vice versa (Verdonck et al., 1999).

Furthermore, the mass of the sample, i.e. thermal inertia of the material should also be considered before choosing a rate. Small samples (< 10 - 30mg) can have faster rates, while heavier samples should have a slower rate (Bershteæin & Egorov, 1994) in order to allow for uniformity in temperature distribution in the sample and improved resolution.

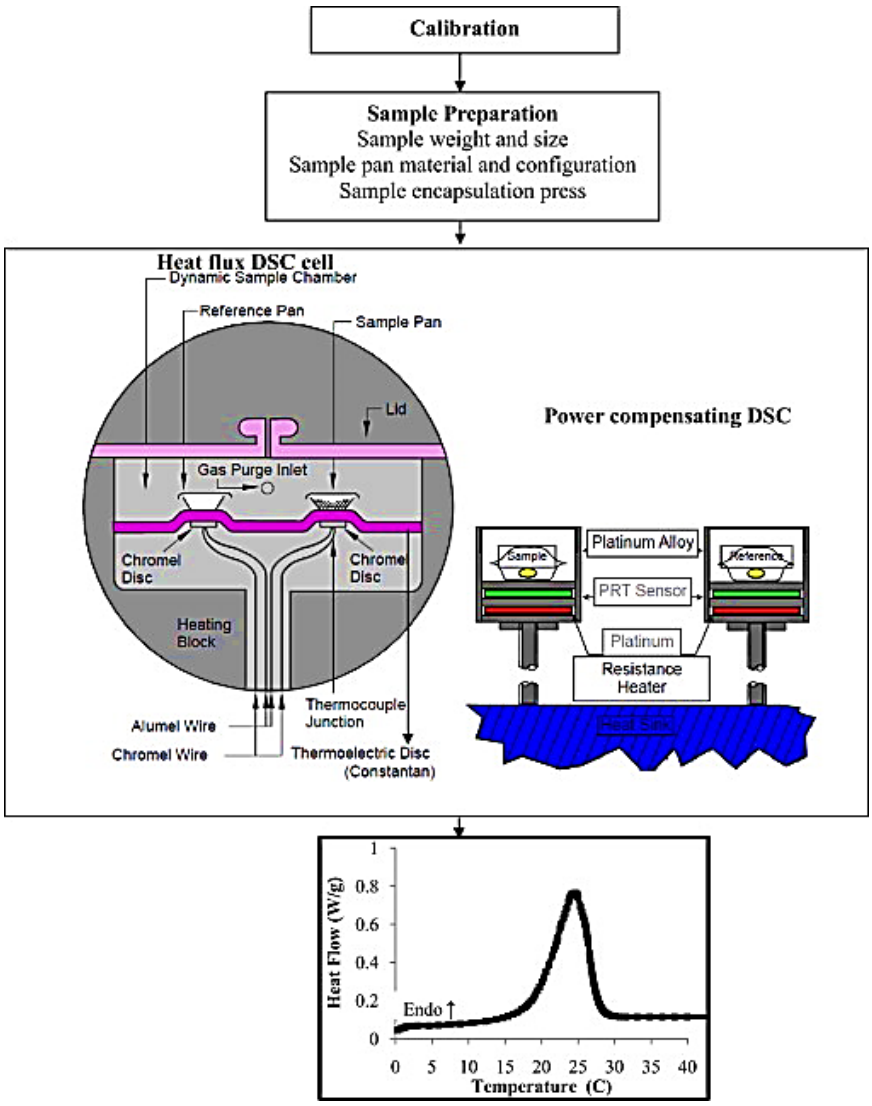

Figure 3-14: Differential scanning calorimeter sample and reference holder (Memon, 2014)

A sample of the material was placed inside the calorimeter and heated at a fixed heating rate. The amount of energy needed to maintain a fixed rate of temperature increase was measured. An endothermal or exothermal peak in the DSC thermogram denotes the melting or crystallization temperature of the tested material. The measuring principle of DSC technique is to compare the rate of heat flowing to the sample with that of an inert material which is heated or cooled at the same rate. Changes in the sample that is associated with absorption or evolution of heat cause a change in the differential heat flow which is then recorded as a peak. The area under the peak is directly proportional to the

enthalpy change and its direction indicates whether the thermal event is endothermic or exothermic.

The phase change temperature is divided into starting, peak and ending temperatures (Figure 3-15). The starting and ending temperatures are the temperatures at the intersection of extrapolated baseline and the tangents to the DSC curve drawn at the inflection points to the left and right side of the peak while the peak temperature is the temperature at the peak point of DSC curve. The thermal heat stored in the unit weight of PCM is obtained by dividing the integrated area between the baseline and the DSC curve with a temperature rising rate in the DSC test. This value is calculated automatically by the software. It is worthy to mention here that the user can choose different types of baselines such as linear, sigmoidal horizontal, sigmoidal tangent and extrapolated to calculate the thermal energy stored in the unit weight of PCM.

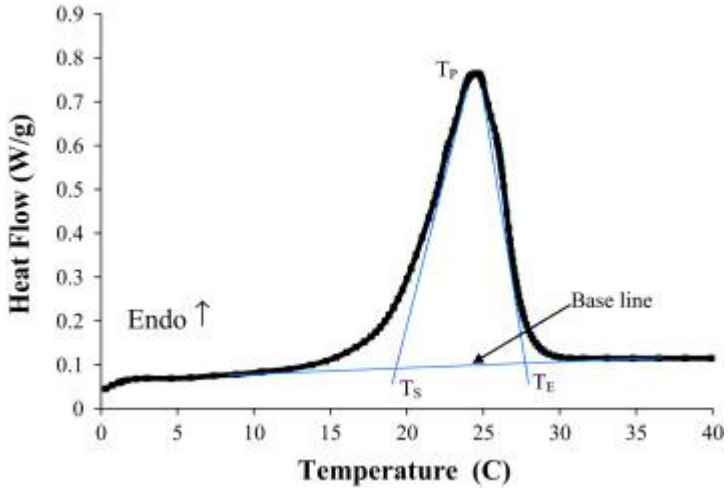

Figure 3-15: DSC curve

In the present study, the heat of fusion or crystallization of enthalpy (ΔH), the onset melting and crystallization temperatures as well as the property of super-cooling for each pure PCMs and SSPCMs were measured. The DSC measurement was carried out by the METTLER TOLEDO 820C (Error ± 0.25–1°C) with a working range of -50~500℃.For this measurement, the samples with 5~10mg in weight were heated from

30 to 100℃ at the scanning velocity of 5℃/min. The temperature was maintained at 35℃for 5 minutes and then cooled down to -10℃ as one measure circle was finished. Nitrogen atmosphere was maintained during the whole process for all measurements. Hence, crystallization exotherms and melting endotherms for various SSPCMs with different supporting materials were obtained.

3.4.2 Thermal Gravimetry and Derivative Thermogravimetric

Thermogravimetric analysis (TGA) is a technique in which the change in the sample mass was analyzed while the sample is subjected to a temperature programme. TGA is mainly used to characterize the decomposition and thermal stability of materials under different conditions, and to examine the kinetics of physical-chemical processes occurring in the sample.

In the thermal gravimetry analysis, a sensitive balance is used to measure the changing in weight of a sample as a function of temperature. Typical applications in material characterization of thermal gravimetry (TG) include the assessment of thermal stability, decomposition temperature, material composition, chemistry reaction kinetics and purity determination etc. Derivative thermogravimetric (DTG) analyses can be calculated by the differential of change in sample weight on time. DTG data denotes the rate of change in weight (dm/dt) of a sample which is heated at a controlled manner.

In the present study, the samples were heated from the ambient temperature (20℃) to 600℃ in nitrogen atmosphere with the gas flow rate of 50ml/min (nitrogen atmosphere) at the heating rate of 10ºK/min. The weight of different samples was 8~15mg in all cases. During the heating period, both the weight loss and temperature data were recorded. METTLER TOLEDO-SDTA 851(Error ± 5 μg) equipment was used in the test with the testing range of 25 to 1300℃.

3.4.3 Thermal Conductivity

Form-stable PCMs attracted a vast attention due to increment in thermal conductivity compared to the pure PCMs. Measuring these thermo-physical properties was a challenge for a long time since different methods and techniques presented different results. Thus, the method which is going to be used would be significant to lower the measurement error and uncertainty as much as possible. In this study, two thermal conductivity measurement methods were employed including Transient hot-wire techniques and laser flash method.

Generally, Fourier's law for conduction heat transfer can be utilized to measure thermal conductivity of a material. Temperature difference can cause heat transfer through materials which is known as conduction heat transfer. Thermal conductivity is particular properties of the material which can differ from one material to another and can be calculated by Equation (3-1):

$$k = \frac{q/A}{\Delta T/L} \tag{3-1}$$

where, k is thermal conductivity, q is magnitude of heat transmission, ΔT is temperature difference, A is cross sectional area and L is the length (Bitaraf Haghighi et al., 2012). To simplifying calculations, one-dimensional temperature filed and steady state flow would be considered.

3.4.3.1 Transient Hot-Wire (THW) method

This can be known as the most regular and the oldest method of measuring thermal conductivity. Comparing other methods, it can be known as a very fast measurement method and conceptual design of the apparatus is simple as well. It has been used to measure thermal conductivity of powders at the beginning. However, it has been improved by many researchers. The THW method is based upon using a long, thin platinum wire as a dual line heat source and temperature sensor. This is possible due to

the relatively unique relationship between the temperature and thermal characteristics of platinum. The platinum filament is fully placed within the material for which the thermal conductivity is to be determined, and a step increase in the electrical power supplied to the wire is introduced. This allows the platinum wire to heat up due to resistive heating. The excess heat from the hot filament is rejected to the surrounding through conduction. Simultaneously, while this heating is occurring, the relative change in resistivity of the wire is being measured through a two or four wire resistive measurement system. The surface temperature of the hot wire and therefore the temperature of the immediate surrounding can be calculated based upon this approach. The measured value of total input power, and power lost to the surrounding, combined with the overall change in resistivity of the platinum wire due to electrical heating are collected; these values, in conjunction with the measured experimental time and dimensional parameters of the hot wire setup, can be used to back calculate the thermal conductivity of the material of interest.

In this study KD2-Pro system was used to measure the thermal conductivity of the some SSPCMs. The KD2 Pro resolves to 0.001℃ in temperature by utilizing special algorithms to analyze measurements made during a heating and a cooling interval. Algorithms also separate out the effects of the heat pulse from ambient temperature changes. The prepared samples were placed in proper container in circulating bath while the temperature was controlled and dual needle apparatus was used to measure the thermal conductivity of the samples.

3.4.3.2 Laser Flash Technique

The Laser Flash technique is based on the measurement of the thermal transient of the rear surface of the sample when a pulsed laser illuminates the front and it avoids interferences between the thermal sensor and the heat source. The physical model of the Laser Flash measurement supposes to have a single pulsed heat source (delta like), for

example a laser shot, on the sample front surface. The study of the thermal transient of the rear surface provides the desired thermal information. The temperature of the rear face is measured with an infrared detector and it can be expressed mathematically as a function of several variables that are grouped into dimensionless parameters. These variables include sample geometry, thermal diffusivity and heat loss from the sample.

The laser flash technique (Netzsch LFA 447 NanoFlash) was used to measure the thermal diffusivity of prepared samples at 35℃. The thermal conductivity may also be derived from the thermal diffusivity when the specific heat and the sample bulk density are known as shown in equation (3-2):

$$K = \alpha . \rho . C_p \quad (3\text{-}2)$$

Where k is the thermal conductivity (W/ (m·K)), α is thermal diffusivity (m^2/s), ρ is density (kg/m^3) and C_p is specific heat capacity (J/(kg·K)).

3.4.4 Fourier-Transform Infrared (FTIR) Spectroscopy

Infrared spectroscopy was used to identify the chemical groups within a substance based on the concept that the chemical bonds present in a materials would vibrates at a characteristic frequency. Imaging, a molecule bond will absorb energy and vibrate when an infrared beam passes through the substance at a certain frequency. When molecules undergo transitions between quantum states corresponding to two different internal energies, spectra emission or absorption will take place. The energy difference ΔE, is related to the frequency of radiation emitted or absorbed by the quantum state as given by Bohr Equation:

$$\Delta E = hv \quad (3\text{-}3)$$

where h is Planck`s constant, $h=6.6262\times10^{-34}$ JS, and v is equivalent to the classical frequency.

Infrared frequencies in the wavelength range of 1~50μm (10000cm^{-1} ~200cm^{-1}) are associated with molecule group vibration and vibration-rotation spectra. Each bond present in a molecule group is capable of performing a number of different modes of vibration, such as stretching and bending, scissoring, rocking, wagging and twisting. A transmittance or absorbance spectrum can be plotted, showing that at which wavelengths the sample absorbs the IR rays. This allows an interpretation of the nature of bonds present in the material. Therefore, the appearance of a number of peaks can be attributed to the presence of a particular chemical structure (Pasquini, 2003).

FTIR spectroscopy was performed using a Perkin Elmer Spectrum 100 infrared spectrometer. SSPCMs were analyzed in an attenuated total reflectance (ATR) detector over a 400-4000 cm^{-1} wavenumber range at a resolution of 4 cm^{-1}.

3.4.5 X-Ray Diffractometry

X-Ray Diffraction and Scattering (XRD) is the most important non-destructive tool to analyze all kinds of substances ranging from fluids to powders. X-rays are an ideal probe for the study of materials since the wavelength of X-rays is of the same order as the distance between the atoms in the materials. XRD offers a deep insight into structure, crystalline phase composition, material properties such as stress and texture, nano-structure and thin films etc.

The portion of amorphous region in the specimen scatters the X-ray beam and gives a continuous background on the diffraction spectrum, while the crystalline portion reflects the radiation according to the Bragg`s theory showing the diffraction peaks in a spectrum. The distance between the parallel planes inside the crystallites can be calculated by the Bragg`s equation (Cowie, 1991):

$$d = \frac{n\lambda}{2\sin\theta} \tag{3-4}$$

Where θ is an incident angle, λ is the wavelength of radiation and n is an integer indicating the order of diffraction.

The dried sample powders were put into a holder in a dense and plate state. X-ray diffraction data were taken by the EMPYREAN-PANALYTICAL XRD system diffractometer at the power of 40KV and 10mA current with Cu (k=1.54178 Aº) irradiation. The XRD patterns were obtained in the range of 2θ =5~80º and the scanning speed was 0.02º/second.

3.4.6 Raman Spectroscopy

Raman spectroscopy is a spectroscopic technique used in the condensed matter of physics and chemistry to study the vibrational, rotational and other low-frequency mode in a system. It relies on inelastic scattering or Raman scattering of monochromatic light, usually from a laser in the visible, near infrared, or near ultraviolet range. The laser light interacts with photons or other excitations in the system, resulting in the energy of the laser photons being shifted up or down. The shift in energy often gives information about the photon modes in a system (Siesler et al., 2008). The basic principle of Raman spectroscopy is shown in Figure 3-16.

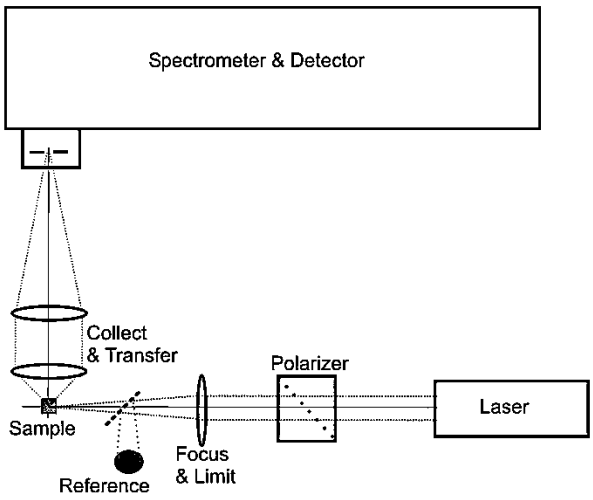

Figure 3-16: The basic principle of Raman spectroscopy measurement

The Raman Effect occurs when the light impinges upon a molecule and interacts with the electron cloud of the bonds of that molecule. The incident photon excites one of the electrons into a virtual state. For the spontaneous raman effect, the molecule will be excited from the ground state to a virtual energy state, and relax into a vibrational excited state generating Stokes Raman scattering. If the molecule was already in an elevated vibrational energy state, the Raman scattering is then called anti-Stokes Raman scattering. A molecular polarizability change or the amount of deformation of the electron cloud, with respect to the vibrational coordinate is required for the molecule to exhibit the Raman Effect. The amount of the polarizability change will determine the intensity, whereas the Raman shift is equal to the vibrational level that is involved.

Raman spectroscopy is commonly used in chemistry to detect vibrational information which is very specific for the chemical bonds in molecules. It therefore provides a fingerprint through which the molecule can be identified. The fingerprint region of organic molecules is in the range of 500-2000 cm^{-1}.

The Raman scattering spectroscopy was carried out by the instrument of RENISHAW INVIA RAMAN MICROSCOPE at room temperature with backscattering

geometry and 1800g/mm grating. The laser source for the Raman measurements was Argon laser operating at 633nm with the output power of 150mW. The focusing area of the laser beam was around 2μm. The detector was an electronically-cooled CCD with the resolution of 1024×256 pixels. The spectra collection time was kept at 2 minutes and each sample was scanned from 100 cm^{-1} to 3200cm^{-1} of Raman shift.

3.4.7 Scanning Electron Microscopy

Scanning Electron Microscopy (SEM) involves the electron microscope capable of producing high resolution images and giving a three-dimension appearance of a sample surface. SEM techniques are used to examine the surface morphology and structures of a material.

In SEM a fine probe of electrons with energies typically up to 40 keV is focused on a specimen, and scanned along a pattern of parallel lines. Various signals are generated as a result of the impact of the incident electrons, which are collected to form an image or to analyze the sample surface. These are mainly secondary electrons, with energies of a few tens of eV, high-energy electrons backscattered from the primary beam and characteristic X- rays (Goldstein et al., 1981). In SEM the nature of the sample determines the preparation of the sample, since appropriate samples may be examined directly with little or no prior preparation. Unfortunately, most polymers present specific problems making them inappropriate. Therefore proper sample preparation is necessary prior to characterization including conductive coatings through evaporation or sputtering.

To determine the morphology of the fractured surfaces in this study, a CARL ZEISS-AURIGA 60 scanning electron microscopy was used and the analysis was done at room temperature. The samples were fractured by freezing them in liquid nitrogen, and simply breaking the specimen into appropriate size to fit the specimen chamber. The

fractured samples were gold coated by sputtering to produce conductive coatings onto the samples.

3.4.8 Transmission Electron Microscopy

Transmission electron microscopy (TEM) is also an imaging technique using a beam of electrons transmitting through a specimen, and then an image is formed TEM will also be applied to characterize the surface properties and inner structure of a specimen, as well as to examine the nature of nano-particles in the polymer matrix (Wang, 2000). The maximal penetration thickness of an electron beam for TEM test is about 100 to 500nm.

The samples used for TEM were prepared by drying a drop of aqueous suspension placed on a carbon coated copper grid. Inner structures of the composite PCMs were investigated by the CARL ZEISS-LIBRA120 with an accelerating voltage of 120,000 and a vacuum ratio of 10^{-7} Torr.

3.4.9 X-Ray Photoelectron Spectroscopy

X-ray Photoelectron Spectroscopy (XPS) was developed in the mid-1960s by Kai Siegbahn and his research group at the University of Uppsala, Sweden. The technique was first known by the acronym ESCA (Electron Spectroscopy for Chemical Analysis). The variation of photo peak energy with chemistry allowed the development of this surface sensitive chemical analysis method. X-ray photoelectron spectroscopy works by irradiating a sample material with monoenergetic soft x-rays causing electrons to be ejected. Identification of the elements in the sample can be made directly from the kinetic energies of these ejected photoelectrons. The relative concentrations of elements can be determined from the photoelectron intensities. An important advantage of XPS is its ability to obtain information on chemical states from the variations in binding energies,

or chemical shifts, of the photoelectron lines. The relationship governing the interaction of a photon with a core level is:

$$KE = h\nu - BE - e\Phi \quad (3\text{-}5)$$

Where KE is Kinetic Energy of ejected photoelectron, hν is characteristic energy of X-ray photon, BE is Binding Energy of the atomic orbital from which the electron originates and eΦ is spectrometer work function.

In this study X-Ray photoemission spectrometer (XPS-PHI 5400 ESCA) with an Al-Kα (hν=1486.69 eV) X-ray source was used to identify the elements' states in prepared materials.

3.4.10 UV-Vis spectrophotometer

Ultra Violet-Visible spectrophotometer is one of the most common methods used to investigate stability of nanofluids due to its ease of use and fast analysis. It has been utilized to magnitude stability of suspensions in nanofluids; however, viscosity of base fluid would be known as one constraints of this method. This method is based on different wavelengths of light in which it can be scattered or absorbed by other materials. It is known when light is passing through fluids, intensity of it changes by absorption and scattering.

The light transmission of all graphene samples was measured with a Shimadzu UV spectrometer (UV-1800) operating between 190 and 1100 nm for verifying purposes.

3.4.11 Surface Area Analysis

Surface area largely determines many physical and chemical properties of materials. Physical adsorption of molecules, heat loss or gain resulting from that adsorption, swelling and shrinking, and many other physical and chemical processes are

closely related to surface area. When a gas or vapor phase is brought into contact with a solid, part of it is taken up and remains on the outside attached to the surface. In physisorption (physical adsorption), there is a weak Van der Waals attraction between the adsorbate and the solid surface. An Adsorption Isotherm is obtained by measuring the amount of gas adsorbed across a wide range of relative pressures at a constant temperature (typically liquid N2, 77K). Conversely desorption Isotherms are achieved by measuring gas removed as pressure is reduced. That is useful to characterize porous materials allowing for the determination of specific surface area, pore size distribution and pore volume.

The Brunauer, Emmett and Teller (BET), is the most common method used to describe the specific surface area. In this study Brunauer–Emmett–Teller method (BET-Autosorb-iQ2) was used to measure specific surface area and pore distribution of the carbon samples.

3.4.12 Atomic Force Microscopy

The Atomic force microscopy (AFM) consists of a cantilever with a sharp tip (probe) at its end that is used to scan the specimen surface. The cantilever is typically silicon or silicon nitride with a tip radius of curvature on the order of nanometers. When the tip is brought into proximity of a sample surface, forces between the tip and the sample lead to a deflection of the cantilever according to Hooke's law (Cappella & Dietler, 1999). Depending on the situation, forces that are measured in AFM include mechanical contact force, van der Waals forces, capillary forces, chemical bonding, electrostatic forces, magnetic forces (see magnetic force microscope, MFM), Casimir forces, solvation forces, etc. Along with force, additional quantities may simultaneously be measured through the use of specialized types of probes (see scanning thermal microscopy, scanning joule expansion microscopy, photothermal microspectroscopy, etc.). Typically, the deflection is measured using a laser spot reflected from the top surface of the cantilever into an array

of photodiodes. Other methods that are used include optical interferometry, capacitive sensing or piezoresistive AFM cantilevers. These cantilevers are fabricated with piezoresistive elements that act as a strain gauge. Using a Wheatstone bridge, strain in the AFM cantilever due to deflection can be measured, but this method is not as sensitive as laser deflection or interferometry. Atomic force microscopy (MultiMode 8, Bruker, Germany) in tapping mode was used to show the size of the prepared GO.

3.4.13 Dropping Point Test

The dropping point is defined as the temperature at which the first drop of a melted sample of the substance under investigation flows out of the bottom orifice of a standard dropping point cup on slow heating. The composite PCMs were placed and pressed into a sample cup and heated at a rate of $2°C$/min until the first drop was detected. The shape stability of composite PCMs was analyzed by using Mettler Toledo FP83HT Dropping Point Cell to investigate temperature of leakage for melted PCMs from SSPCMs.

3.4.14 Electrical Resistivity

In many works they have presented this properties for future applications used as latent heat storage and release units for thermal management of computers, electrical engines, solar power plants, and for thermal protection of electronic devices. The electrical resistance of PCM composites was measured with a LCR HiTESTER 3532 meter. The resistance of the sample was measured in the frequency range from 0.6 Hz to 100 kHz. Electrical resistivity was calculated from the resistance values at room temperature. The electrical resistances of the composite PCMs were measured and resistivity of samples was calculated by taking the geometry of the sample into account using the following equation:

$$\rho(\Omega.\,\mathrm{m}) = \mathrm{R}\left(\frac{\mathrm{A}}{\mathrm{L}}\right) \tag{3-6}$$

Where R is the electrical resistance of a uniform specimen at 1Hz, L is the length and A is the cross-sectional area of the specimen.

3.4.15 Thermal Cycler

To determine the thermal stability and reliability of the shape stabilized composite PCMs during melting and freezing process, a thermal cycling test was done using a thermal cycling system of in-house design (University of Malaya). The thermal cycling system was designed to operate between 30 and 80°C. The schematic and picture of the thermal cycling system are shown in Figure 3-17 . The tests were done by fan and heater as cooling and heating parts, digital Indicating Controller (Brian Child-P41) for controlling of melting and freezing process, communication converter (Autonics-SCM-US48I) to transfer data to PC and controller program, relay (ANV) to control heater and power supplies for fans and heater. The cartridge heater was located behind the PCM container and a thermocouple was placed inside the PCM to check the temperature and transfer data to digital Indicating Controller. First, the specified amount of PCMs was placed inside the container and the thermocouple was carefully placed inside the PCM to measure temperature and send data to communication converter. Second, by operating program in PC cycling started and melting was done by heating up to 80 °C and then immediately freezing was started by switching off the heater and starting the fan till 30°C . The temperature variations of composites was automatically recorded in PC by accuracy of ±0.1 ℃.

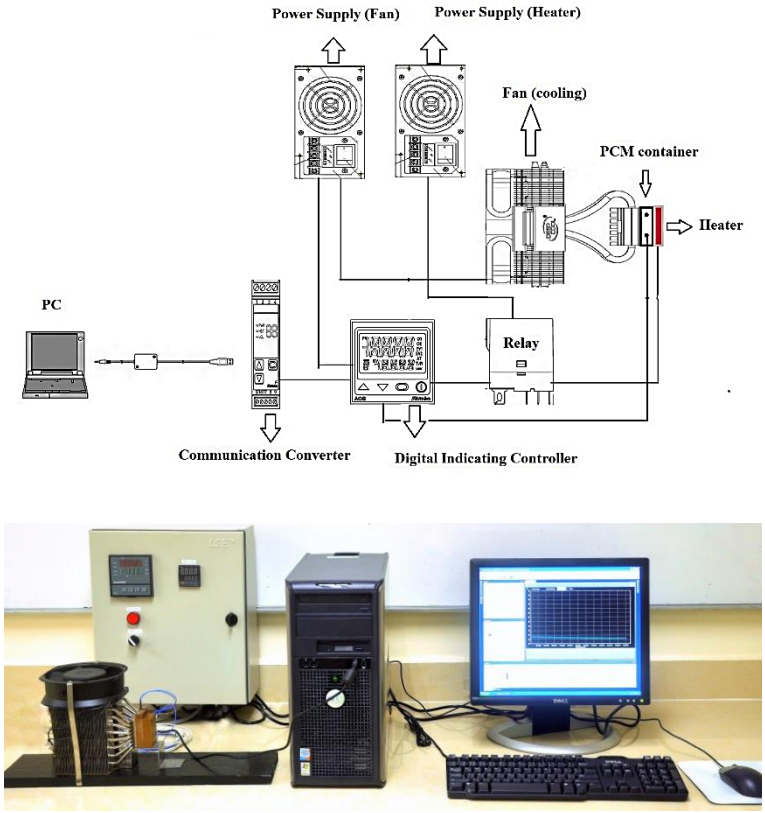

Figure 3-17: Accelerated thermal cycler

3.4.16 Solar-Thermal Test

The Specimens having diameter of 20 mm and thickness of 3 mm were prepared for the solar-thermal test. Figure 3-18 demonstrates the apparatus for the solar heating/cooling thermal examination. As can be seen in the Figure 3-18 , a specimen which has a thermal meter placed on its center was fixed to the holder box that was thermally insulated by plastic foam panels and had interior dimensions of 200 × 200 × 300 mm^3. A 150 W infrared lamp functioned as the thermal radiation supply through the heating process. Inside the box, the specimen firstly went through a 25 min long heating process. It was subsequently cooled down to room temperature without the help of cooling instruments. The temperature of the specimen's surface as well as the temperature inside the box were recorded by the data logger and computer as it's shown in Figure 3-18

.

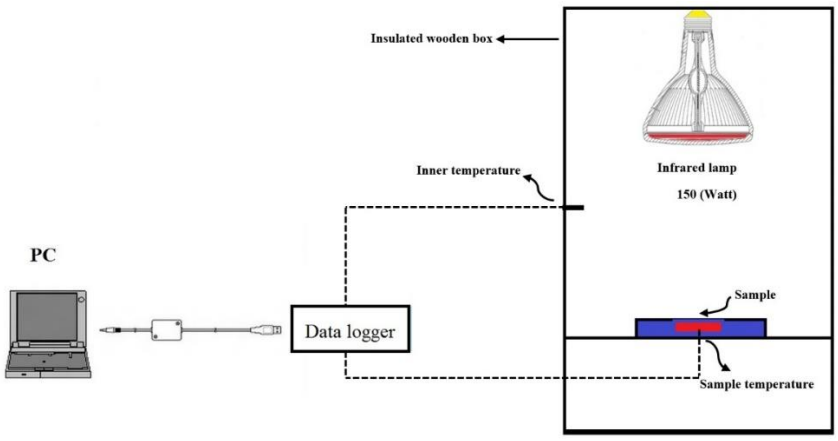

Figure 3-18: The schematic of the solar-thermal apparatus

3.5 Summary

Based on the conventional techniques of fabricating SSPCMs, novel shape stabilized PCMs with composite structures incorporated with carbon materials have been manufactured successfully. Furthermore, experimental parameters have been determined according to the previous experience and the preliminary studies.

The SSPCMs were characterized by a series of modern analysis techniques and instruments. SEM and TEM were carried out to observe the surface morphology, cross section and inner structure. FT-IR and Raman scattering spectroscopy were applied to analyze the feature of chemical structure. XRD technique was used to detect the crystal structure and EDX was employed for surface elemental analysis. DSC was used to measure the thermal capacity and properties, super-cooling and melting enthalpy of the SSPCMs. The thermal stability of microcapsule was determined by the thermalgravimetry (TG). The thermal conductivity of the prepared SSPCMs also were measured by two methods (hot wire & laser flash) to investigate the effects of carbon additives on thermal conductivity of the pure PCMs. The thermal cycling and solar adsorption test also were introduced to investigate thermal performance of the prepared SSPCMs.

CHAPTER 4

RESULTS AND DISCUSSION

4.1 Introduction

This chapter evaluates the chemical, physical and thermal properties of prepared SSPCMs. The structural, morphological and thermal features of the newly developed SSPCMs were evaluated by a series of advanced instruments and characterization technologies, such as the DSC, TGA, FT-IR, Raman spectroscopy, TEM, SEM, XRD and LFA. The thermal reliability of prepared SSPCMs were investigated by employing thermal cycler for large number of heating and cooling process.

4.2 Graphene Oxide SSPCMs

4.2.1 Graphene Oxide Characterization

Graphene oxide (GO) is highly functionalized with decorating polar groups such as carboxyls, hydroxyls, diols, etc, on irregular-sized graphene-like domains, which deliver an excellent solubility of the GO in organic solvents. However, polar groups on GO inevitably introduce structural defects on fine pattern of pristine graphene, destroy conjugation among sp^2 hybridized carbon atoms as well as interconnection between of graphene-like domains, and thereby significantly reduce thermal conductance of GO. However, it has higher specific surface area to adsorb liquids as well as higher thermal conductivity compare to organic PCMs. Here, GO is prepared as detailed in experimental section. Briefly, graphite flakes are oxidized by a mixture of $KMnO_4$ and concentrated acids. GO prepared by this method was characterized carefully to understand its structure and properties. As shown by Figure 4-1(a), an AFM height image indicates the thickness of the GO sheets ranges from 0.8 to 1.2 nm, corresponding to 1 to 4 atomic graphene layers. The crystalline and morphology structure of GO were studied by SEM and TEM.

Figure 4-1 (b and c) shown GO sheets and it was cleared that the size of a few micrometers and it tends to scroll on sheet edges, which a natural form of graphene nanosheets (Zhang et al., 2012b). The surface area and pore diameter distribution of GO was measured by BET and it's shown in Figure 4-1(d). The pore diameter and its distribution for GO sheets indicated the highest volume of pore size of 8 nm pore diameter.

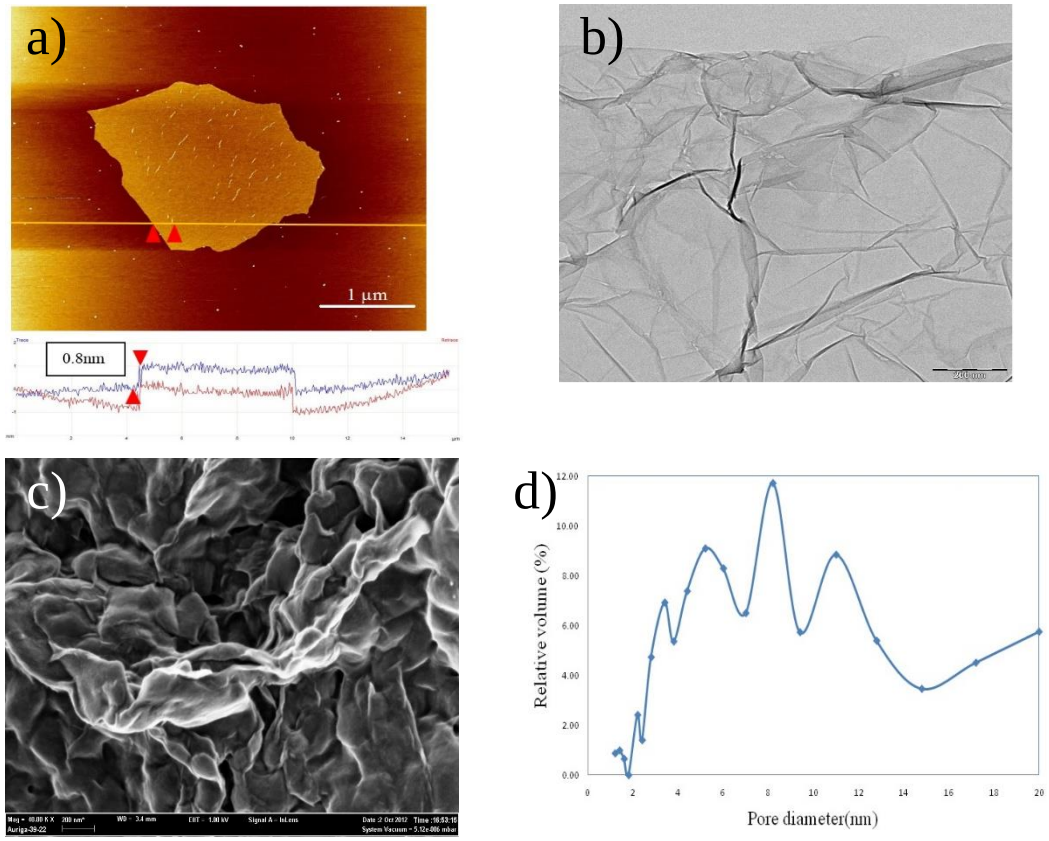

Figure 4-1: a) AFM image , b) TEM image , c) SEM image, d) Pore distribution of the GO

As shown in Figure 4-2 (a), GO solution shows two bands: a maximum peak was at 228 nm, which was related to the π- π* transition of the aromatic C–C bond and a weak shoulder at 300nm due to n– π* transition of C=O bond. Figure 4-2 (b) shows the XRD features of GO that presents one sharp peak at $2\theta = 9.7°$, corresponding to d-spacing of 0.906 nm, and it was due to the intercalation of water molecules and the formation of

oxygen containing functional groups between the layers of the graphite. FT-IR spectrum of prepared GO is shown in Figure 4-2 (c). For GO, several strong characteristic peaks at 1723 (C=O carboxyl or carbonyl stretching vibration), 1387 (O–H deformations in the C–OH groups), 1224 (C–OH stretching vibration) and 1062 cm^{-1} (C–O stretching vibrations in C–O–C in epoxide) are observed and was confirmed by the literature (Wu et al., 2012).

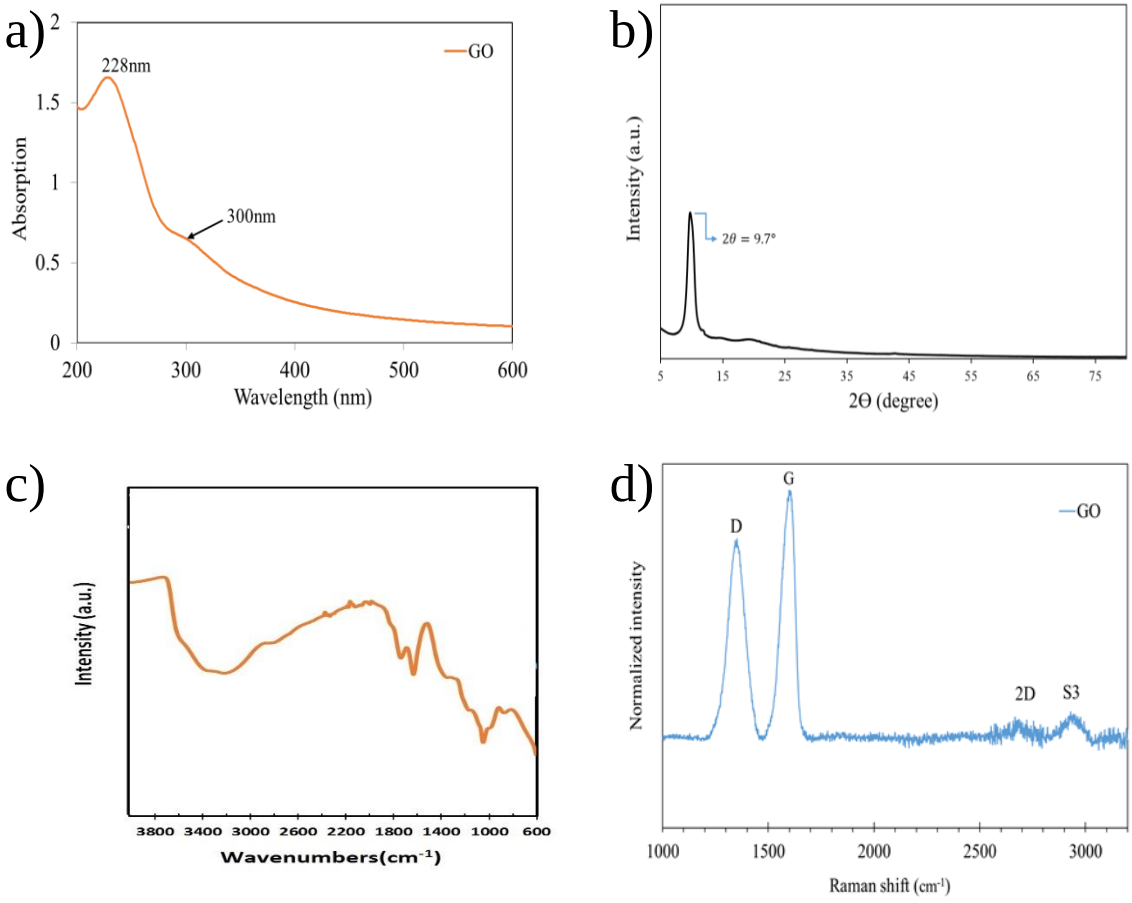

Figure 4-2: a) UV–vis spectrum , b) XRD pattern, c) FT-IR spectrum, d) Raman spectrum of the GO

The structure, defect levels, and crystallinity of the graphene oxide sheets were studied by further structural characterization using Raman spectroscopy and it's shown in Figure 4-2 (d). The Raman spectrum of GO displayed a band at 1595 cm^{-1} named the "G band" and another band at 1360 cm^{-1} named the "D band". The G band represents the planar configuration of sp^2-bonded carbon that makes up graphene, and the D band is due

to the breathing modes of six-atom rings and requires a defect for activation. From these results it can be concluded that the GO was synthesized successfully according to the literature.

4.2.2 Paraffin/Graphene Oxide SSPCM

In this research impregnation method is used for incorporation of paraffin as PCM in porous graphene oxide (GO). The impregnation method is one of the simplest and also cheapest methods while the amount of PCM impregnated can be increased by using vacuum during this process. The procedure was done for four different graphene oxide (GO) sheets made by using the same method and all analyses performed for different sheets to get the maximum mass percentage of impregnated paraffin into the GO pores. The effects of GO on thermal and chemical properties of paraffin was investigated by several characterization methods that will be explained in following sections.

4.2.2.1 FT-IR Spectra of Paraffin/GO SSPCM

Figure 4-3 shows the FT-IR results for paraffin wax and paraffin/GO composite SSPCM. The peaks at 2917.02 and 2851.57 cm^{-1} are the symmetrical stretching vibration peaks of $-CH_2$ in paraffin. The peaks at 1459.17 and 720 cm^{-1} are the bending vibration peak of $-CH_3$ in paraffin. It can be clearly seen from both FT-IR spectra that there is no shift in the above main absorption peaks while in the composite PCM can clearly indicate paraffin absorption peaks. This results shows that there is no chemical reaction between functional groups of paraffin and GO. The paraffin was impregnated in pores of GO sheets and leakage of paraffin from composite PCM was prevented.

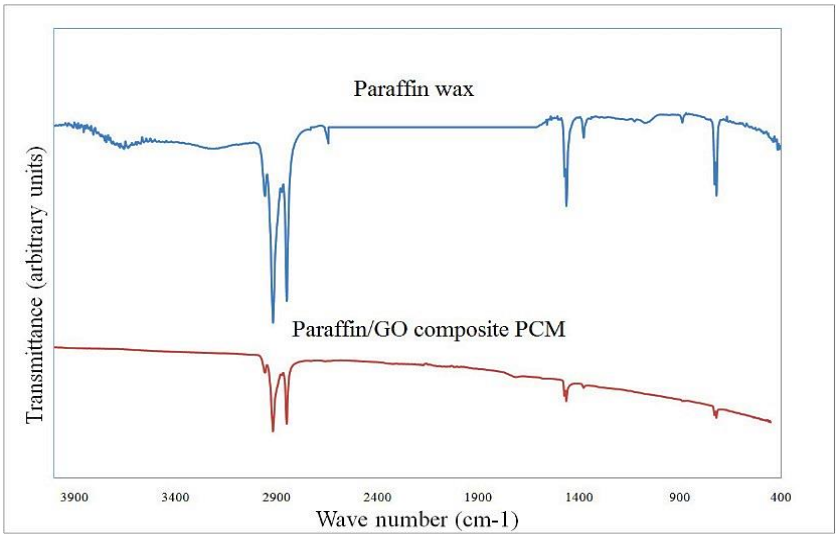

Figure 4-3: FT-IR spectra of paraffin and form-stable paraffin/GO composite PCM.

4.2.2.2 Morphology of Paraffin/GO SSPCM

In Figure 4-4, the black and white parts are paraffin and GO substances within the composite PCMs, respectively. Taking GO morphology in Figure 4-1 (c) as an example to examine the morphology of the SSPCM, it possesses a relatively compact morphology with uniformly distributed paraffin. Additionally, an obvious interspace between graphene sheets and paraffin particles was observed, which should be due to the volume contraction related to the crystallization of paraffin. This will help composite material retains its form without having leakage of the melted paraffin during phase change procedure.

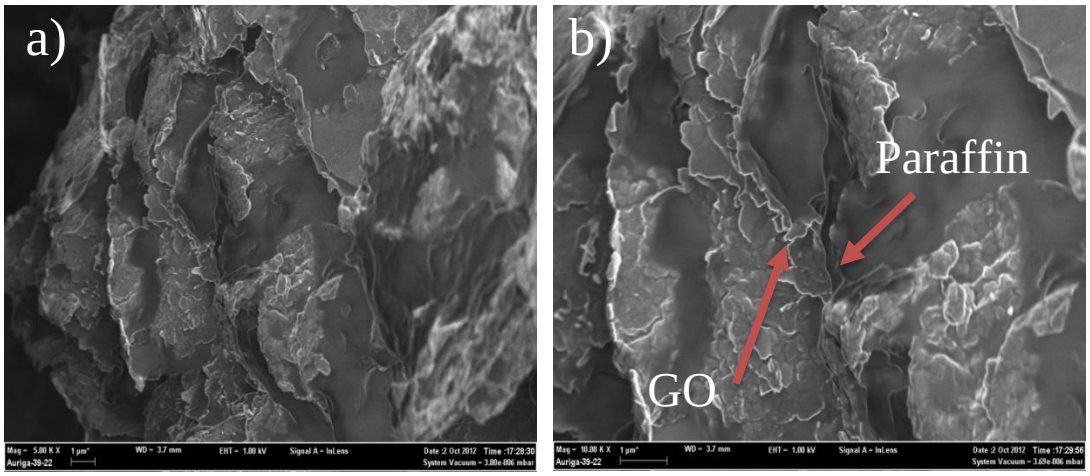

Figure 4-4: SEM images of the paraffin/GO composite PCM (a)(x 5K).(b)(x10K)

4.2.2.3 Thermal properties of paraffin/GO composite PCM

DSC analyses results are shown in Figure 4-5 and Figure 4-6 for the pure paraffin wax, PCM1, PCM2, PCM3 and PCM4. As can be seen in both figures, two main transition peaks were clearly observed, in which the sharp or main peak should be attributed to the heterogeneously nucleated rotator–liquid transition which represents the solid–liquid phase change of the paraffin and the minor peak at the left side of the main peak to the homogeneously nucleated crystal–rotator transition corresponds to the solid–solid phase transition of paraffin (Zhang et al., 2012a). The thermal properties of the pure paraffin and both composite PCMs, such as transition temperatures, phase change temperatures and the latent heat obtained by the DSC measurements are summarized in Table 4-1. As can be seen in Table 4-1, the melting and solidifying temperatures are determined to be 53.46℃ and 42.25℃ for the paraffin wax and 53.57℃ and 44.59℃ for the PCM4, respectively. The melting and solidifying latent heats are measured to be 130.92kJ/kg and 132.31kJ/kg for the paraffin wax, 63.76kJ/kg and 63.89kJ/kg for the PCM4, respectively.

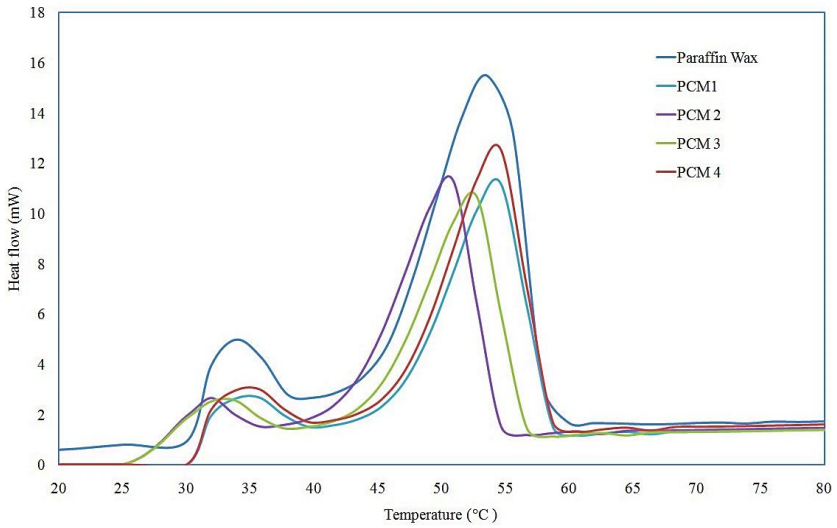

Figure 4-5: Melting DSC curves of the Paraffin Wax and PCM1–PCM4.

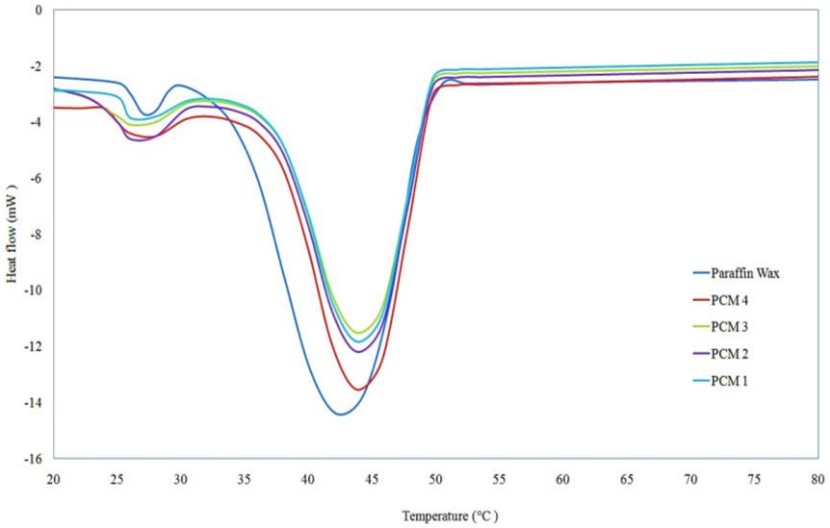

Figure 4-6: Solidifying DSC curves of the Paraffin Wax and PCM1–PCM4.

In the composites, during the melting and solidifying process only paraffin absorbs and releases thermal energy. So high latent heat storage capacity in composite PCM is the result of high phase change material content. The mass percentage of PCM (namely paraffin in this case) is calculated according to Fang et al. (2011) as follows:

$$\mathrm{PCM(wt\%)}=\frac{\Delta \mathrm{H_{PCM}}}{\Delta \mathrm{H_{Paraffin}}}\times 100\% \qquad (4\text{-}1)$$

where PCM (wt%) represents the mass percentage of paraffin in the composites, $\Delta \mathrm{H_{PCM}}$ indicates the melting latent heat of the composites, and the $\Delta \mathrm{H_{Paraffin}}$ shows the

melting latent heat of pure paraffin as determined by the DSC test. Hence, the PCM mass percentages of PCM 1, PCM 2, PCM 3 and PCM 4 were 47.8 wt%, 47.39 wt%, 44.81 wt% and 48.3 wt%, respectively. The highest mass percentage of paraffin in GO sheets at 48.3 wt% for PCM 4 that melts at 53.57℃ with a latent heat of 63.76kJ/kg and solidifies at 44.59℃ with a latent heat of 64.89kJ/kg. The differences between melting and solidifying temperatures of paraffin and PCM composites from Table 4-1 shows that the supercooling degree of composite PCMs is smaller than paraffin wax during solidification process. These results shows that GO as supporting material protect paraffin due to the porous wall of the GO acting as nucleation agent. The results also indicate that the synthesis method is repeatable.

Table 4-1: DSC results of the Paraffin Wax and PCM1–PCM4.

Sample name	paraffin (wt %)	Melting			Solidification		
		$T_{t,m}$(℃)	T_m(℃)	ΔH_m(kJ/kg)	$T_{t,f}$(℃)	T_f(℃)	ΔH_f(kJ/kg)
PCM 1	47.80	33.7	54.60	63.11	29.57	44.78	64.45
PCM 2	47.39	31.87	51.48	62.53	29.13	45.76	63.34
PCM 3	44.81	32.15	52.33	59.12	28.56	44.63	60.73
PCM 4	48.30	35.68	53.57	63.76	31.04	44.59	64.89
Paraffin Wax	100	33.84	53.46	131.92	30.34	42.25	132.31

$T_{t,m}$: Melting transition temperature — $T_{t,f}$: Freezing transition temperature

T_m : Melting temperature — T_f : Freezing temperature

ΔH_m: Melting latent heat — ΔH_f: Freezing latent heat

4.2.2.4 Thermal stability

The TGA curves of paraffin and PCM composites are shown in Figure 4-7 . The results show that there are two steps of weight loss for composite PCMs and the weight loss of PCM4 is larger than other PCMs due to the higher mass percentage of paraffin wax. As shown in Figure 4-7, the first step occurs at a temperature between 250 and 350℃

and belongs to the thermal degradation of the paraffin wax molecular chains while the second step occurs at a temperature higher than 350℃ due to the thermal degradation of the GO. A supporting GO layer creates a physical protective wall on the surface of the composite PCM, delaying the decomposition of paraffin. This protective wall can restrict the transfer of flammable molecules to the gas phase and the transfer of heat from the flame to the condensed phase (Zhang et al., 2009). This result indicates that the GO composite can improve the thermal stability of the composite PCMs.

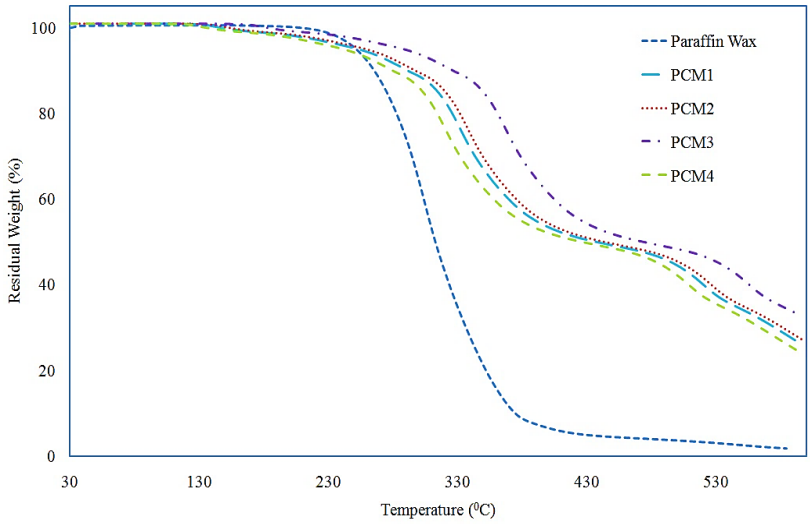

Figure 4-7: TGA curves of the paraffin wax and PCM1–PCM 4.

4.2.2.5 Thermal reliability

The main issue in thermal energy storage materials is the stability of the thermal and chemical properties after a long term utility period. Therefore, thermal cycling test was performed to investigate the properties of composite PCM after a large number of melting and freezing cycles. Thermal cycling test was done up to 2500 cycles and DSC analysis were performed for PCM 4 after 500, 1500 and 2500 cycles. Results are shown in Figure 4-8 and Figure 4-9 .

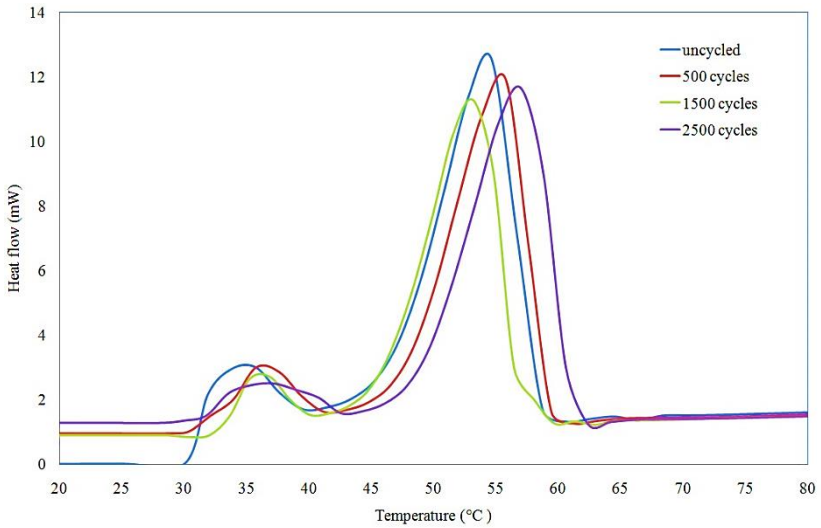

Figure 4-8: Melting DSC curves of the SSPCM before and after thermal cycling

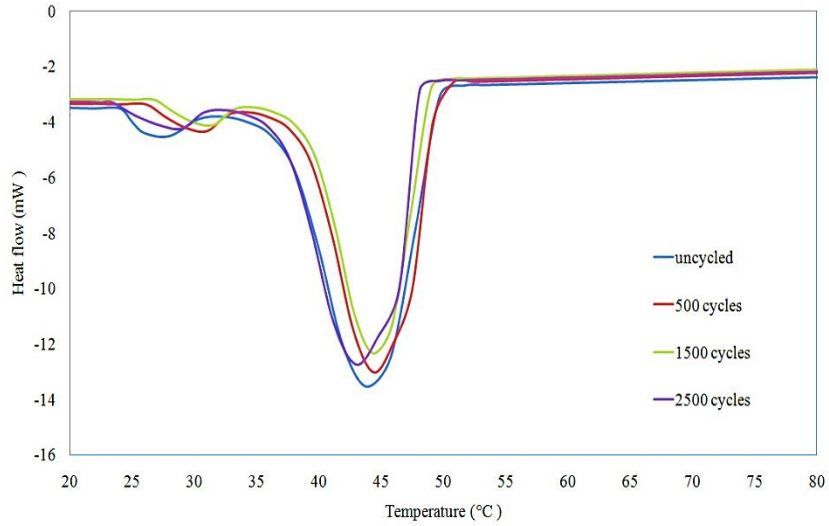

Figure 4-9: Solidifying DSC curves of the composite PCM before and after thermal cycling

Thermal properties of composite PCM before and after thermal cycling are given in Table 4-2. After thermal cycling, the melting temperature after 500, 1500 and 2500 cycles changed as 1.08,-0.18 and 1.85℃ and freezing temperature changed by 2.04,1.11 and -0.04 ℃ , respectively. The latent heat values of composite PCM are changed by -3.10, 4.03 and 1.73% for melting process and 3.42, 4.81 and 2.74 % for freezing process

after 500, 1500 and 2500 cycles. The changes in melting and freezing temperature of composite PCM are not significant for LHTES applications and it can be considered that PCM composite shows good thermal reliability after big number of thermal cycles. The decrease in latent heat values are in acceptable level for LHTES applications for composite PCM (Chen et al., 2012).

Table 4-2: Thermal properties of paraffin/GO composite PCM before and after thermal cycling

Cycling number	Melting temperature(℃)	Melting latent heat (kJ/kg)	Freezing temperature(℃)	Freezing latent heat (kJ/kg)
0	53.57	63.76	44.59	64.89
500	54.65	61.78	46.63	62.67
1500	53.39	61.19	45.7	61.76
2500	55.42	62.67	44.55	63.11

In addition, Figure 4-10 shows the FT-IR spectra of composite PCM before and after thermal cycling. It can be seen that there are no changes in the shape and frequency values of major peaks after thermal cycling. This result shows that after a high number of repeated melting/freezing cycles the chemical formation of the composite was not affected.

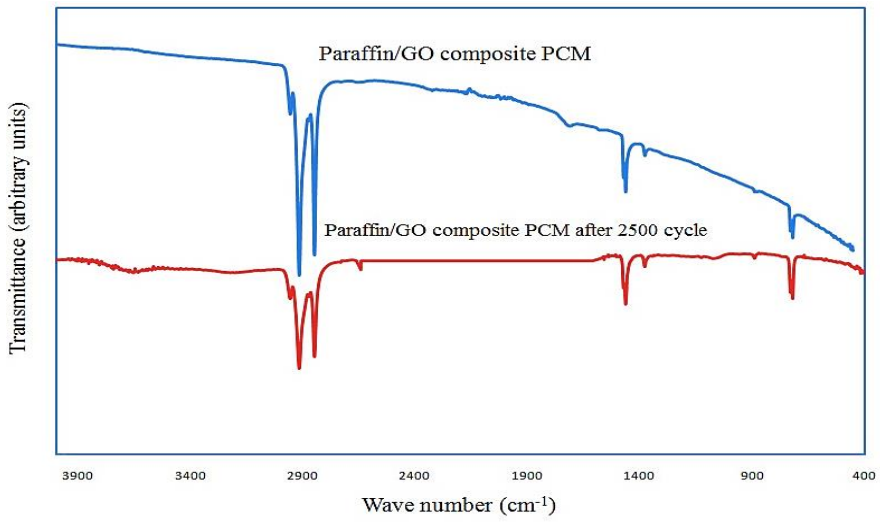

Figure 4-10: FT-IR spectra of paraffin/GO composite PCM before and after thermal cycling

4.2.2.6 Thermal conductivity of paraffin/GO SSPCMs

Thermal conductivity of composite PCM is an important parameter besides heat storage and release performances. The thermal conductivity of pure paraffin and composite PCMs was measured by a thermal conductivity apparatus (KD-2 Pro) by using the hot wire method. Thermal conductivity of composite PCMs was measured in solid state before melting temperature and after melting temperature of paraffin in thermal equilibrium condition. The results are presented in Table 4-3 for pure paraffin and PCM1 –PCM4. As shown in Table 4-3 in solid state (25 ℃) and molten state (60 ℃) the thermal conductivity of paraffin/GO composite is much higher than that of paraffin wax. The thermal conductivity of the PCM 1, PCM 2, PCM 3 and PCM4 is 1.04, 1.19, 1.45 and 0.985 W/m.K in the melting state and 0.952, 0.964, 1.32 and 0.932 W/m.K in solidifying state, respectively. The thermal conductivity of the PCM4 in both solid (25 ℃) and molten (60 ℃) states is highly increased by more than three times compared to paraffin wax thermal conductivity. The PCM 4 is presented as a suitable composite PCM for thermal energy storage due to the higher heat transfer rate and greater thermal conductivity

Table 4-3: Thermal conductivity of the paraffin wax, PCM1–PCM4 in melting and solidifying states

Sample name	Thermal conductivity (W/m K)	
	Molten state (60 ℃)	Solid state(25 ℃)
Paraffin wax	0.305	0.287
PCM 1	1.04	0.952
PCM 2	1.19	0.964
PCM 3	1.45	1.32
PCM 4	0.985	0.932

4.2.3 Palmitic acid /Graphene Oxide SSPCM

GO has high thermal conductivity, high chemical durability and environmental resistance. In the present study, we used the palmitic acid as a fatty acid to prepare form-stable PCM with high thermal conductivity. In this section we have studied the effect of GO on structure and thermal properties of the PA.

4.2.3.1 FTIR spectra of the PA/GO SSPCM

FT-IR spectroscopy was done for characterization of composite PCM to investigate chemical compatibility between PA and GO. Figure 4-11 shows the FT-IR results for PA (palmitic acid) and PA/GO composite PCM. The peaks at 2915.02 and 2853.57 cm^{-1} are the symmetrical stretching vibration peaks of – CH_2 in PA. The absorption peak at 1720 cm^{-1} is assigned to the C═O stretching vibration. The peak at 1321 cm^{-1}corresponds to the in-plane bending vibration of the –OH group of palmitic acid. The peak at 910 cm^{-1}corresponds to the out-of-plane bending vibration of the –OH functional group and the peak at 730 cm^{-1}represents the in-plane swinging vibration of the –OH functional group. It can be clearly seen from both FT-IR spectrum, there is no

shift in the above main absorption peaks and in composite PCM can clearly indicate PA absorption peaks. This result shows that there is no chemical reaction between functional groups of PA and GO.

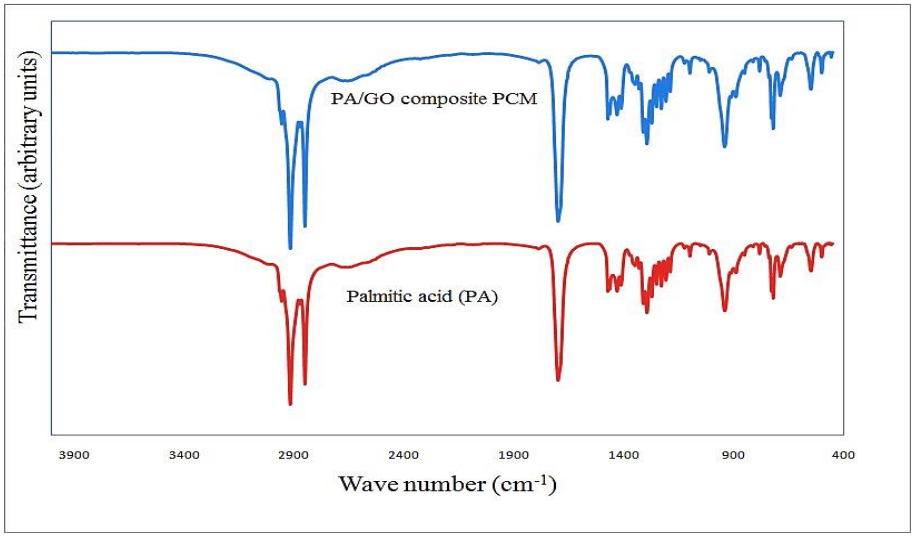

Figure 4-11: FT-IR spectra of PA and form-stable PA/GO composite PCM

4.2.3.2 XRD patterns of PA/GO composites PCM

Figure 4-12 shows the XRD patterns of the graphene oxide (GO), PA and GO/PA composite PCM. Figure 4-12(a) shows that GO has peaks at angle of 14° and 43° as observed in Li et al. (2010). Figure 4-12(b) shows the XRD peaks at angles of 8°,13°, 24°, 25° and 27.0° contributed by the PA because of its given crystallization. Figure 4-12(c) indicates that the XRD peaks of the PA in the composites PCM are also stated on the basis of the GO major peaks and it shows that the crystal formation of the PA in the composites PCM did not change during the impregnation process. The intensity of the X-ray peaks of the PA in the GO composites is lower than that of pure PA. This result shows that due to the limitation of the crystals of the PA by pores of the GO composite, the crystallite size of the PA becomes smaller in the composites.

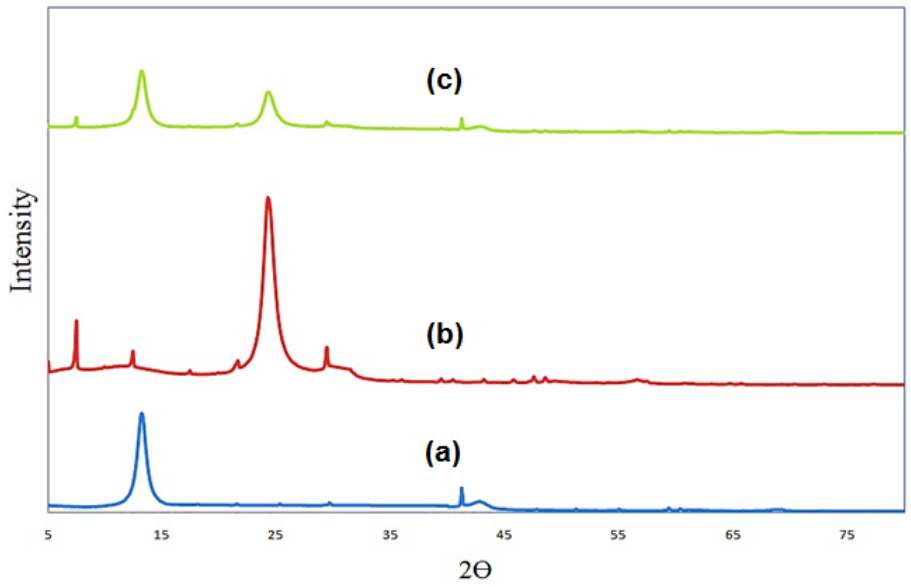

Figure 4-12: XRD patterns of the (a) graphene oxide (GO) (b) PA (c) GO/PA composite PCM

4.2.3.3 Microstructure Analysis

Figure 4-13 shows the SEM images of the PA/GO composite PCM. In Figure 4-13, the black and white parts are the PA and GO substances within the composite PCMs, respectively. It was observed how the PA distributed into the pores of GO sheet used as the supporting material. The composite material retains its form without having leakage of the melted PA during phase change procedure.

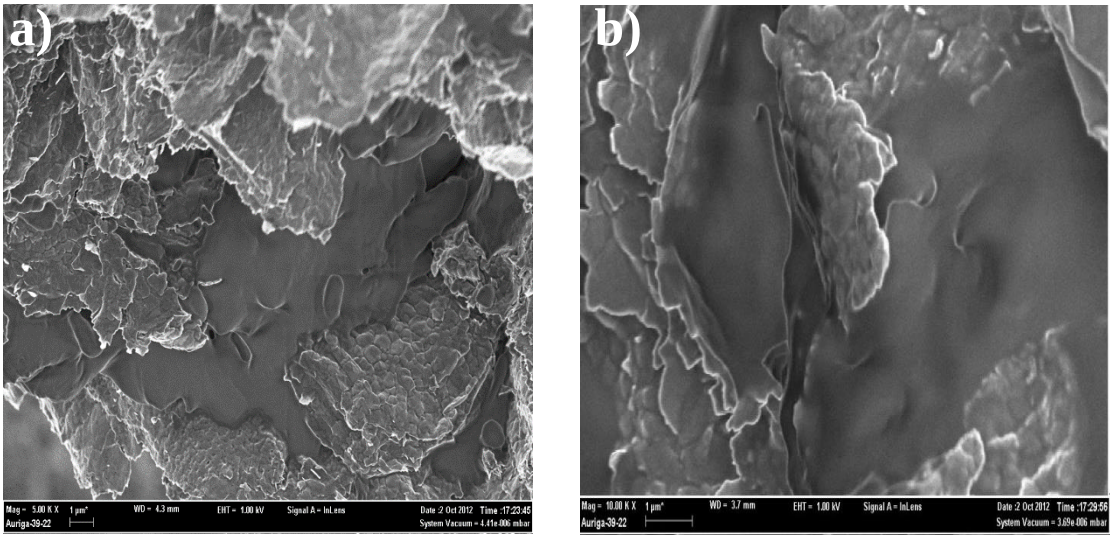

Figure 4-13: SEM micrographs of the PA/GO composite PCM (a)(x 5K).(b)(x10K)

4.2.3.4 Phase Change Properties of the PA/GO SSPCMs

DSC analyses results are shown in Figure 4-14 andFigure 4-15 for the PA, PCM1, PCM2, PCM3 and PCM4. The melting and freezing temperatures and latent heats are summarized in Table 4-4. As shown in Table 4-4, the melting and solidifying temperatures are 61.14°C and 59.84°C for the PA and 59.83°C and 60.05°C for the PCM 2, respectively.

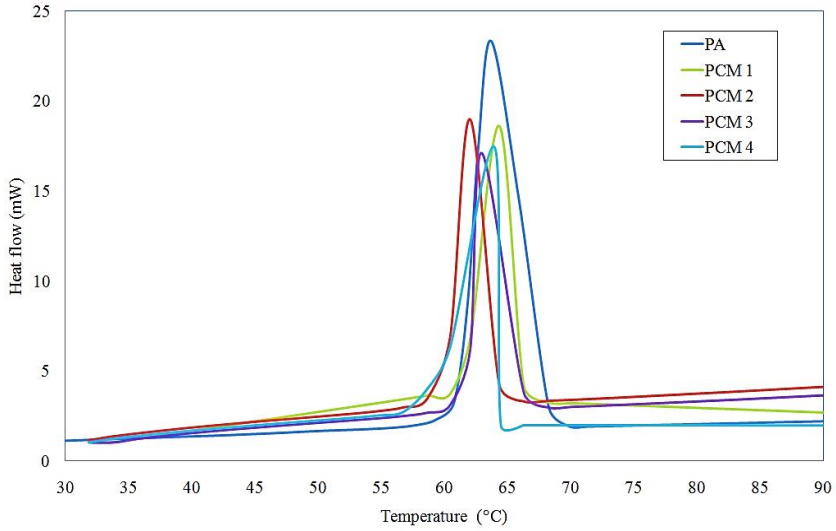

Figure 4-14: Melting DSC curves of the PA and PCM1–PCM4.

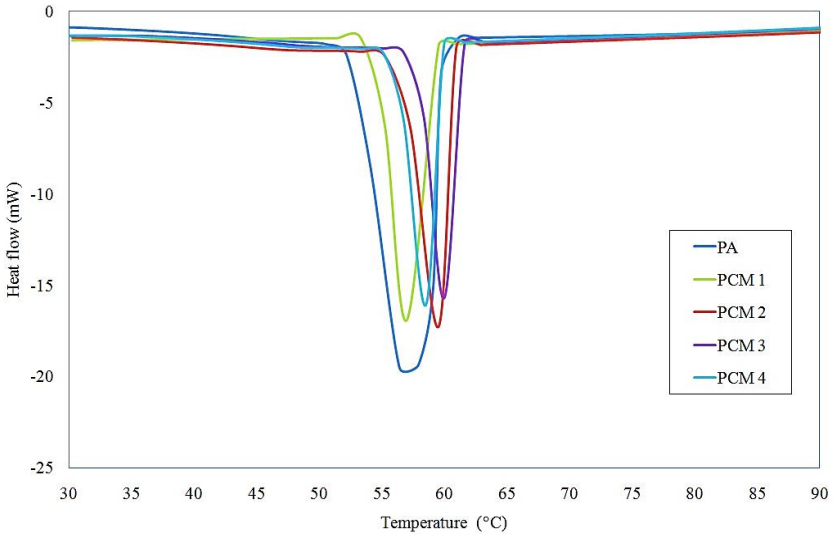

Figure 4-15: Solidifying DSC curves of the PA and PCM1–PCM4.

The melting and solidifying latent heats are measured to be 202.00kJ/kg and 208.87kJ/kg for the PA and 101.23kJ/kg and 101.49kJ/kg for the PCM 2, respectively. In

the composites, during the melting and solidifying process, only PA absorbs and releases thermal energy so high latent heat storage capacity in composite PCM is the result of high phase change material content. The mass percentage of PCM was calculated according to Equation (4-1). Hence, the PCM mass percentages of PCM 1, PCM 2, PCM 3 and PCM 4 were 49.78 wt%, 50.11 wt%, 49.39 wt% and 40.60 wt%, respectively. The highest mass percentage of PA in GO sheets was determined to be 50.11 wt% for PCM 2 that melts at 60.45℃ with a latent heat of 101.23kJ/kg and solidifies at 60.05℃ with a latent heat of 101.49kJ/kg. The differences between melting and solidifying temperatures of PA and PCM composites (Table 4-4) shows that the supercooling degree of composite PCMs is smaller than PA during solidification process. These results show that GO as supporting material protecting PA due to the porous wall of the GO acting as nucleation agent. The results also indicate that the synthesis method is repeatable.

Table 4-4: DSC results of the PA and PCM1–PCM4.

Sample name	Melting		Solidification	
	Temperature (^{0}C)	Latent heat (kJ/kg)	Temperature (^{0}C)	Latent heat (kJ/kg)
PA	61.14	202.00	59.84	208.87
PCM 1	61.25	100.56	58.21	101.05
PCM 2	60.45	101.23	60.05	101.49
PCM 3	61.05	99.78	60.15	100.07
PCM 4	59.65	100.21	58.45	100.67

4.2.3.5 Thermal stability

The TGA and DTG curves of PA and PCM 2 are shown in Figure 4-16 and Figure 4-17, respectively. The result shows that there are two steps of weight loss for

PCM 2. As shown in Figure 4-16, the first step occured at temperature between 230 and 310℃ that belongs to the thermal degradation of the PA molecular chains while second step occured after 430℃ as for the thermal degradation of the GO. Charred residue amount of PA and PCM2 at 600 ℃ was determined to be 1 and 26.36 % and also the temperature of maximum weight loss was measured to be 280 and 287℃, respectively. A protective GO layers create a physical protective wall on the surface of composite PCM, delaying the main decomposition of PA. This protective wall can confine the transfer of flammable molecules to the gas phase and the transfer of heat from the flame to the condensed phase (Zhang et al., 2009).This result indicates that the GO composite can improve the thermal stability of the composite PCMs.

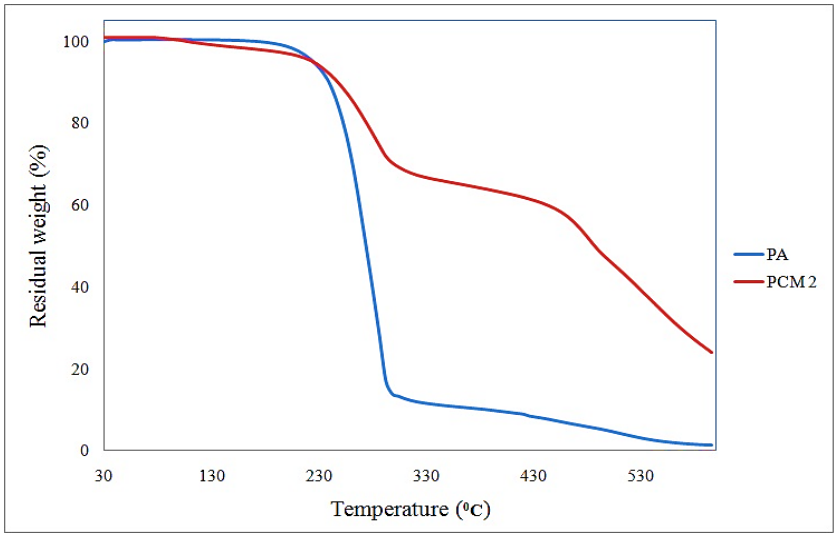

Figure 4-16: TGA curves of the PA and PCM2

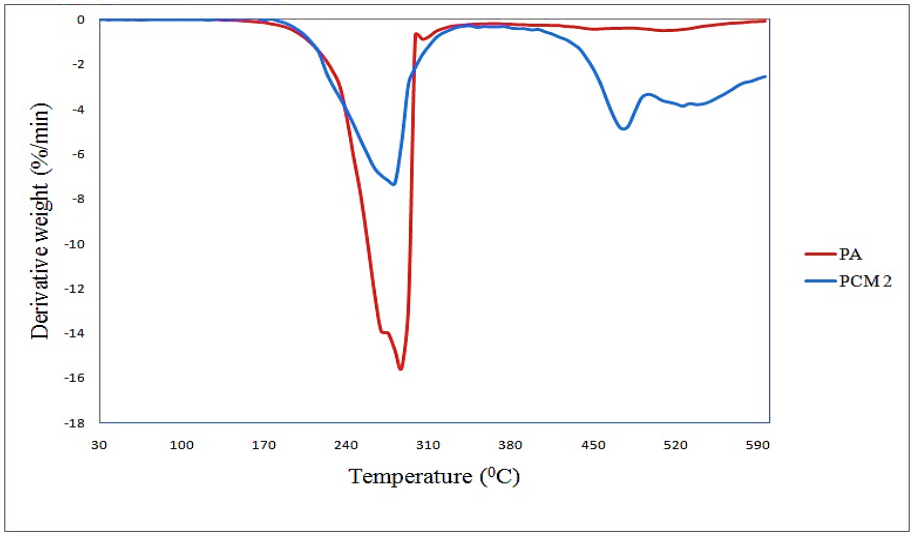

Figure 4-17: DTG curves of the PA and PCM 2

4.2.3.6 Thermal Reliability

Thermal cycling test was performed to investigate properties of composite PCM after a large number of melting and freezing cycles. Thermal cycling test was done up to 2500 cycles and DSC analysis was performed for PCM 2 after 500, 1500 and 2500 cycles. Results are shown in Figure 4-18 and Figure 4-19 .

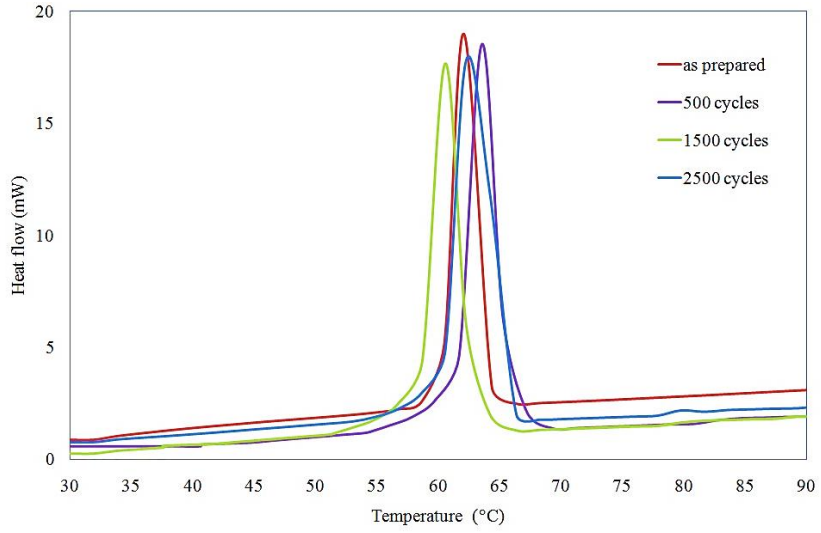

Figure 4-18: Melting DSC curves before and after thermal cycling

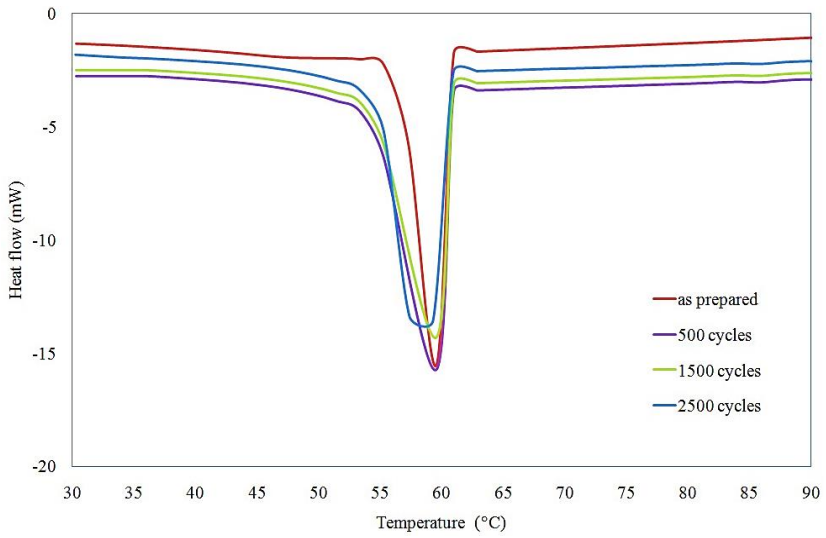

Figure 4-19: Solidifying DSC curves before and after thermal cycling

Thermal properties of composite PCM before and after thermal cycling are given in Table 4-5. After thermal cycling, the melting temperature after 500, 1500 and 2500 cycles changed by 0.18,-0.48 and -0.42 ℃ and freezing temperature changed by -0.38,-0.32 and -0.63℃ , respectively. The latent heat values of composite PCM were changed by 0.52 %, 1.09 % and -1 % for melting process and -1.04 %,-1.59% and -1.39 % for freezing process after 500, 1500 and 2500 cycles. The changes in melting and freezing temperatures of composite PCM are not significant for LHTES applications. The decrease in latent heat values is in an acceptable level for LHTES applications for composite PCM (Fernandes et al., 2012).

Table 4-5: Thermal properties of PA/GO SSPCMs before and after thermal cycling

Cycling number	Melting temperature(°C)	Melting latent heat (kJ/kg)	Freezing temperature(°C)	Freezing latent heat (kJ/kg)
0	59.83	101.23	60.05	101.49
500	60.50	101.76	60.12	100.43
1500	58.63	102.34	60.15	99.87
2500	59.67	100.21	60.03	100.08

In addition, Figure 4-20 shows the FT-IR spectra of PCM 2 before and after 2500 thermal cycles. Figure 4-20 shows that there are no essential changes in the form and wave number of main peaks after thermal cycling. These results prove that chemical structure of PA/GO composite PCM was not affected during thermal cycling. Accordingly, the form-stable PA/GO composite PCM is stable in chemical and thermal properties after 2500 thermal cycles.

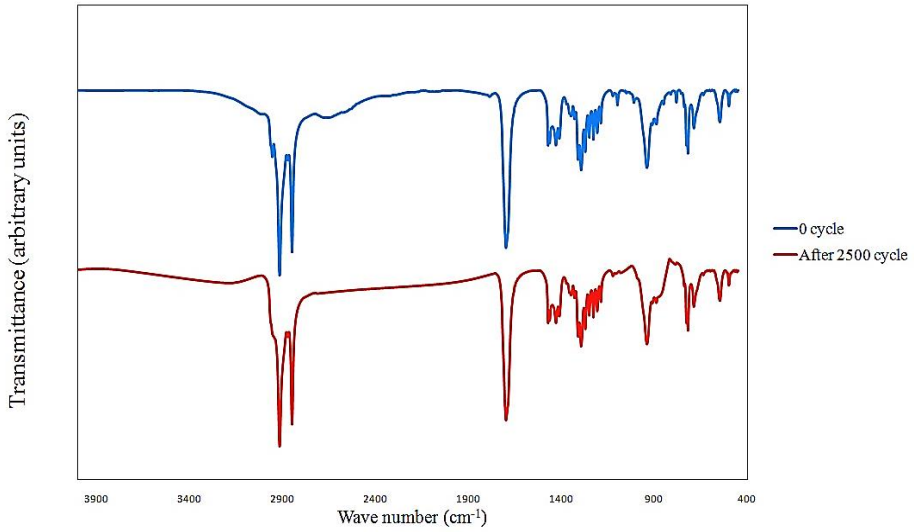

Figure 4-20: FT-IR spectra of PA/GO composite PCM before and after thermal cycling

4.2.3.7 Thermal Conductivity

The thermal conductivity of PA and composite PCMs was measured by a thermal conductivity apparatus (KD-2 Pro) by using the hot wire method. Thermal conductivity of composite PCMs was measured in solid state before and after melting temperature of PA in thermal equilibrium condition. The results are presented in Table 4-6 for PA and PCM1 –PCM4. As shown in Table 4-6 in solid state (25 ^{0}C) and molten state (60 ^{0}C) the thermal conductivity of PA/GO composites is much higher than PA. The thermal conductivity of the PCM 1, PCM 2, PCM 3 and PCM4 is 1.13 W/m K, 1.08 W/m K, 1.38 W/m K and 1.45 W/m K in the molten state and 1.08 W/m K, 1.02 W/m K, 1.20 W/m K and 1.24 W/m K in solid state, respectively. From the results, it can prove that the thermal

conductivity of the PCM2 in both regions of molten and solid was increased by more than three times compared to the PA thermal conductivity.

Table 4-6: Thermal conductivity of the PA and PCM1–PCM4

Sample name	Thermal conductivity (W/m K)	
	molten state (60 ^{0}C)	Solid state(25 ^{0}C)
PA	0.29	0.285
PCM 1	1.13	1.08
PCM 2	1.08	1.02
PCM 3	1.38	1.20
PCM 4	1.45	1.24

The improvement of thermal conductivity in PA/GO composite PCM also verified by comparison of the melting and freezing time of PA and PA/GO composite PCM. The melting and freezing graphs of PA and PCM 2 are shown in Figure 4-21 and Figure 4-22. As can be seen in Figure 4-21 the melting time will be 38 min for pure PA and 23 min for PCM 2 and it shows that the melting time was reduced by 39.4%. Figure 4-22 shown that the freezing time were also decreased by 60.6% from 33 min for pure PA to 13 min for PCM 2. This result also indicates that the thermal conductivity in composite PCM was obviously increased and heat transfer in composite was more intensive.

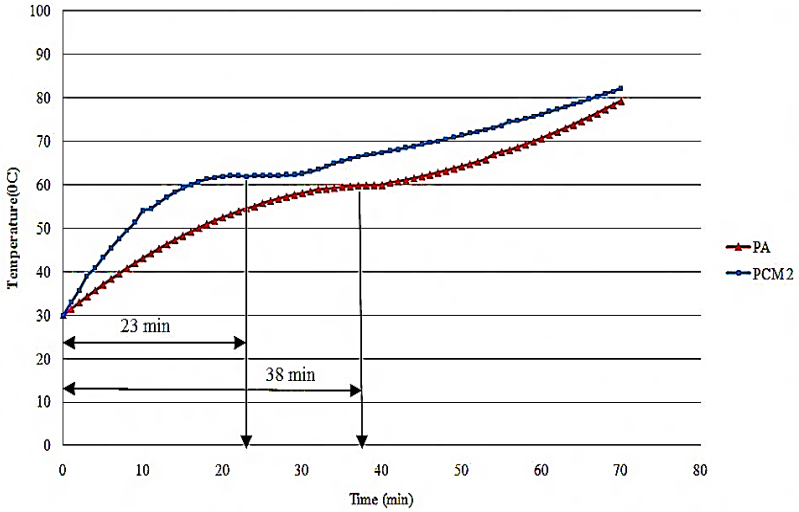

Figure 4-21: Temperature vs time graph of PA and PCM 2 for melting process

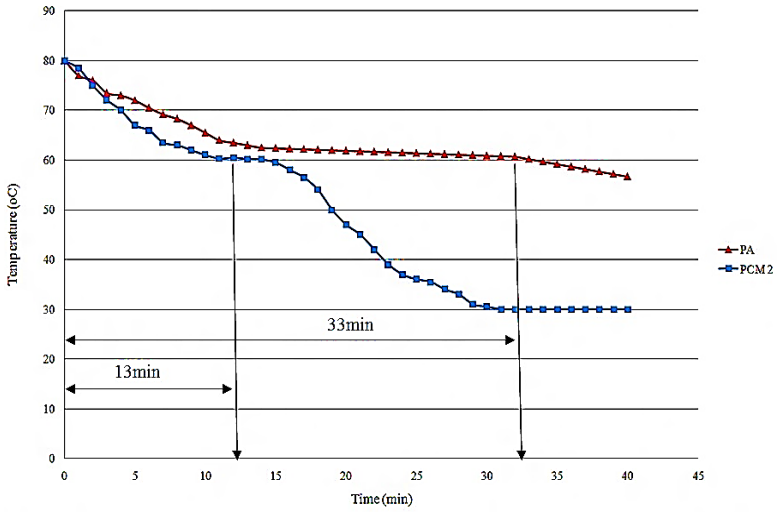

Figure 4-22: Temperature vs time graph of PA and PCM 2 for solidification process

4.3 Nitrogen Doped Graphene (NDG) SSPCM

In this work, we report the preparation of PA/NDG composite PCM as a novel form-stable composite PCM by using NDG as supporting material. The high compatibility between NDG and PA leads to a large improvement in the thermal conductivity at low filler loading ratio along with a small reduction in latent heat. Furthermore, capillary forces and surface tensions were improved due to the larger specific surface area (793 m^2/g) of NDG that is effective for shape-stabilization over the phase change process of PCMs mainly because it helps to hold the molten PCM.

4.3.1 Characterization of Nitrogen Doped Graphene

Figure 4-23 (a) and (b) show the FESEM images of the sample, displaying a uniform structure like crumpled silk veil waves with a porous architecture while NDG nanosheets are randomly stacked together. The FESEM images of the NDG sample reveal that the two dimensional graphene structures with high specific surface area and volume ratio are well retained. Three major peaks located at 284.4, 399.5 and 532 eV was determined from the XPS spectra of the NDG sample (Figure 4-23 (c)) that was linked to C1s, N1s and O1s, respectively, showing the nitrogen was incorporated within the graphene structure (Guo et al., 2013). The nitrogen was doped by atomic percentage of 2.6% within the graphene network by pyridinic and pyrrolic nitrogen species, respectively. The nitrogen atoms might be positioned in a π conjugated system and contributed to the π system with one or two p-electrons, respectively (Lu et al., 2013). The specific surface area of the NDG sample was measured and shown in Figure 4-23(d). The unique mesoporous structure of NDG contributes to the high specific surface area (793 m^2/g) which is higher than prepared GO (684 m^2/g) with a uniform pore size distribution around 3–5 nm. Over the synthesis of NDG sheets, beside the carbon atoms that was replaced by nitrogen atoms (most likely located on the reactive edge) ammonia can also react with graphene to form hydrogen cyanide and hydrogen ($C + NH_3 = HCN + H_2$) (Panchakarla et al., 2009). This reaction takes some carbon that will make the NDG sheets more porous, which in turn resulted in the higher specific surface area, pore volume, and pore size. The large surface area can enhance both the heat transfer rate and the adsorption quantity of PA.

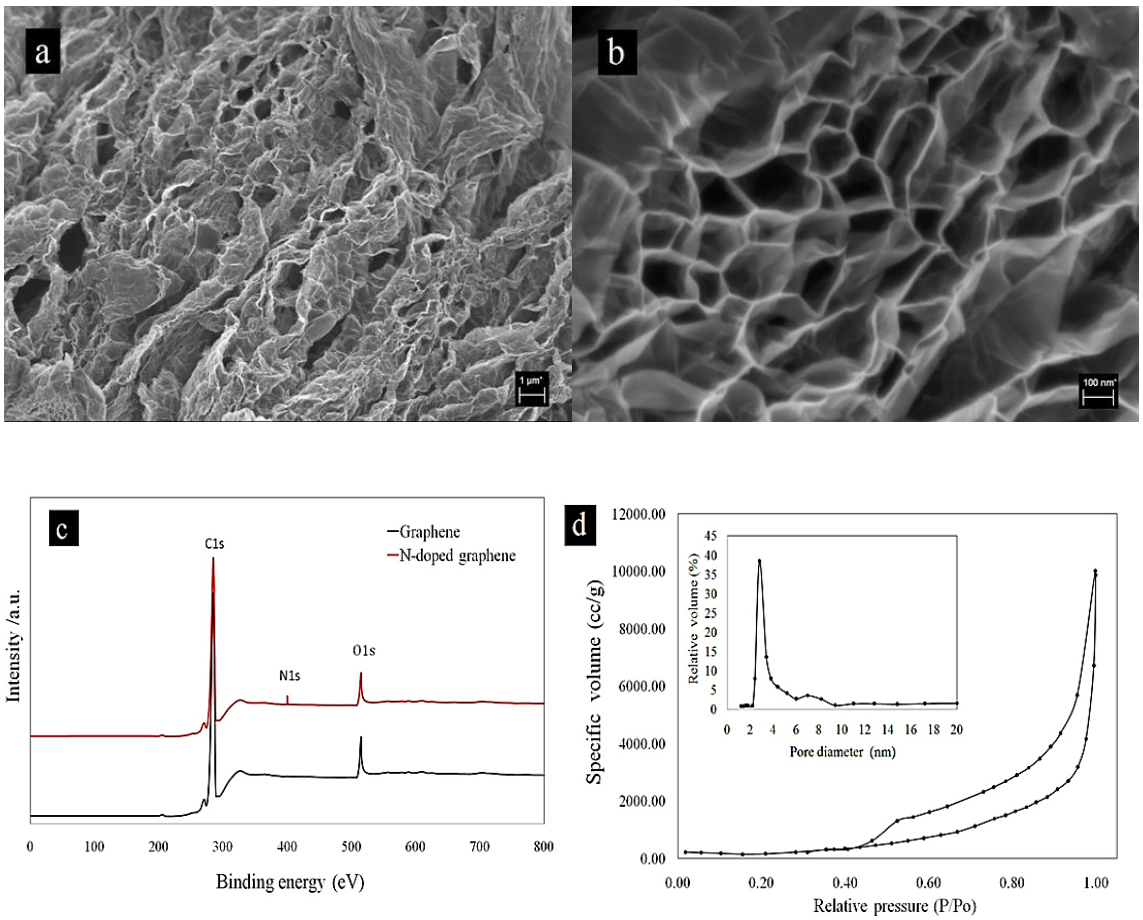

Figure 4-23: (a and b) FESEM images of NDG (×5K, ×60K); (c) XPS spectra of NDG and graphene; (d) Nitrogen adsorption/desorption isotherms of NDG. Inset in (d) is the BJH pore size distribution

4.3.2 Morphology of the PA/NDG SSPCM

The FESEM images of the form-stable PCMs with varying NDG content are shown in Figure 4-24. The NDG particles are generally embedded in the PA as indicated by the white parts protruding from the background or lying on the surface and suggested by their irregular but sharp edges in contrast with the smooth and soft PA. At the lower nanofiller loading, the NDG particles in the nanocomposites are easier to recognize because of their particular structure as shown in Figure 4-24 (a) and (b). The NDG particles in PA composites preserved their structure while the PA was adsorbed completely by the surface and pores of NDG.

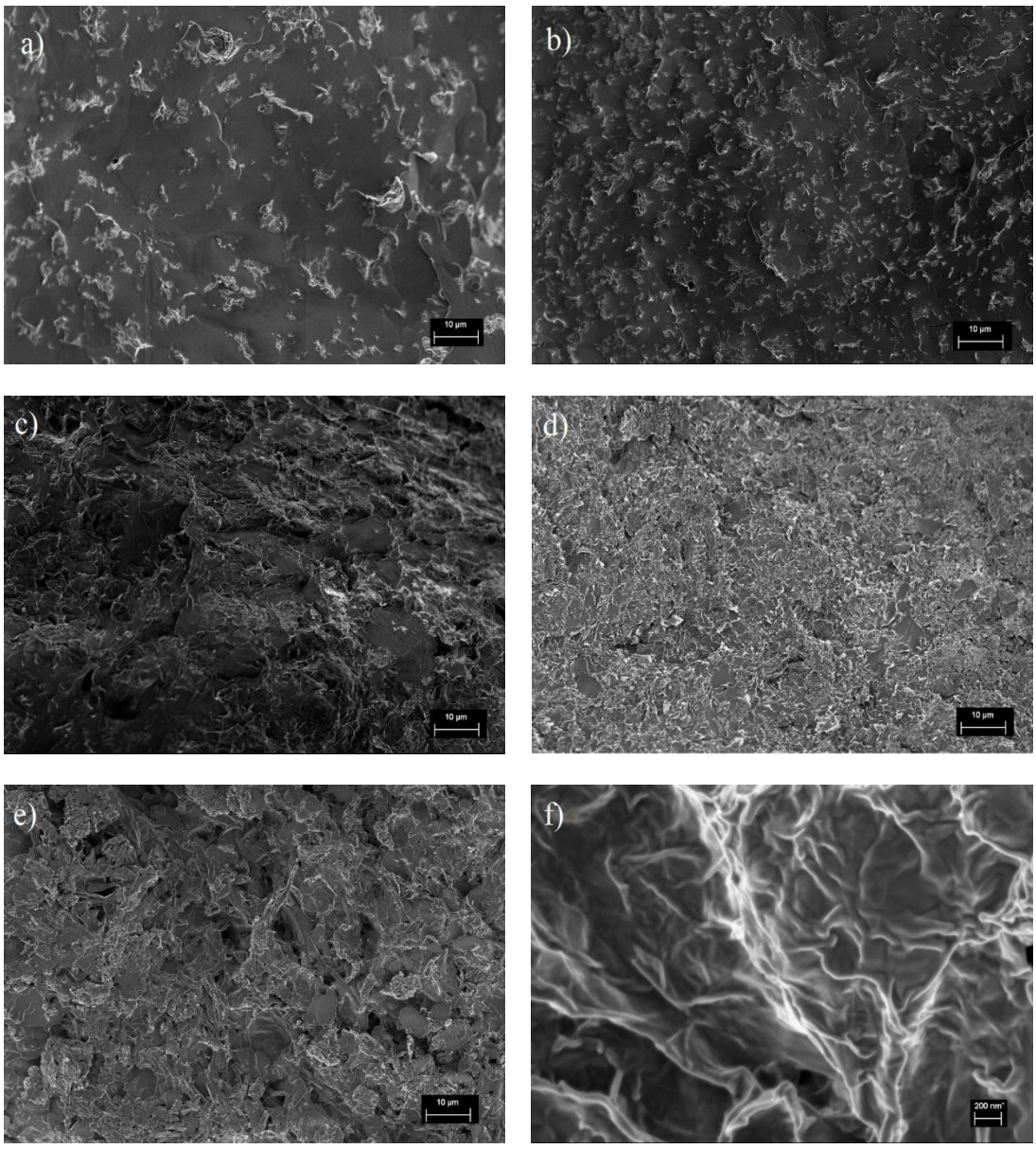

Figure 4-24: FESEM images of (a) S1 (b) S2 (c) S3 (d) S4 (e) S5 (f) S5 (×25K)

Figure 4-24: (c), (d) and (e) show nearly only white areas, suggesting that the PA was adsorbed well into the NDG network. It can be clearly observed in Figure 4-24(f) that NDG layers possess the substantial capability to absorb the melted PA once the temperature is higher than the melting point of PA. Besides, the NDG particles develop a network which could avoid the composite PCM from falling apart even when the PA is melted. Therefore, the composite PCM still demonstrates the exact property of form-stability. In fact, in our experiments, the composite PCM has not been collapsed even when the PA loading was 97%.

Figure 4-25 displays the TEM images of NDG along with the PA/NDG composite PCM. The TEM image shows that NDG sheets are randomly compact and stacked together, demonstrating uniform laminar morphology like crumpled silk veil waves. The partial lining level of the PA/NDG composite (Figure 4-25(b)) is deeper compared to the NDG. That is attributable to the PA adsorbed by the network structure of NDG. The outcomes from TEM images are similar to the results from the SEM images.

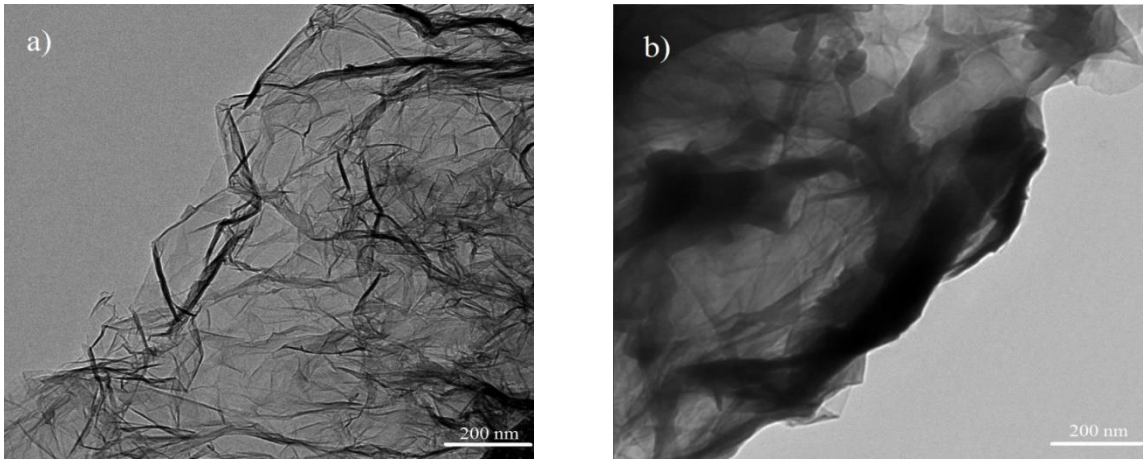

Figure 4-25: TEM images of (a) NDG (b) PA/NDG composite PCM

4.3.3 Shape-Stabilization Tests

The majority of the PCMs which have been employed in applications have numerous advantages such as high latent heat and minimal costs but they might need storage containers. The thermal efficiency of the systems will be affected by utilizing storage containers while the leakage issues also will appear in energy storage systems. Shape stabilization of PCMs will resolve these issues and may even change the thermal conductivity of the PCMs based on the additives used. Figure 4-26 shows different structures of PA/NDG composite PCMs after drying and it can be clearly seen that the PA was totally absorbed by NDG particles for higher mass percentage of NDG. The continuous solid shape of the PA was observed in mass percentage of 1 and 2%, while in other sample this shape was totally changed due to the absorption of PA by NDG particles.

Figure 4-26: Dried PA/NDG Composite PCMs

The results of the dropping tests are presented in Table 4-7.

Table 4-7: Dropping points of PA and PA/NDG composite PCMs

Sample	Dropping point (℃)
PA	65.03
S1	77.40
S2	142.20
S3	195.60
S4	>375.00[b]
S5	>375.00[b]

[b] The upper limit of the measuring range is at 375℃

The dropping point of pure PA was 65.03℃ and increased significantly with the addition of NDG particles. The capillary and surface tension forces between PA and NDG may result in a great enhancement in the shape stabilization of composite PCMs. It can be mentioned that even at a NDG content of 2 wt%, the shape of the composite can be preserved up to 142.2 ℃, considerably more than the normal operating temperature range of energy storage systems. The dropping test was corroborated by putting the prepared PA/NDG pellets into the oven at 150℃ for 1h. Figure 4-27 shows the effect of temperature on the shape of composite PCMs and it can be seen that leakage of PA occurred for S1 and S2 while there was no leakage for other samples and shape of pellets was remained.

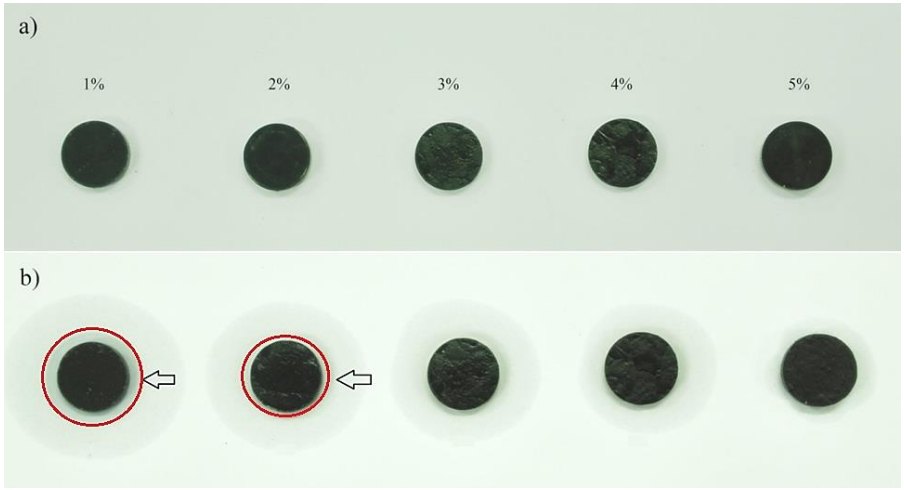

Figure 4-27: Images of PA/NDG composite PCMs (a) 30℃ (b) 150℃

4.3.4 XRD Characterization

Figure 4-28 displays the XRD patterns of pure PA, NDG and PA/NDG composite PCM samples. A wide peak centered at around 24.2° is observed for the NDG sample, confirming the recovery of a graphitic crystal structure(Wang et al., 2010). The XRD pattern of the PA/NDG composite PCM mostly indicates the features of the PA due to the strong diffraction intensity of crystalline PA. The diffraction peaks of NDG at angle of 2θ=24.2° was covered by PA as a result of the higher loading of PA. The XRD patterns from the composite PCMs generally show that the crystal formation of PA within the composite PCMs is not different than in pure PA.

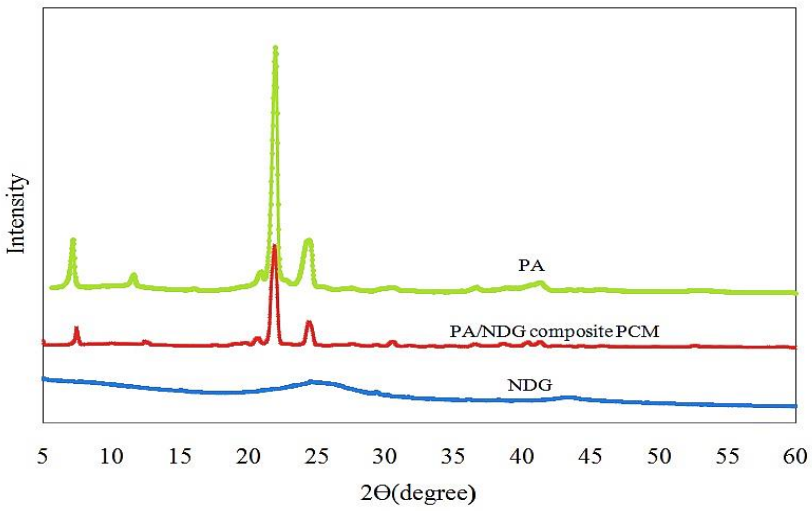

Figure 4-28: XRD patterns of NDG, pure PA and PA/NDG composite PCM

4.3.5 Thermal Energy Storage Properties

Thermal energy storage properties of pure PA and prepared PA/NDG composite PCMs were studied with DSC and summarized in Table 4-8. For each sample, four different parts of the pellet were taken to achieve accurate results and the relative standard deviation (RSD) was also calculated. All DSC curves in Figure 4-29 exhibited one big endothermic peak with T_{peak} located in the temperature range of 64–67 ℃, which is ascribed to the melting of PA. In other words, it is PA that performs the role of storing thermal energy. The DSC curves shown in Figure 4-29 and the data listed in Table 4-8 indicate that the thermal energy storage properties of the prepared form-stable PCMs are not affected by using NDG as a supporting material.

Table 4-8: Thermal energy storage properties of PA and PA/NDG composite PCMs

Samples	Melting temperature T_m(℃)	Melting peak Temperature T_p(℃)	Phase change latent heat(ΔH_m)			Relative standard deviation (%)
			Experimental value (kJ/kg)	Calculated value (kJ/kg)*	Relative Error (%)	
Pure PA	62.40	64.12	206.32	-----	------	0.63
S1	63.27	65.13	199.65	204.25	2.25	0.58
S2	63.36	65.89	198.84	202.19	1.65	0.67
S3	63.78	65.99	199.48	200.13	0.32	0.73
S4	63.85	66.44	197.53	198.06	0.26	0.76
S5	63.89	66.52	195.54	196.00	0.23	0.85

* Calculated by : $\Delta H_{composite}$ =(1-NDG (wt%))* ΔH_{PA}

The T_m of composite PCMs were increased slightly with increasing of NDG content. NDG can play a role in promoting the heterogeneously nucleated phase transition from melting to a triclinic phase and consequently enhances its crystallization temperature. In addition, the relative error between theoretical and experimental latent heat values of composites were decreased with increasing of the mass percentage of NDG

in the prepared composites. This was indicated that the molten PA was adsorbed properly by the NDG nano sheets network. In addition, the NDG nano sheets with high and uniform porous structure was capable to minimize seepage of the molten PA that will improve the latent heat of the PA/NDG composite PCMs. Here the S3 sample, which contained 3 wt% of NDG with the relative error of less than 1%, gave the highest latent heat value without any leakage, which was 96.9% of that of pure PA.

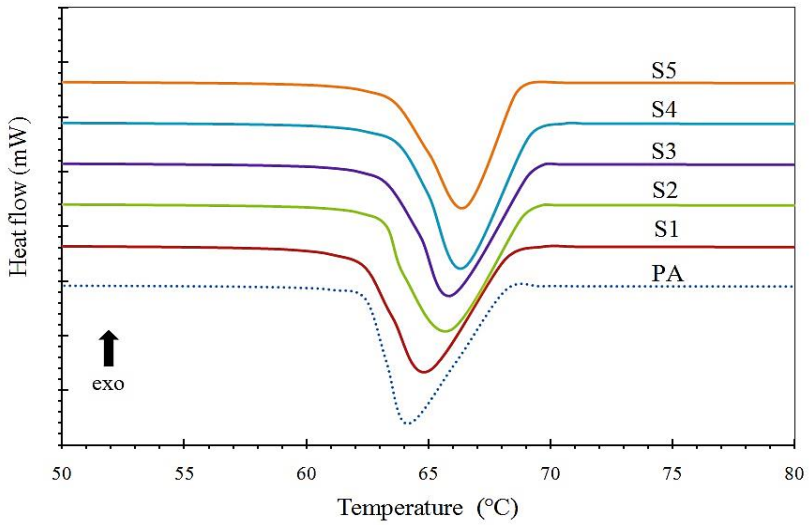

Figure 4-29: DSC curves of pure PA and PA/NDG composite PCMs

Latent heat is particularly attractive due to its ability to provide high-energy storage density in quasi-isothermal process. The energy storage density could be increased by using PCM having a high phase change (latent heat) within the temperature range of the storage while the total heat stored in a PCM can be calculated as follows:

$$Q_t = \int_{T_1}^{T_m} C_{ps} \, . \, dT + \Delta H_L + \int_{T_m}^{T_2} C_{pl} \, . \, dT \qquad (4\text{-}2)$$

Here Q_t is the total heat stored, C_{ps} and C_{pl} are the specific heat of solid and liquid PCM, respectively. ΔH_L is the heat of fusion at the phase change temperature T_m.It can be seen that the specific heat also affects the total heat storage while its change with temperature are generally not. The specific heat of pure PA and PA/NDG composite PCM was

measured with the multiple curves method in temperatures between 35 to 50 ℃ as shown in Figure 4-30.

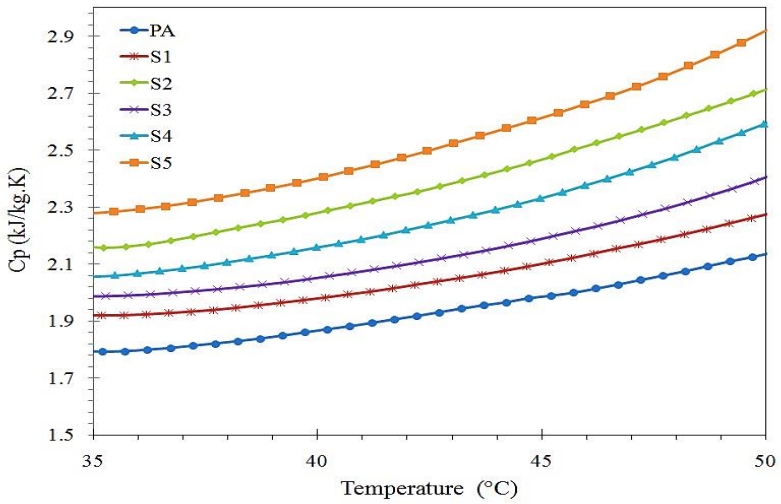

Figure 4-30: Specific heat curves of PA and composite PCMs

The results show that the specific heats of composite PCMs were increased by adding NDG, with the increment more pronounced for higher NDG loadings. The equations are generated according to the measured data between 35 to 50 °C and they represent the temperature interval where no phase change occured. The A, B and C coefficients of the solid phase are given in Table 4-9.

Table 4-9: Coefficients of the second order polynomials in solid State,

C_p (kJ/kg °C) =AT^2 (°C) +BT (°C) +C

Sample	A	B	C	R^2
Pure PA	0.0024	-0.1862	5.4358	0.94
S1	0.0012	-0.0757	3.1324	0.99
S2	0.0015	-0.1012	3.6725	0.99
S3	0.0016	-0.103	3.6636	0.99
S4	0.0012	-0.0663	2.9727	0.99
S5	0.0018	-0.1078	3.8882	0.99

4.3.6 Thermal Stability

Thermal stability is considered as an important parameter in assessing the performance of newly designed composite PCMs when used for thermal energy storage or thermal regulation. Figure 4-31 shows the TG curves of PA and the prepared form-stable PCMs. The onset and maximum weight loss temperatures are given in Table 4-10. PA exhibits a one-step weight loss starting at 201.48 °C and the maximum weight loss temperatures at 275.16°C, which is caused by the evaporation of PA. The PA/NDG samples also show a one-stage degradation behavior while the temperatures at maximum weight loss rate are significantly increased up to 349.21 °C.

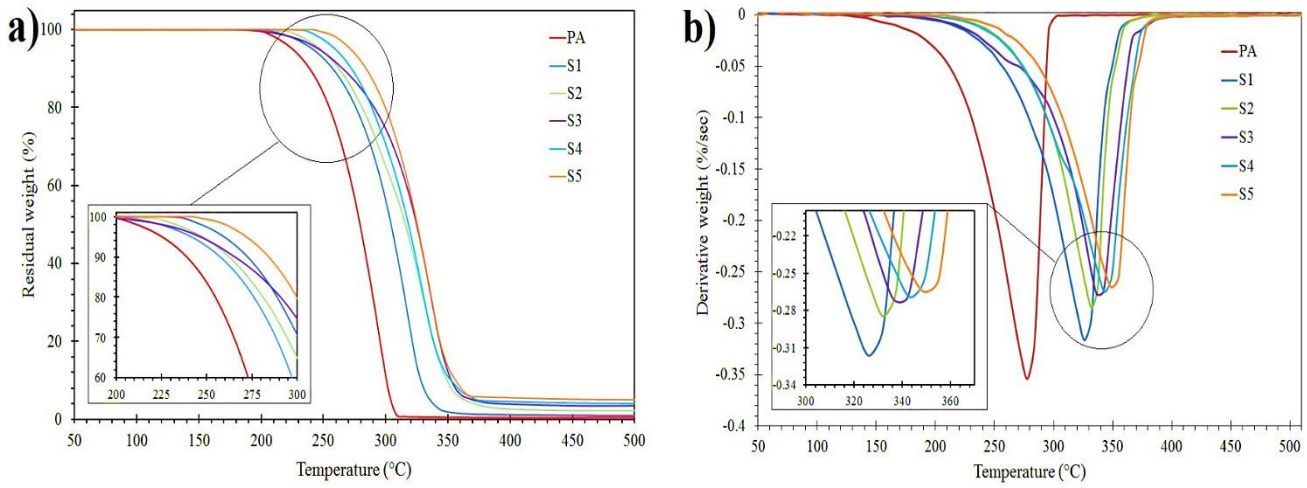

Figure 4-31: TG (a) and DTG (b) graphs of the PA and SSPCMs

It is reasonable to believe that the PA must first break through the NDG layers during the heating process and then can evaporate out of the composite. The NDG layers are compact and rigid enough to protect the absorbed PA from diffusing at the normal boiling point, thus improving the degradation temperature of composite PCMs. The derivative TG thermograms in Figure 4-31(b) also confirm that the maximum weight loss occurs at a higher temperature for the composite PCMs with a higher content of NDGs. This indicates that the thicker NDG layers are more effective in enhancing the thermal stability of composite PCMs. It is also observed from Figure 4-31(a) that the composite samples exhibit different char yields depending on the PA that was completely absorbed

by NDGs. There is no doubt that the composite PCMs achieved higher stability by adding NDGs as a supporting material.

Table 4-10: Decomposition temperatures of the PA and composite PCMs

Sample	Onset decomposition temperature (℃)	Maximum weight loss temperature (℃)
Pure PA	201.48	275.16
S1	212.93	326.31
S2	227.17	332.26
S3	230.08	339.53
S4	233.53	343.36
S5	237.69	349.21

4.3.7 Thermal conductivity

PA has a high latent heat, but a low thermal conductivity that may delay the thermal response to the storage and release of latent heat. Therefore, thermal conductivity enhancement is absolutely required when designing composite PCMs. It was expected that adding inorganic materials with a higher thermal conductivity can enhance the thermal conductivity of the resulting composite PCMs. The thermal diffusivity was measured by the laser flash method and the thermal conductivity can be calculated according to Equation (3-2). The thermal conductivity of PA and PA/NDG composite PCMs are measured at 35 ℃ and results are shown in Figure 4-32.

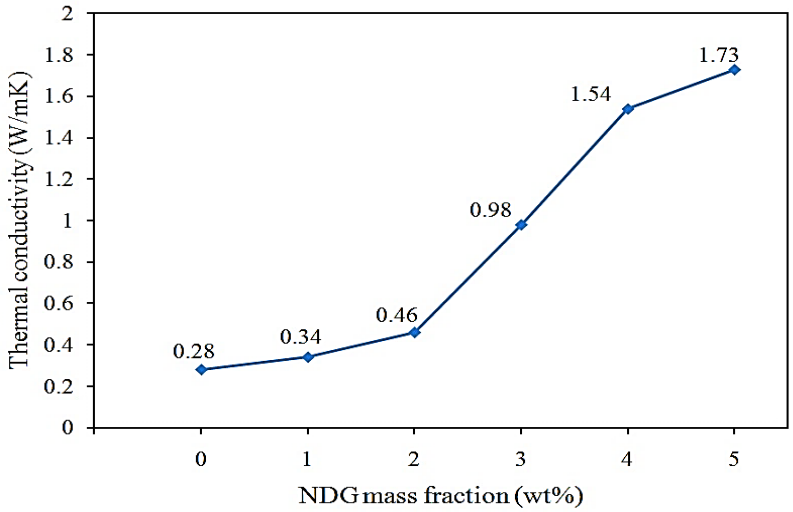

Figure 4-32: Thermal conductivity of PA and PA/NDG composite PCMs at 35 ℃

From the data presented in Figure 4-32, it can be seen that the thermal conductivities of the PA/NDG composites (S1 to S5) clearly improved compared to the pure PA. The maximum enhancement was 517% by adding only 5 wt% of NDG and it shows that NDG has a significant effect on the thermal conductivity of the PA. However, the figure also shows that the thermal conductivity does not increase linearly with increasing NDG loading. It was suggested that the arrangement of the layer structures in NDGs influences the interaction between PA and NDGs. By comparing S2 with S3, it can be seen that the enhancement was significant due to the virtual heat transfer network made by NDG layers. At the high NDG loading, as the content of NDG is further increased, the increasing of thermal conductivity slows down and exhibits a tendency to approach a limit. As a result, the PA/NDG composite PCMs achieved a much higher thermal conductivity than pure PA.

Plots of temperature versus time for PA and PA/NDG composite PCMs during heating and cooling are shown in Figure 4-33.These results show that the total charging and discharging time for PA was around 1100Sec and was decreased to 790Sec for S5 due to the higher thermal conductivity of the S5. By comparing the melting and freezing time of

PA with that of composite, it is obvious that the thermal storage and release rates were increased by 2.8 times.

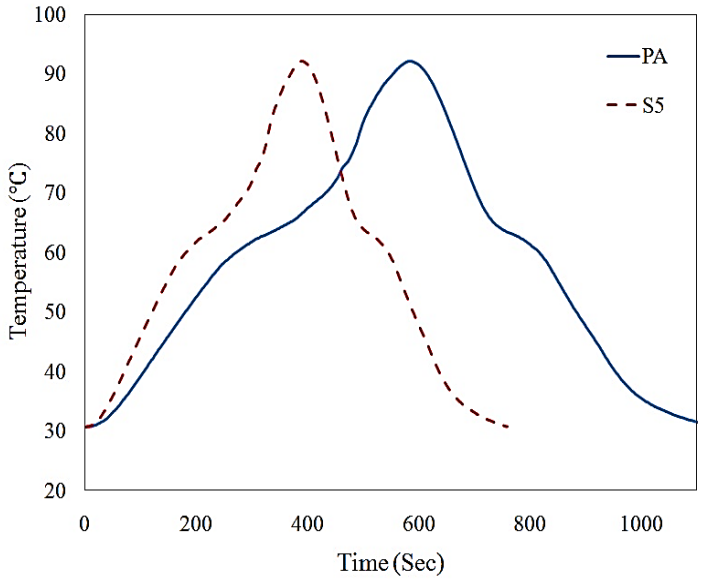

Figure 4-33: Charging and discharging graph of PA and PA/NDGs composite PCM

During cooling, temperature distribution images after 10 and 150 sec are shown in Figure 4-34 (a–f) for PA/NDG composites. The temperature distribution around the PA/NDG composites after 10 sec is almost the same for all samples while after 150 sec, the lowest temperature was found in S5 and the highest was in S1. From the results it can be seen that the differences between temperatures for S2, S3 and S4 are higher than can be explained by the thermal conductivity graph in Figure 4-32. The difference between thermal conductivity of these samples are higher than others so we could expect the results from the temperature distributions. These results also show that the thermal conductivity of composite samples was improved by using a higher mass fraction of the NDG.

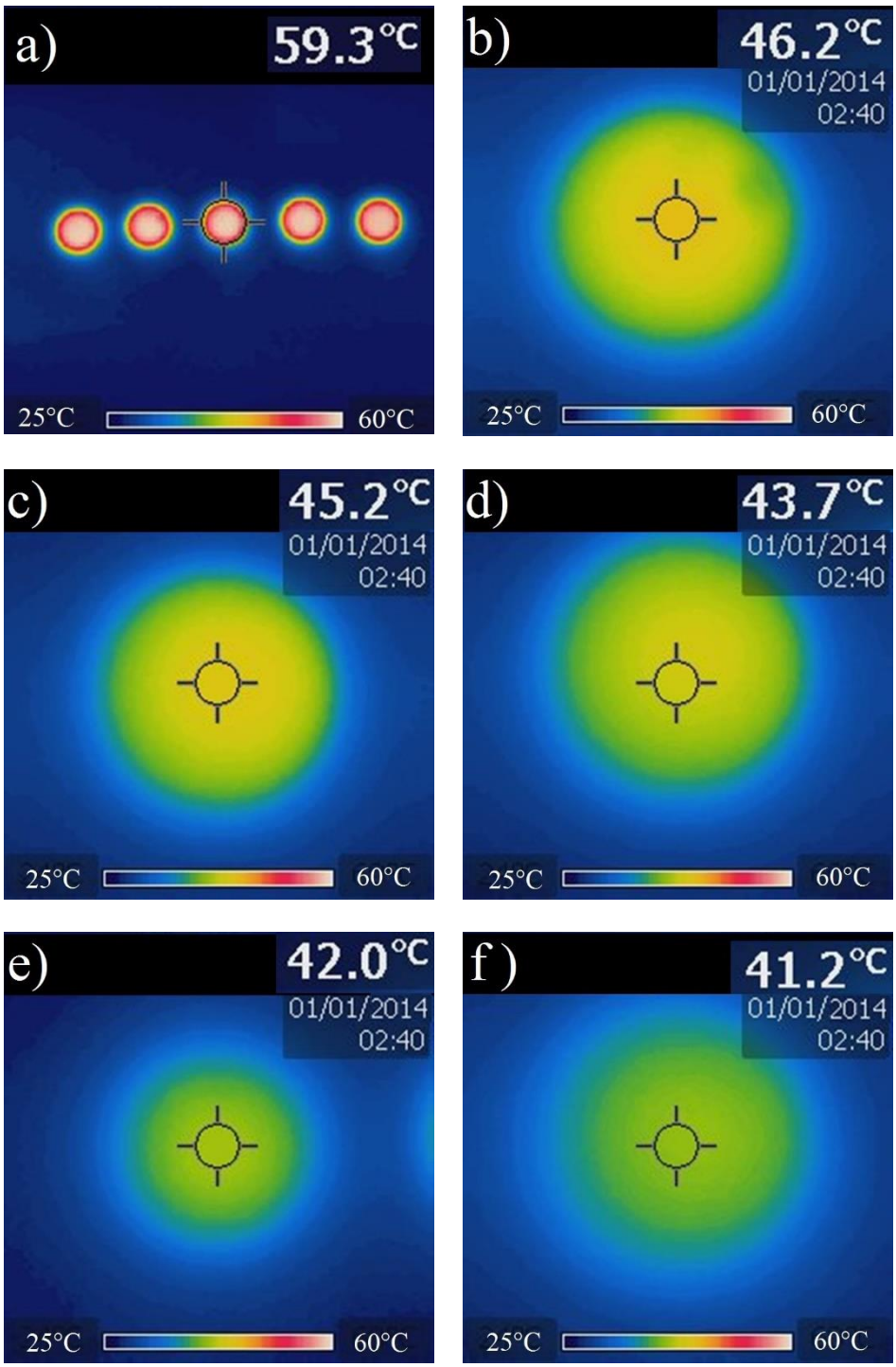

Figure 4-34: (a)Thermal images of the composite samples during the cooling time at 10 sec (b-f) thermal images at 150 sec for (b) S1 (c) S2 (d) S3 (e) S4 (f) S5

4.3.8 Thermal Effusivity of SSPCMs

The thermal effusivity is a measure of a material's ability to exchange thermal energy with its surroundings. The thermal effusivity is considered to be a critical physical quantity to depict the unsteady state heat transfer in a LHTES system. The effusivity of a material is the square root of the product of the thermal conductivity, density and heat capacity that can be calculated as follows:

$$e = \sqrt{\rho k c_p} \tag{4-3}$$

Where e (kJ/ (K.m^2.s$^{0.5}$)) is thermal effusivity, k is thermal conductivity (W/ (m·K)), ρ is density (kg/m^3) and c_p is specific heat capacity (kJ/ (kg·K)).The thermal effusivity of the PA and PA/NDG composite PCMs were calculated at 35 ℃ and listed in Table 4-11 .

Table 4-11: Thermal effusivity of PA and composite PCMs

Sample	Thermal effusivity(kJ/(K.m^2.s$^{0.5}$))
Pure PA	0.670
S1	0.758
S2	0.895
S3	1.335
S4	1.701
S5	1.836

The thermal effusivity of all composite PCMs is larger than that of pure PA, which is beneficial for the LTES systems. The thermal effusivity of PA was increased about 173% by adding only 5 wt% of NDG.

4.3.9 Electrical Resistivity

The electrical resistances of the composite PCMs were measured and resistivity of samples was calculated by taking the geometry of the sample into account using Equation (3-6).The electrical resistivity of different composite PCMs with a different mass fraction of NDGs are shown in Figure 4-35 .

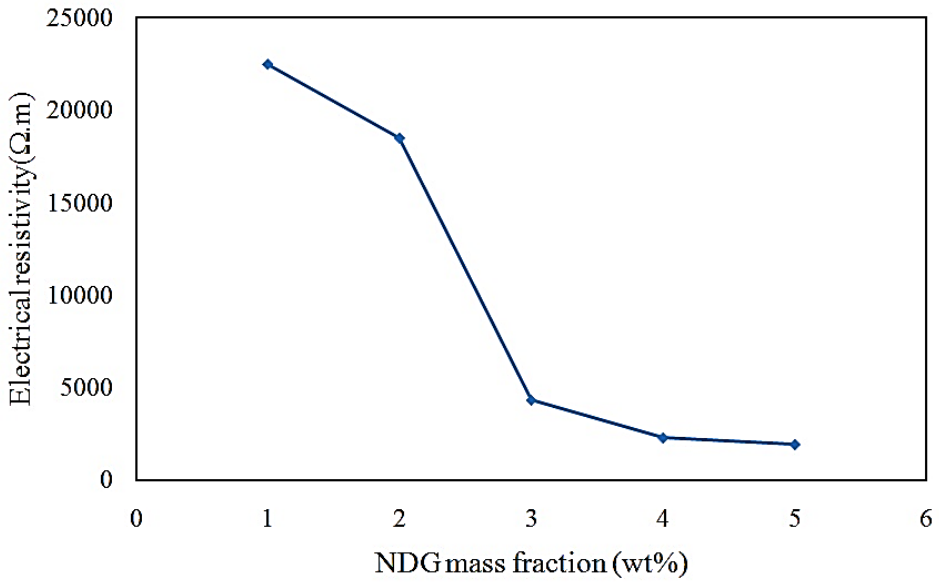

Figure 4-35: Electrical resistivity of the composite PCMs

The results demonstrate that NDG additives can enhance the electrical conductivity of PA considerably. A percolation threshold between 2 and 3 wt% is observed for PA/NDG composite PCM, the place where a significant reduction in resistivity from 18500 to 4310 Ω.m occurs. At 5 wt% loading, the electrical resistivity of the PA/NDG composite is around 1910 Ω.m. The extremely high aspect ratio of NDGs considerably improves the probability of contacts between neighboring flakes and thus raises the possibility of developing percolating networks at a lower loading content. The main increment in thermal conductivity also happened between 2 and 3 wt%, which shows that a percolating network forms between these two mass fractions.

4.3.10 Thermal reliability

Thermal reliability of the composite PCMs is critical to evaluate the potency of TES systems for long period-utility. Hence, a PCM needs to maintain its TES attributes even when it is put through a prolonged thermal cycling process. Thermal reliability is also one of the essential criteria employed for the selection of PCMs. For this specific purpose, in this research the thermal reliability of the composite PCMs was examined after the exposure to 1000 melting-freezing cycles. The changes of latent heats in composite PCMs after thermal cycling were considered to determine whether they are thermally reliable.

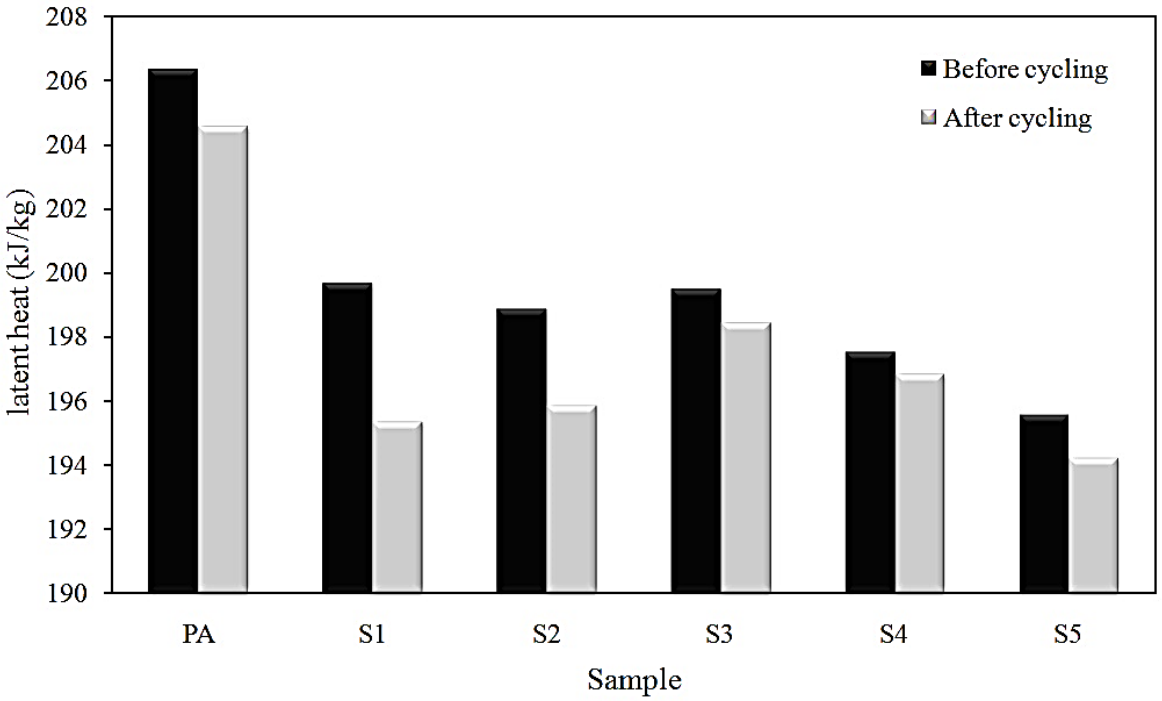

Figure 4-36: The latent heats value of the PCMs before and after thermal cycling

The composite PCMs had only one phase transition curve with particular onset temperatures as before the cycling. In other words, there were clearly no extra peaks related to chemical decomposition or phase segregation within the composites. Through comparing the latent heat values in Figure 4-36, the maximum change in latent heat capacity was determined as 4.3 kJ/kg for S1 and the minimum was 0.99 kJ/kg for S5.

These results suggested that the changes in the latent heat capacity of the composites after thermal cycling were less than 1% for S3, S4 and S5 demonstrate their good thermal reliability. The results mean that the variations of the phase change temperatures and latent heats are negligible for LHTES applications. Therefore, it can be concluded that the thermal properties of PA/NDG composite PCMs keep stable for at least 1000 cycling. Thermal energy storage density and speed of storing and releasing are two key factors when PCMs are applied to store thermal energy such as solar thermal energy. Besides, as far as the practical application is concerned, it is worthwhile to transform solid–liquid PCMs into form-stable PCMs. The prepared PA/NDG composite form-stable PCM by applying only 3wt% of the NDG possesses the merits of high thermal energy storage density (199.48 kJ/kg), high thermal conductivity 0.98(W/m.K) and good form stability. As a result, we believe that the prepared PA/NDG form-stable PCM certainly can find its application in low temperature solar-thermal applications.

4.4 Graphene Nanoplatelets (GNPs) SSPCMs

Graphene nanoplatelets (GNPs) possess many desirable properties ideal for the PCM applications. Like other carbon-based systems, the graphene sheets that make up the nanoplatelets are thermally and electrically conductive. Compared to nanotubes or carbon fibers, the platelet structure delivers lower thermal contact resistance at lower loading levels, leading to higher thermal conductivity compared to other carbon particles or fibers. Furthermore, the large specific surface area (300–750 m^2/g) of GNPs is advantageous for shape-stabilization over the solid–liquid transition of PCMs since it helps to grasp the liquid by surface tension.

4.4.1 Morphology and Dispersion

Figure 4-37 shows the SEM images of different surface area of GNPs and PA/GNPs composite PCMs. As can be seen from the SEM images, the as-received GNP significantly agglomerated and stacked together. As a result of the irregular nature of the

agglomerated GNPs, their size (in-plane diameter) spread widely within the range of 5−50 μm. Figure 4-37(a), (c) and (e) display raw GNPs with different surface areas. The surface area is a very important factor in shape stabilization of composite PCMs. Therefore, a higher surface area of GNPs will form a mechanically interconnected composite and offer superior mechanical reinforcement on the PCMs. Figure 4-37(b), (d) and (f) shows that palmitic acid (PA) was adsorbed uniformly by GNPs. This suggests that there is a strong interface between graphene and PA molecules. PA will be easily held by the capillary force due to the high specific area of GNPs. Good dispersion and network formation facilitates heat transfer and allows phonons to travel efficiently through the graphene fillers and between the flakes. It is well-known that the type of the polymer matrix, degree of exfoliation of the graphene flakes, orientation of the fillers, and interfacial interaction influences the thermal transport in graphene nanocomposites.

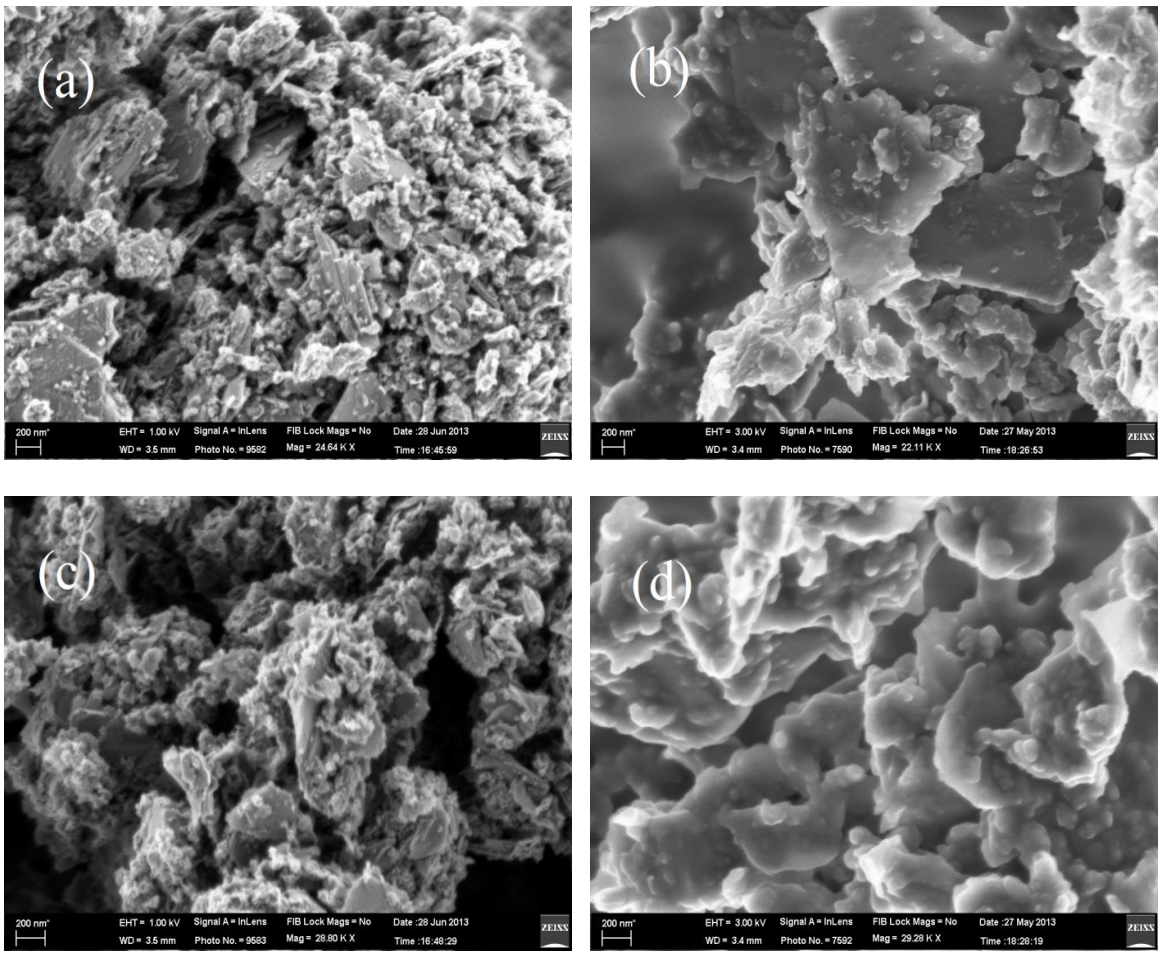

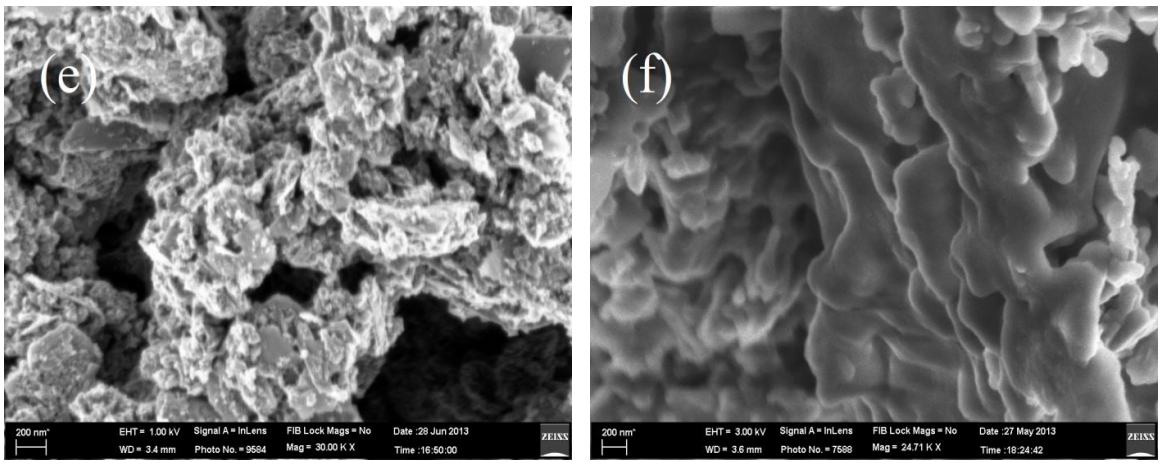

Figure 4-37: SEM images of (a) GNPs /300 (b) S1 (c) GNPs/500 (d) S2 (e) GNPs/750 (f) S3

Figure 4-38 (a) shows TEM images of graphene nanoplatelets. GNP exhibits a flake structure with various in-plane sizes and indicated well-ordered graphene layers. The thickness of GNP is <10 nm (~20 graphene layers). The darker parts in Figure 4-38(b) show that PA was well adsorbed by GNPs.

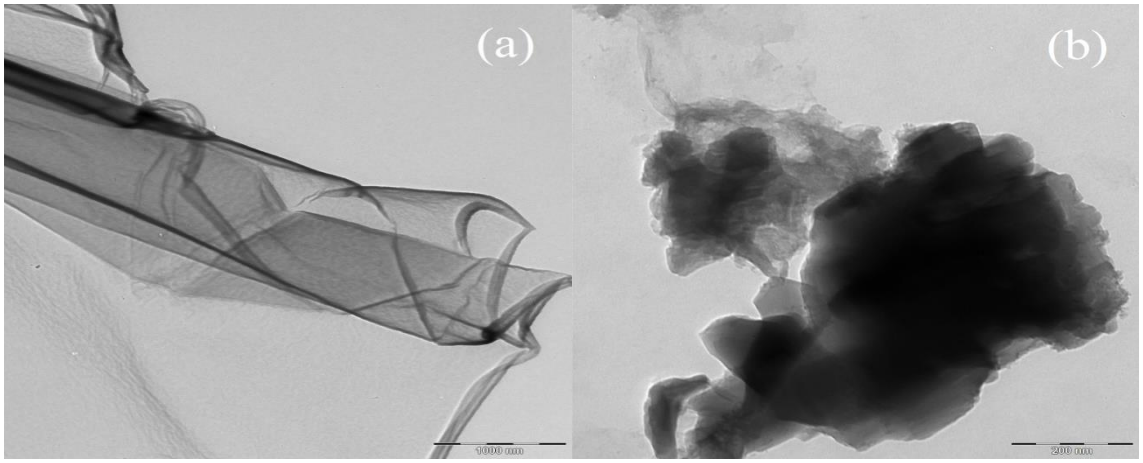

Figure 4-38: TEM images of (a) GNPs (b) PA/GNPs composite PCM

4.4.2 FT-IR Analysis

Figure 4-39 shows the FT-IR spectra for PA, GNPs and PA/GNPs composite PCM. For GNPs the peak at 3450 cm^{-1} is attributed to O—H stretching vibrations and the absorption peak of GNPs at 1582 cm^{-1}, assigned to C═ C vibrations. The peaks at 2915.02 and 2853.57 cm^{-1} are the symmetrical stretching vibration peaks of –CH2 in PA. The absorption peak at 1720 cm^{-1} is attributed to C-O stretching vibrations. The peak at

1321 cm^{-1} corresponds to the in-plane bending vibration of the –OH group of PA and the peak at 910 cm^{-1}corresponds to the out-of-plane bending vibration of the –OH functional group and the peak at 730 cm^{-1}represents the in-plane swinging vibration of the –OH functional group . It can be clearly seen from both FT-IR spectra that there is no shift in the above main absorption peaks and in composite PCM, PA absorption peaks can be clearly seen. This shows that there is no chemical reaction between functional groups of PA and GNPs.

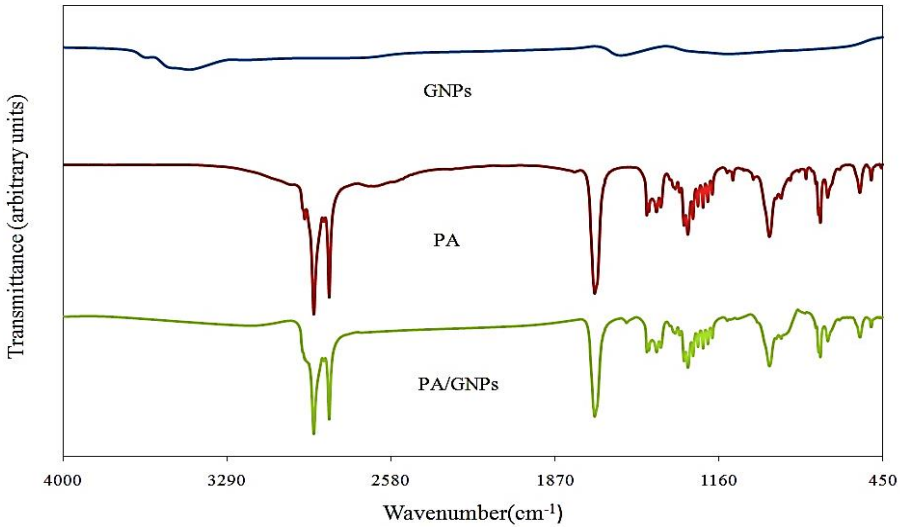

Figure 4-39: FT-IR spectra of (a) GNPs (b) PA(c) PA/GNPs SSPCM

4.4.3 XRD Analysis

Figure 4-40 displays the XRD patterns of GNPs, PA and PA/GNPs composite PCM. The XRD pattern of the GNPs confirms well with Li et al. (2011b). The major peak of GNPs appeared at angle of 2θ=26°. The XRD patterns of the composite PCMs mainly confirm that the crystal formation of the PA in the composites PCM did not change during the impregnation process. The intensity of the X-ray peaks of PA in the GNPs composites is lower than that of pure PA. This shows that due to the limitation of the crystals of the PA by pores of the GNPs composite, the crystallite size of the PA becomes smaller in the composites (Zhang et al., 2012c) .

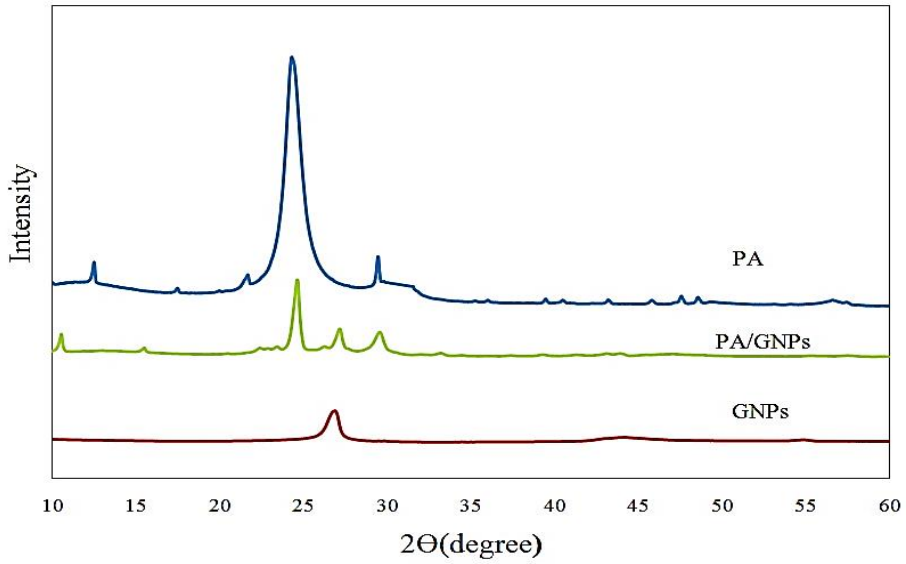

Figure 4-40: XRD patterns of PA, GNPs and PA/GNPs composite PCM

4.4.4 Energy Storage Properties

The thermal energy storage properties of PA and the shape stabilized PCMs were investigated by means of DSC. For each composite PCM sample, three DSC experiments were performed with individual samples taken from different sites of the pellets, and the mean value of the melting and solidification temperatures and enthalpies are shown in Table 4-12 . Typical DSC curves of PA and PA/GNPs form-stable PCMs are shown in Figure 4-41and Figure 4-42. As can be observed, just one major transition peaks have been clearly seen, where the sharp peak ought to be caused by the heterogeneously nucleated rotator–liquid transition which shows the solid–liquid phase change of PA. As can be seen in Table 4-12, the melting and solidification temperatures are determined to be 60.58℃ and 59.51℃ for the pure PA and 61.16℃ and 60.20℃ for the S3, respectively. The melting and solidification latent heats are measured to be 205.53kJ/kg and 209.42kJ/kg for the PA and 188.98kJ/kg and 191.23kJ/kg for the S3, respectively.

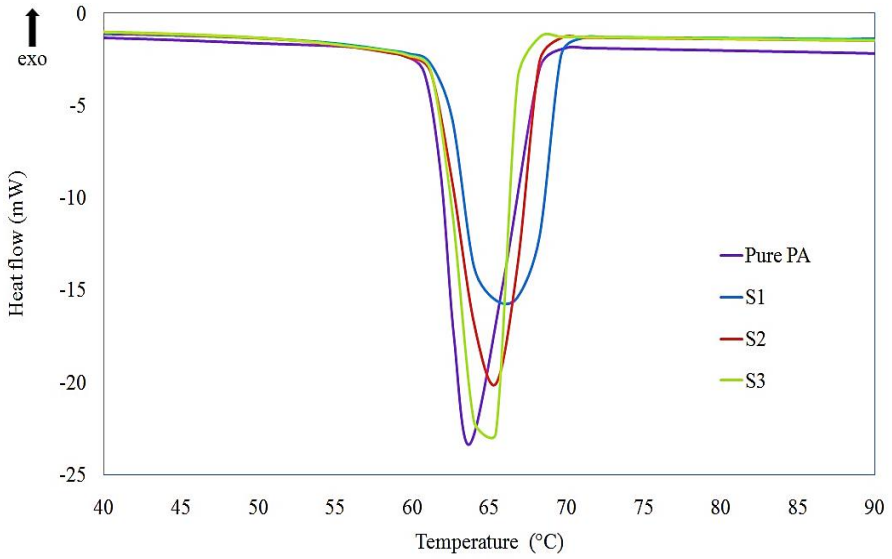

Figure 4-41: Melting DSC curves of the Pure PA and S1, S2 and S3

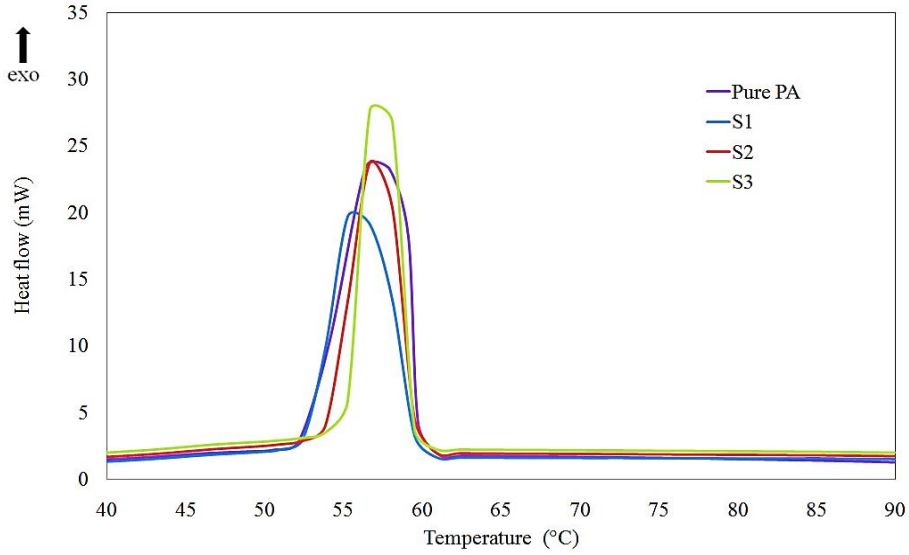

Figure 4-42: Solidification DSC curves of the Pure PA and S1, S2 and S3

In composite PCM, high latent heat storage capacity is a result of high phase change material content. The mass percentage of PA was calculated based on Equation (4-1). Hence, the PCM mass percentages of S1, S2 and S3 were 77.99 wt%, 83.06 wt% and 91.94 wt%, respectively. These results confirmed that increasing of specific surface area from 300 to750 m^2/g will significantly affect the amount of PCM that can be absorbed by GNPs.

Table 4-12: DSC results of pure PA and PA/GNPs SSPCMs

Sample name	Palmitic acid (Wt %)	Melting		Solidification	
		Melting temperature T_m(℃)	Melting latent heat ΔH_m(kJ/kg)	Freezing temperature T_f(℃)	Freezing latent heat ΔH_f(kJ/kg)
Pure PA	100	60.58	205.53	59.51	209.42
S1	77.99	61.87	160.31	60.52	168.43
S2	83.06	61.32	170.72	60.31	175.34
S3	91.94	61.16	188.98	60.20	191.23

The difference between melting and solidification temperature of pure PA and S3 was 1.07 and 0.96, respectively which shows that supercooling degree of composite PCMs is smaller than pure PA during solidification process. For all prepared samples, S3 has the highest $\Delta H_{melting}$ that is 188.98kJ/kg, corresponding to a 91.94% loading of PA, and no leakage of PA could be found when it was warmed up over the melting point of PA as is shown in Figure 4-43.

Figure 4-43: Image of S3 at 25 and 80℃

4.4.5 Dropping Point

The shape stabilization of PCMs will solve these problems and will change thermal conductivity of PCMs depending on additives that have been used. To evaluate of the shape stability of PA/GNPs composite PCM, we used a dropping test to measure dropping point of composite PCMs and the results are shown in Table 4-13.

Table 4-13: Dropping points of PA and PA/GNPs SSPCMs

Sample	Dropping point (℃)
PA	65.03
S1	150.80
S2	196.4
S3	>375

The PA/GNPs composite PCMs show great enhancement in form-stability, without any liquid seepage for the duration of solid–liquid phase transition because of the capillary forces. The results indicate that the shape of the composite can be retained up to 150.80℃ significantly more than the operating temperature range of palmitic acid PCMs.

4.4.6 Thermal Stability

The TGA and DTG curves of GNPs with different surface area is shown in Figure 4-44 (a) and (b).The results indicate that there are two steps of weight loss for GNPs, namely, the water weight loss that occured at 30-100 and decomposition of GNPs around 630. It can be seen that the decomposition temperature will decrease with increasing surface area of the GNPs. As shown in Figure 4-44 (c) and (d) for pure PA and PA/GNPs composite PCMs, the initial step takes place for a temperature between 230 and 350℃ that belongs to the thermal degradation of the PA molecular chains while the

next step happens for a temperature above 350℃ as a result of thermal degradation of the GNPs.

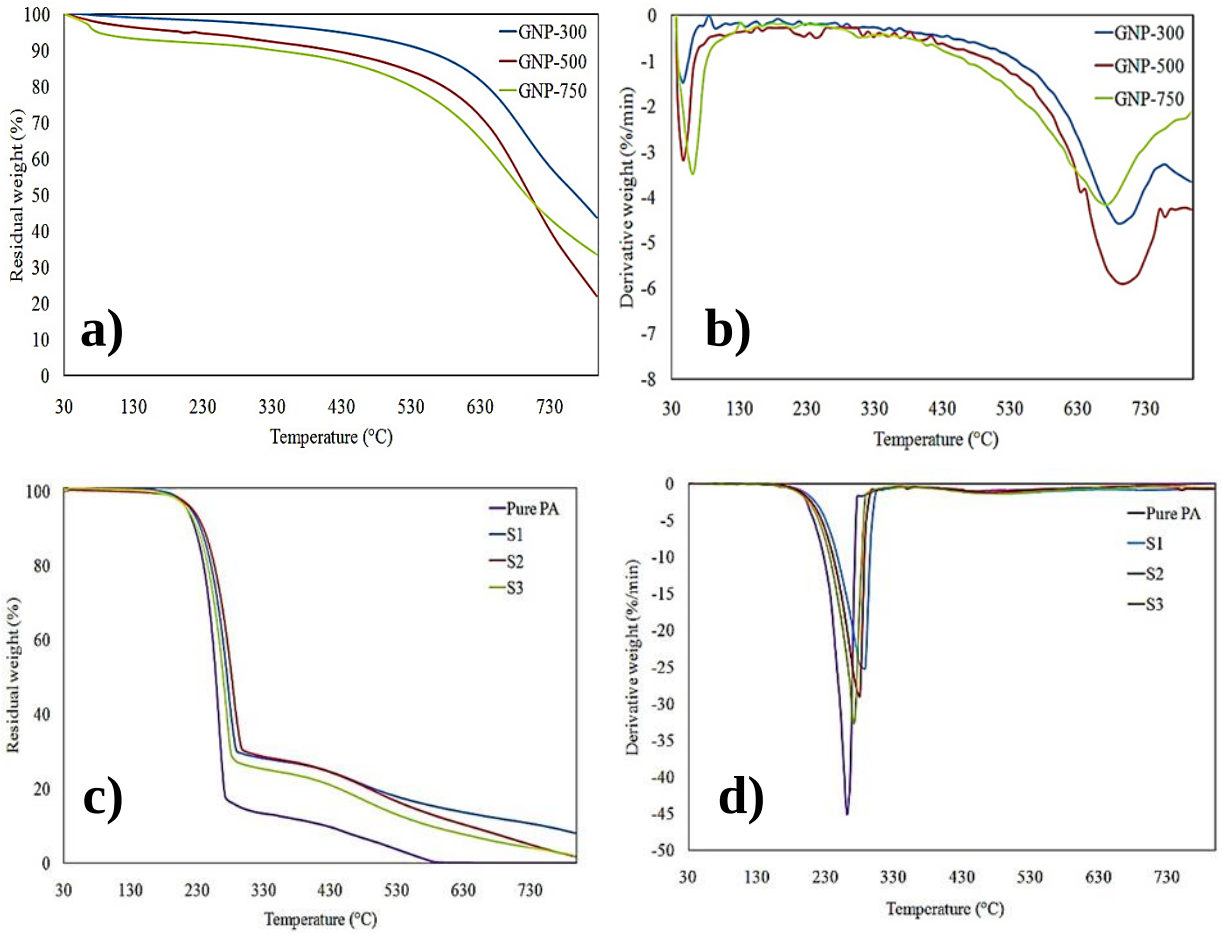

Figure 4-44: TGA and DTG curves of the GNPs (a,b), PA and PA/GNPs(c,d)

Table 4-14 shows the degradation temperatures (T_1, T_2) of PA and PA/GNPs composite PCMs. The weight loss temperature of PA (T_1) was improved by 28.5, 18.66 and 10.63 for S1, S2 and S3, respectively. This shows that thermal stability of PA was significantly improved by GNPs due to the high thermal stability of GNPs and synergistic effect between PA and GNPs. The GNPs insulating the underlying material and slowing the escape of the volatile products generated during thermal decomposition.

Table 4-14: TGA data of PA and PA/GNPs SSPCMs

samples	T_1(℃)	T_2(℃)
PA	262	---
S1	288.5	695.83
S2	280.66	688.5
S3	272.83	664.5

4.4.7 Thermal Reliability of PA/GNPs SSPCMs

Materials have a tendency to lose their thermal performances after repetitive thermal cycles and the phase transition temperatures and enthalpies change considerably. Nevertheless, an appropriate PCM should have reliable thermal properties with consistent phase change cycles without any changes. Thermal cycling test was done for 2500 cycles on S3 as it had the maximum amount of PA absorbed by GNPS. The DSC curves of melting and solidification for S3 before and after thermal cycling are shown in Figure 4-45.

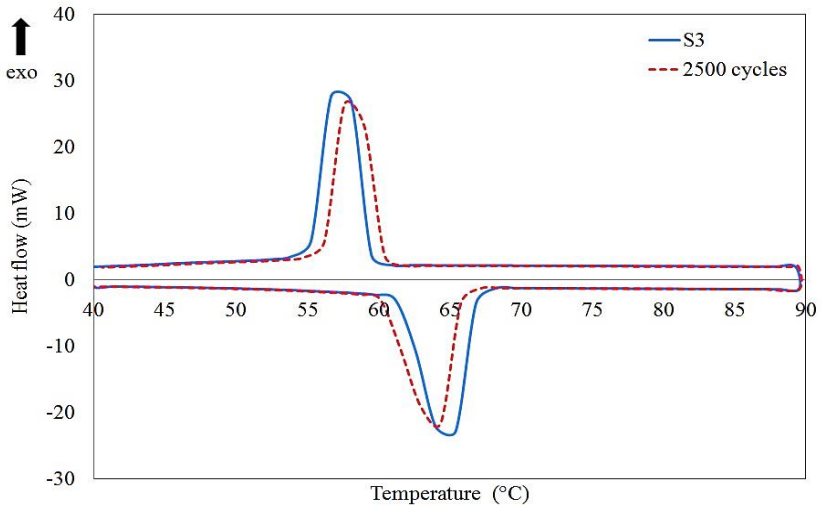

Figure 4-45: The DSC curves of S3 before and after 2500 cycles

The melting and solidification temperature of S3 after 2500 cycles was changed by -1.23 and 0.96℃ , respectively. The latent heat of S3 was changed by -2.97% for melting process and -2.43% for freezing process after 2500 cycles. The changes in

melting and freezing temperature of PA/GNPs composite PCMs are certainly not considerable for LHTES applications. Also it can be regarded that PCM composite indicates great thermal reliability after massive number of thermal cycles. The reductions in latent heat values are satisfactory for LHTES applications for composite PCM. However, the deviations do not lead to any new secondary peak formations different than the main products. Hence, it can be declared these materials also have a good chemical stability for the duration of 2500 thermal cycles.

4.4.8 Thermal conductivity and Electrical Resistivity

The thermal conductivity of pure PA and S1, S2 and S3 was measured by a thermal conductivity apparatus (KD-2 Pro) using the hot wire method at 30 and 80℃. The electrical resistivity of PCMs was calculated as described previously. The thermal conductivity and electrical resistivity of PA and PA/GNPs composite PCMs are shown in Table 4-15 .

Table 4-15: Thermal conductivity and electrical resistivity of PA and SSPCMs

Samples	Thermal conductivity(W/m.K)		Electrical resistivity($\Omega.\mathrm{m}$)
	Solid state (30℃)	Molten state (80℃)	
PA	0.29	0.285	3.19×10^6
S1	2.75	2.54	7.6×10^2
S2	2.43	2.17	15.92×10^2
S3	2.11	1.84	21.08×10^2

The electrical resistivity of composite PCM had significant decreased by four orders of magnitude from 10^6 to 10^2. These variations in the percolation threshold as well

as the resistivity are generally because of the different aspect ratios and sizes of the GNPs, given that the GNPs tend to be uniformly distributed inside the matrix. As shown in Table 4-15, in solid state (25℃) and molten state (80℃), the thermal conductivity of PA/GNPs shape stabilized PCM is much higher than PA. Considering the very high theoretical conductivity of graphene (4840-5300 W/mK), one might expect a more dramatic improvement in thermal conductivity of the composite with the addition of graphene fillers. However, it has been reported that since the dominant heat transfer mechanism is due to the lattice vibrations or phonons; poor phonon coupling in the vibrational modes at the polymer-filler and filler-filler interfaces cause thermal resistance, also called the Kapitza resistance, which decreases the overall thermal conductivity of the material. The thermal conductivity of the S1, S2 and S3 is 2.75, 2.43 and 2.11 W/m.K in the solid state and 2.54, 2.17 and 1.84 W/m.K in molten state, respectively. Thus the thermal conductivity of PA/GNPs composite PCM is about 10 times that of PA. These results also verified by comparison between charging time of PA and PA/GNPs composite PCM as shown in Figure 4-46.

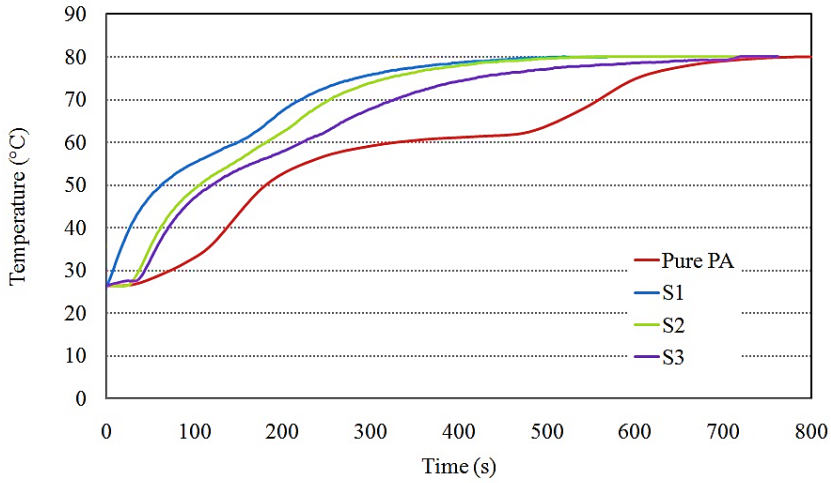

Figure 4-46: Charging graph of PA and PA/GNPs SSPCMs

As can be seen from Figure 4-46, the pure PA needs 360s to reach to molten state while the time is needed for S1, S2 and S3 was 150,182 and 214s, respectively. This

indicates that PA/GNP composites have a significantly higher thermal conductivity than pure PA and that heat transfer process in composite PCM is more intensive.

4.5 Reduced Graphene Oxide (RGO) SSPCM

In the present work, for the first time one step preparation of PCM composite consisting of palmitic acid (PA) and lowest amount of reduced graphene oxide (rGO) as a supporting material is introduced. Graphene oxide sheets are functionalized with long change alkylamine, n-Butylamine, to adsorb palmitic acid (PA) and graphene sheets self-assembled simultaneously into the form-stable structure. Connected graphene network enhances heat transfer across PA and keeps the molten PA in the pores of the structure by capillary force. This method eliminates the necessary means for freezdrying and impregnation as it has been utilized for all the carbonaceous composite PCMs before. The enhancement of thermal conductivity, thermal stability and sunlight adsorption of the prepared PCM composites are presented and discussed in detail. The enhanced thermal properties, together with high latent heat and excellent recyclability make the prepared composites promising candidates as heat storage materials for real application. The SSPCMs samples were prepared with different mass percentage of GO (0.5 -1-1.5 and 2 wt %) and named S1 to S4, respectively.

4.5.1 Mechanism of Self-Assembly

It is well known that the hydrophilic hydroxyl, epoxy and carboxyl functional groups are responsible for stable colloidal dispersion of GO sheets in water. It was also reported that the ionization of carboxylic groups creates electrostatic repulsion between GO sheets which protects them from aggregation in aqueous solutions (Li et al., 2008). During chemical reduction of GO by n-butylamine, its amine ($–NH_2$) functional group was reacted with epoxy and carboxyl functional groups of GO via ring opening reaction and condensation reaction, respectively (Compton et al., 2010; Kim et al., 2014; Peng et al., 2012). Reduction of GO by n-butylamine diminished the repulsion force between

graphene sheets and n-butylamine-functionalized rGO became hydrophobic (Tong et al., 2014). Conversely, combination of π-π stacking, hydrogen bonding and hydrophobic interactions enhanced the bonding force between graphene sheets and consequently promote gelation (Bai et al., 2011). Simultaneously, PA adsorbed and retained in graphene gel network via hydrophobic Van der Waals interaction between the n-butylamine and PA aliphatic chains (Fahmi & Chang, 2013). As the reduction continued, the functionalized graphene nanosheets and PA assembled more tightly to form shape stabilized composite with interconnected network structure. The self-assembly process is shown schematically in the figure below:

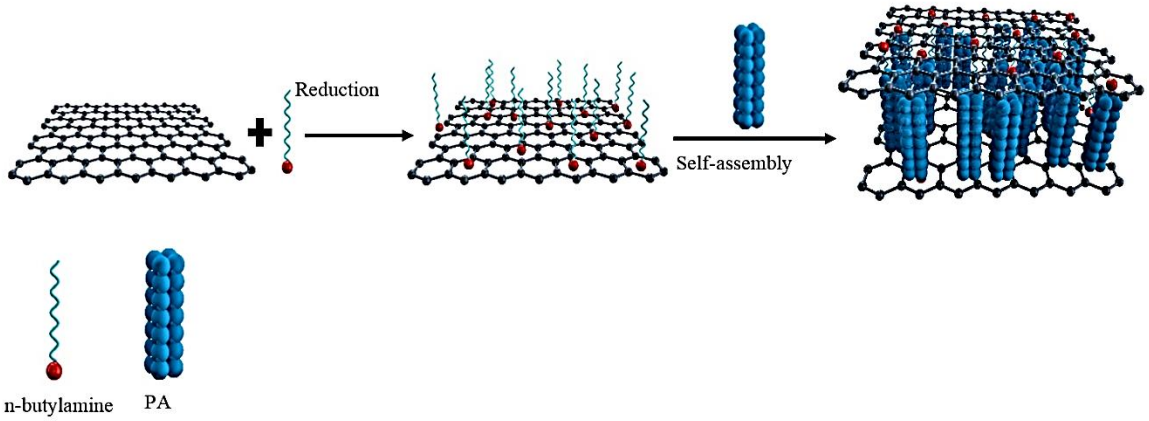

Figure 4-47: Schematic of the self-assembly process of PA/RGO SSPCMs

4.5.2 Morphology and Structure

Figure 4-48 demonstrates the broken cross section of the PA/RGO SSPCMs prepared by self-assembly process. The RGO sheets are either inlayed in the PA matrix confirmed by the white lines protruding from the background or lying on the surface suggested by their irregular but sharp edges completely different from the smooth and soft PA. The overlapping and interlocking flexible graphene sheets resulted in the formation of the interconnected layer structure of RGO and PA. The interfaces of the PA and functionalized graphene combined compactly due to the hydrophobic interaction between them during self-assembly.

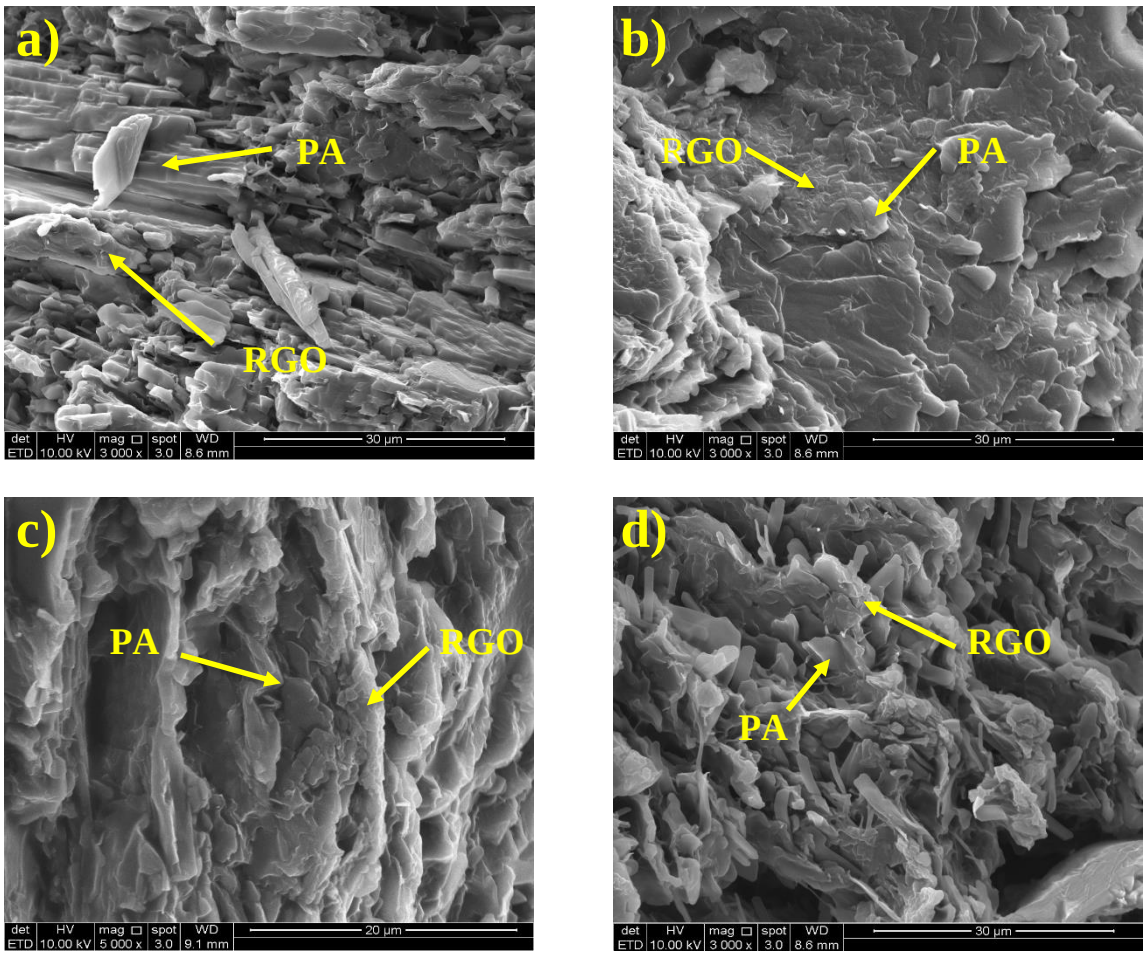

Figure 4-48: SEM images of (a) S1 (b) S2 (c) S3 (d) S4

4.5.3 FT-IR Analysis

The SSPCMs were also characterized by FTIR spectroscopy to reveal specific interactions between PA, n-butylamine and RGO. Figure 4-49 shows the FTIR absorption spectra of the characteristic peaks of PA and PA/RGO composites. From Figure 4-49 , it can be clearly seen that most absorption peaks of the main functional groups of PA appear in the spectra of the PA/RGO SSPCMs with only a slight shift. No significant new absorption peaks occurred in the spectra of SSPCMs compared with pure PA, which indicates that no new chemical bonds generated between PA and the matrix. However, the new peak appeared around 1580 cm^{-1} which belongs to the –NH bending vibration. This result shows that the amine functional group of n-butylamine reacts, mainly, with the carboxylic and epoxy functional groups of GO and there was a slight interaction with the carboxylic functional group of PA. The temperature kept at 70ºC as the carboxylic functional group of PA has less reaction with n-butylamine at this temperature.

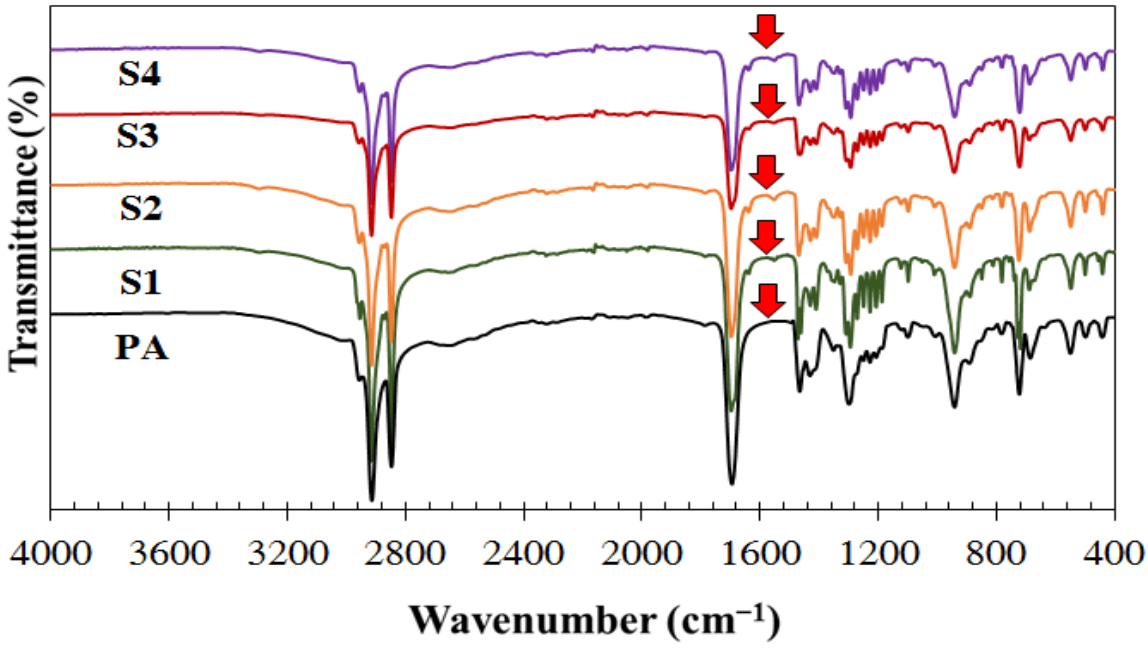

Figure 4-49: FT-IR spectra of pure PA and PA/RGO SSPCMs

4.5.4 Raman Spectra

The well-known D and G bands appeared around 1346 and 1600 cm^{-1} in Raman spectra of GO and PA/RGO composite, respectively (Figure 4-50). As is known, D band is rising from breathing mode of κ-point phonons of A_{1g} symmetry which can be associated with structural defects and partially disordered structures of the sp^2 domains , while G band is related to E_{2g} vibration mode of sp^2 carbon atoms in graphitic structure (Akhavan et al., 2012; Ferrari & Robertson, 2000).Commonly, the intensity ratio of D to G bands (I_D/I_G) has been used to measure the disorder degree of sp^2 clusters in a network of sp^3 and sp^2 bonded carbons. The I_D/I_G for GO decreases from 0.75 to 0.54 in PA/RGO composite which indicates the restoration of sp^2 domains and improving the graphitic degree of graphene nanosheets in SSPCM due to reduction effect (Akhavan et al., 2010; Sheng et al., 2011).

The peak at 2845 and 2885 cm^{-1} are symmetric and asymmetric vibration mode of $–CH_2$ group and together with peaks at 1063, 1102, 1131, 1179, 1299 and 1441 cm^{-1} can be assigned to PA (Brown et al., 1987; Krafft et al., 2005). In the Raman spectra of

PA/RGO composite all the peaks for PA has been observed which are consistent with FT-IR results and confirms the composition of PA and RGO.

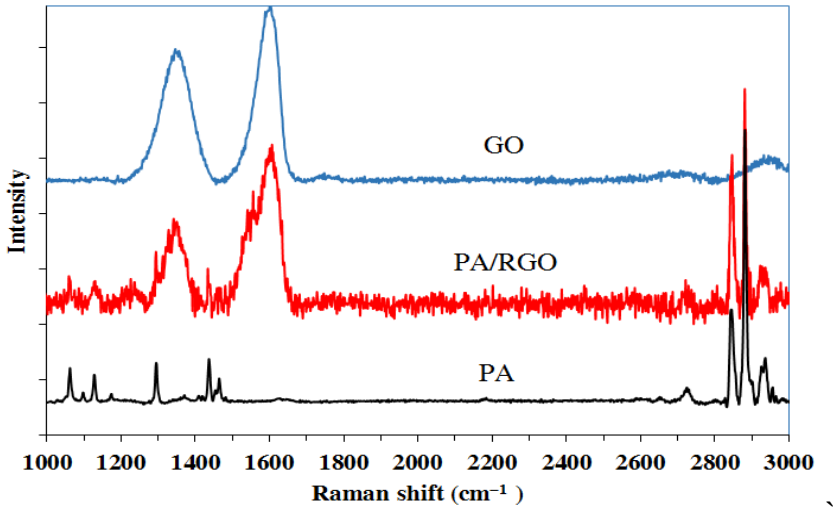

Figure 4-50: Raman spectra of pure PA, GO and PA/RGO composite PCM

4.5.5 Thermal Energy Storage Properties

Thermal energy storage properties of pure PA and PA/RGO composites with different RGO mass fractions are investigated with DSC test. The corresponding thermal properties are summarized in Table 4-16 which, T_{pm} and T_{pf} are melting and solidifying peak temperature and ΔH_m and ΔH_f are latent heat of melting and solidifying, respectively. The phase change enthalpy is an important element in PCMs and could be utilized as a measure to assess the thermal energy storage capacity of the PCM. Figure 4-51shows that with the addition of GO, the melting enthalpy of PA decreases. The reduction is ~3.5% when it comes to ~2% graphene filler content. This can be estimated by considering the fact that some of the PCM volume is replaced by the graphene sheets that won't go through phase change. We did not raise the graphene weight fraction beyond 2% in order to avoid further decrease in the melting enthalpy.

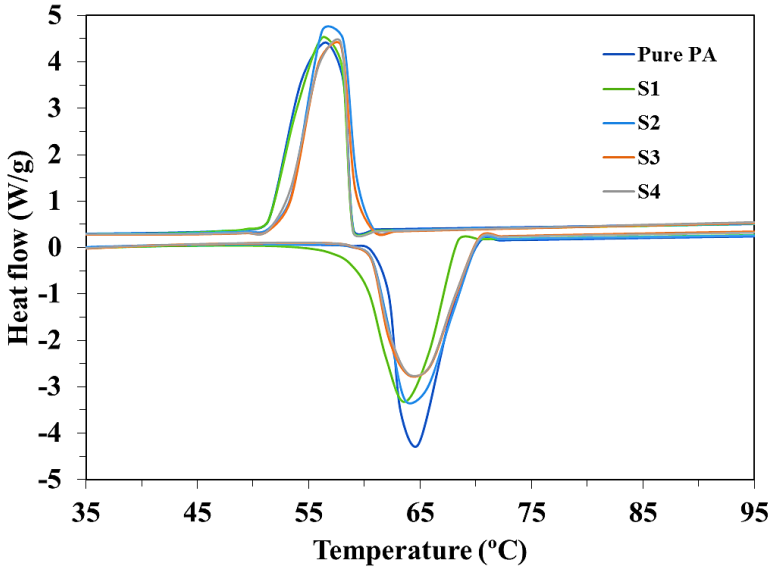

Figure 4-51: DSC plots of pure PA and PA/RGO SSPCMs

All the composite shows one peak in endothermic and exothermic DSC curves in Figure 4-51, indicating the latent thermal energy storage of PA during melting and solidifying process. The phase change properties of PCM composites are slightly effected by n-butylamine and supporting material (RGO) during self-assembly process. T_{pm} and ΔH_m for PCM composites are reduced compare with pure PA due to the reaction of carboxylic group of PA with amine group of n-butylamine which decreased the amount of crystalized PA in composites. Only crystalized PA would contribute to latent heat during melting and solidifying. It is clear that higher n-butylamine /PA fraction leads to lower crystalized PA in SSPCMs. The broader DSC peaks for PCM composites can be explained by increasing the crystallinity of PA by interaction with the functionalized surface of supporting material. However, interpretation of the physics underlying this phenomenon remains unclear.

Table 4-16: Thermal energy storage properties of PA and PA/RGO SSPCMs

Sample name	Palmitic acid (wt %)	Melting		Solidification	
		Melting peak temperature T_{pm} (℃)	Melting latent heat ΔH_m(kJ/kg)	Freezing Peak temperature T_{pf} (℃)	Freezing latent heat ΔH_f(kJ/kg)
Pure PA	100	64.87	203.48	56.50	206.21
S1	98.39	63.68	200.22	56.20	202.91
S2	97.92	63.65	199.26	56.18	200.69
S3	96.97	63.94	197.33	57.90	199.43
S4	96.78	63.90	196.93	57.95	198.83

4.5.6 Thermal Stability

The thermogravimetric (TGA) and derivative TG (DTG) analysis were performed to examine the thermal stability of composite PCMs and graphs are shown in Figure 4-52 . Two-step thermal degradation processes can be observed for PCM composite in DTG curve. However, the second step cannot be recognized in the TGA diagram of composite as it happens continuously.

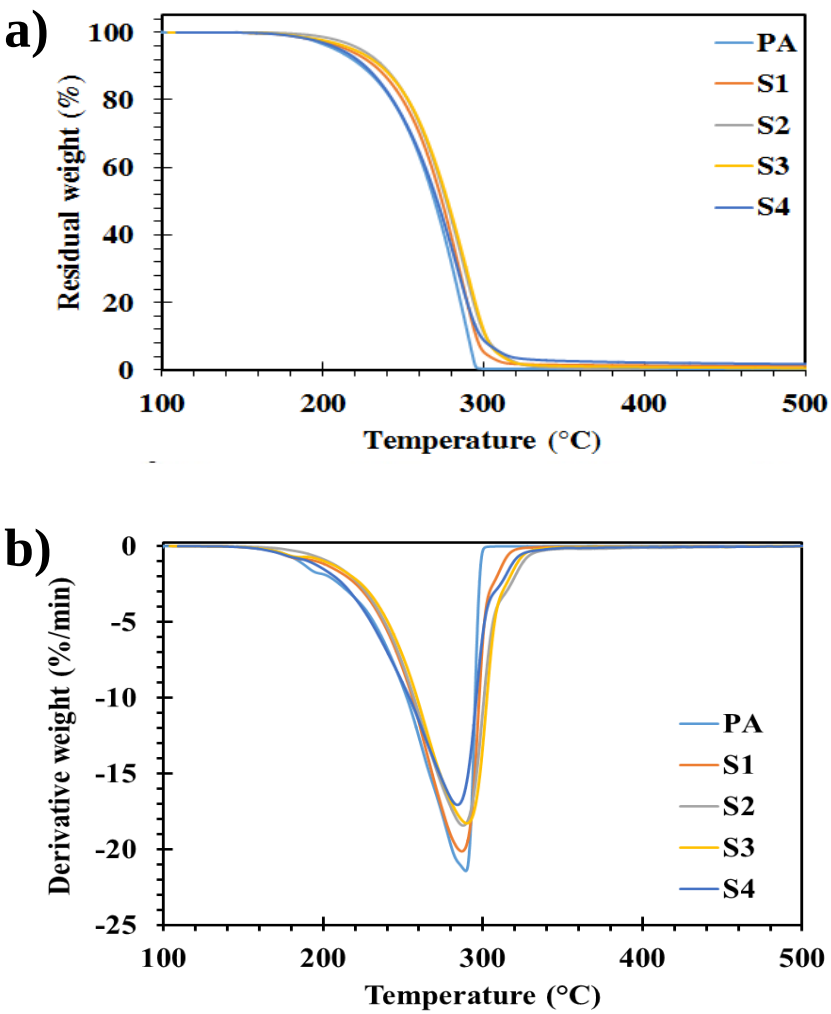

Figure 4-52: (a) TGA and (b) DTG curves of PA and PA/RGO SSPCMs

The first step corresponds to the volatilization of PA in all diagrams. TGA curve shows that pure PA decomposes between 177 to 300 ºC, while PA/RGO SSPCMs show a weight reduction at a higher temperature around 185 to 330 ºC. Further weight losses at 332 to 400ºC shows the elimination of the remaining RGO functional groups in high temperature. The RGO structure act as a protecting layer and the interaction of PA with the surface of RGO slows the escape of the vaporized PCM during thermal degradation. The results show that the composite PCMs exhibit high thermal stabilities.

4.5.7 Shape Stabilization Properties

The shape-stabilized properties of the pure PA and PCM composites were examined by using the hot plate and digital camera. Briefly composite PCMs were placed

on the hot plate and temperature raised to 90 ºC. After 30 min of pure PA added, changes in the samples were observed by digital camera. The black monoliths remained solid unlike the pure PA, which melted completely into liquid as shown in Figure 4-53.The surface of composites was moist, but no liquid leakage from the composites was observed during the heating process. The hydrophobic surface of RGO and capillary effect of micro scale pores in the composite structure prevent the molten PA from leaking.

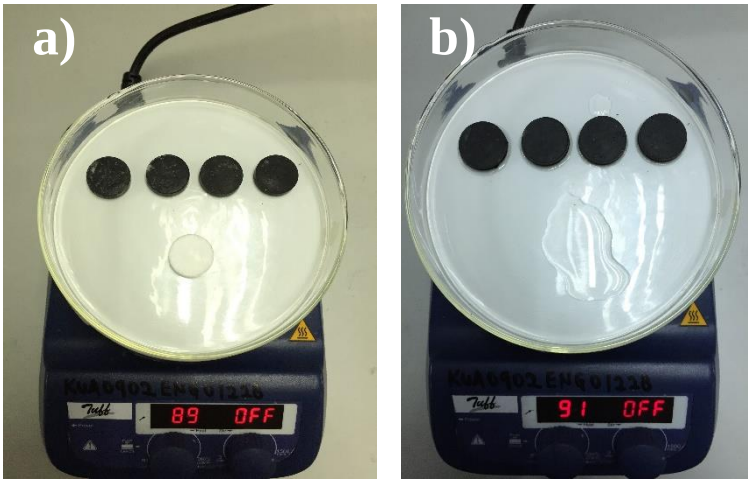

Figure 4-53: Images of PA and PA/RGO SSPCMs a) before b) after melting point of PA

4.5.8 Solar-Thermal Conversion

The photon-to-thermal energy conversion of pure PA and PA/RGO SSPCM was investigated as it is was explained in Section 3.4.16. The samples were placed under the simulated sunlight radiation and the temperature evolution of samples was recorded by a sensor and data collection system. Temperature of composite PCM rapidly increased by absorbing the solar energy (Figure 4-54). The inflation at the melting point of composites illustrates that the phase transition of samples has accrued during solar radiation, due to the fact that RGO absorbed the light radiation and convert it into the thermal energy .The highest recorded temperature of light to heat conversion was about 82-83 °C and temperature equilibrium happened at this point. However, the highest temperature for pure PA was only 53 °C and no visible melting was observed as it has low solar to thermal

conversion efficiency. The temperature of composites reduced after removing the light source. The freezing graph shows the solidification process of PA in the composites. It is obvious that the wide black surface of RGO captured the photon energy and heated the PA molecules, then PA stored and released the thermal energy through the phase transition (Wang et al., 2013). The higher content of RGO as a photon captor and thermal conductor, leads to the faster temperature rising.

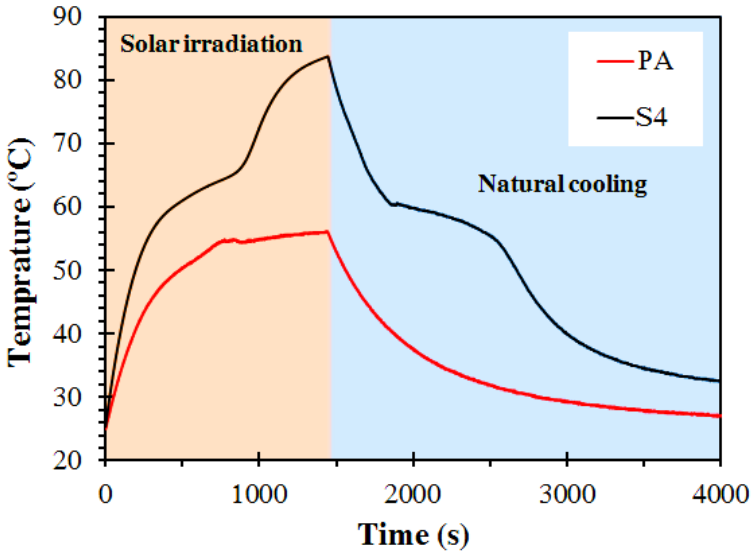

Figure 4-54: Temperature–time relationship of PA and PA/RGO samples under solar radiation

4.5.9 Thermal conductivity and Electrical Resistivity

As the interfacial resistance is inevitable upon the dispersion of fillers in the matrix and conjugated with a thick layer of PA, one feasible way to improve the thermal performance of SSPCMs is to use defect-free graphene with improved intrinsic thermal properties as fillers to form highly conductive networks for rapid heat transfer. Particularly, for carbonaceous materials, heat conduction is dominated by phonon transport from lattice vibrations of the covalent sp^2 bonding network (Ghosh et al., 2010). Figure 4-55 shows the variation tendency of thermal conductivities of PA/RGO SSPCMs prepared with different dosage of RGO. From the graph, we can see that thermal conductivities increased rapidly when the GO was added. There was nearly linear

correlation between the thermal conductivity and the dosage of RGO. That is to say, the more the dosage of RGO was, the higher the thermal conductivity of composites was. However, as is said above, the phase change enthalpy would constantly decrease with the increased amount of RGO. It is acknowledged that if the thermal conductivity of composites can reach 0.3 W/m K, it can meet the demand of heat exchange in the energy storage systems (Zalba et al., 2003).

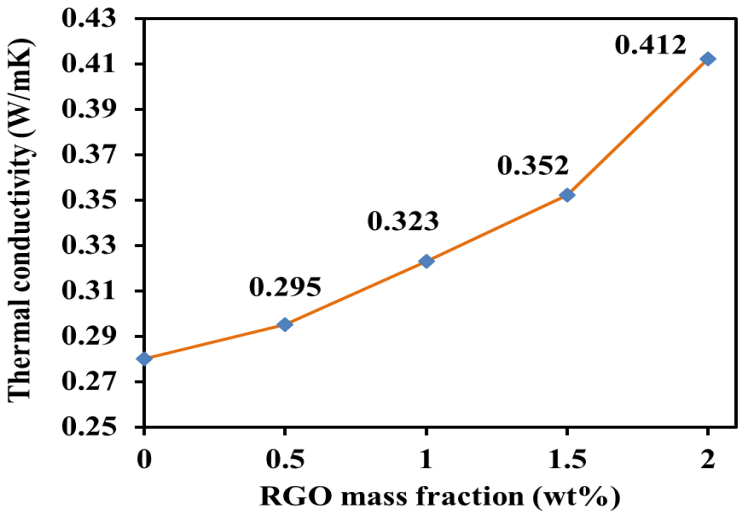

Figure 4-55: Thermal conductivity of PA and PA/RGO composite PCMs at 35 ℃

After phase change, the SSPCMs were heated continuously until steady state approached at 130°C and then was cooled down to the room temperature in the same condition. Temperature reduction can also be directly seen in the infrared camera images represented by the color after 20 sec for all SSPCMs (Figure 4-56). As time increased, the rate of temperature drop in the SSPCMs with higher mass ratio of RGO was much higher than others. Initially, a large (~20 °C) temperature difference exists between S4 and S1, represented by the dramatic color difference on the infrared camera image. The faster cooling rate is essential for the SSPCMs to release stored thermal energy at a rate high enough for effective thermal management.

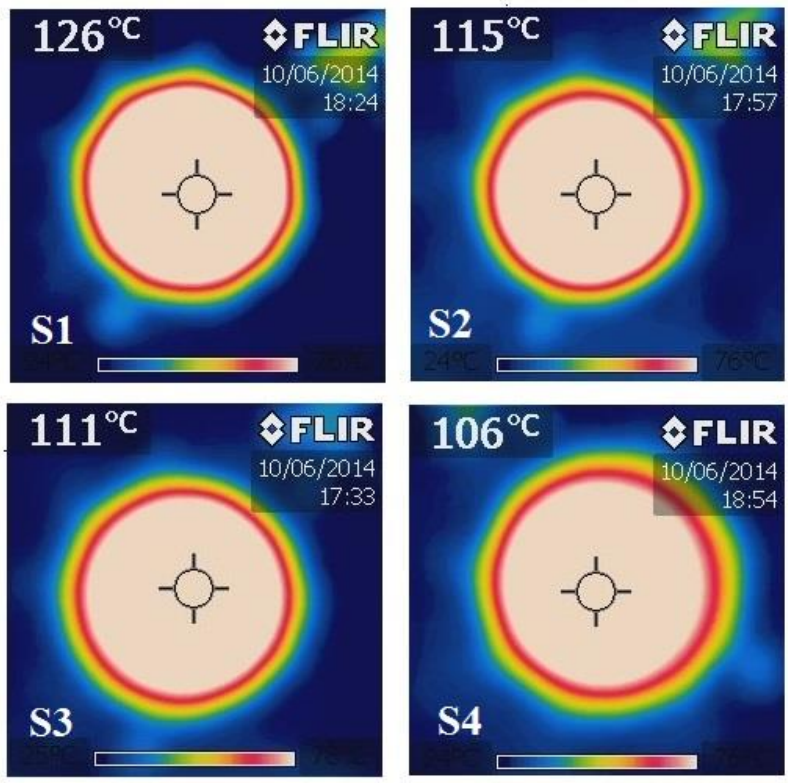

Figure 4-56: IR thermal images of the PA/RGO SSPCMs during cooling time

The electrical resistivity curve was plotted to evaluate the effect of RGO nanosheets on improving the electrical conductivity of the SSPCMs as shown in Figure 4-57. It turned out that by increasing RGO mass fraction inside the composites, the resistivity of samples reduced from 9.66×10^5 Ω.m for S1 to 0.83×10^5 Ω .m for 2 wt% PA/RGO composite. A percolation threshold between 0.5 and 1 wt% is observed for PA/RGO PCMs, where a huge decrease in resistivity occurs. The extremely high aspect ratio of RGO sheets drastically increases the chance of contacts between neighboring flakes and thus increases the probability of forming percolating networks at a lower loading content.

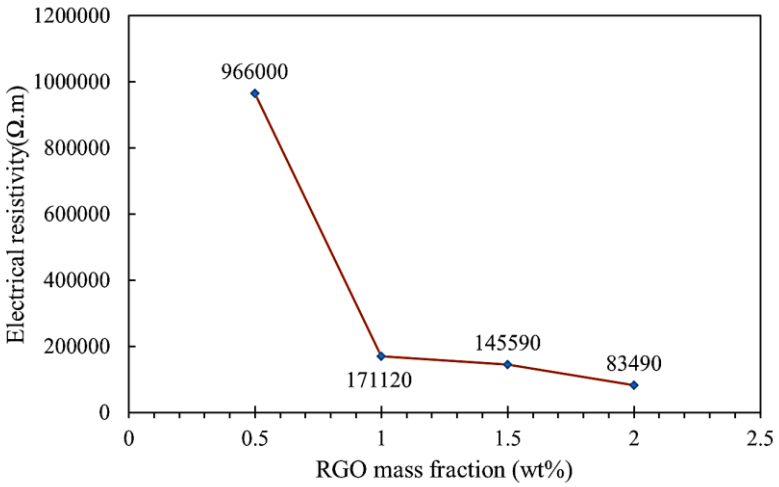

Figure 4-57: Electrical resistivity of PA/RGO composites

4.5.10 Thermal Reliability

Phase transition properties of prepared composites before and after 1000 thermal cycles are listed in Table 4-17. The DSC curves of the composites after thermal cycling had one transition peak which in agreement with the corresponding samples before cycling. Unlike most of the literatures which the latent heats remain unchanged after cycling, the phase change enthalpy was increased by 0.8, 1.1, 2.08 and 2.41 (kJ/kg) for S1, S2, S3 and S4, respectively. Moreover, their phase change temperatures were decreased by 0.6, 0.9, 1.5 and 1.4 °C. This phenomenon can be explained by investigating the chemical structure of PA in the composites after thermal cycling.

Table 4-17: Thermal energy storage properties after thermal cycling

Samples	Melting	
	T_{pm} (°C)	ΔH_m(kJ/kg)
S1	63.08	201.02
S2	62.85	200.36
S3	63.04	199.41
S4	62.40	199.34

Comparing the FTIR spectra after cycling in Figure 4-58 shows that no thermal degradation of PA occurred during heating and cooling cycles.

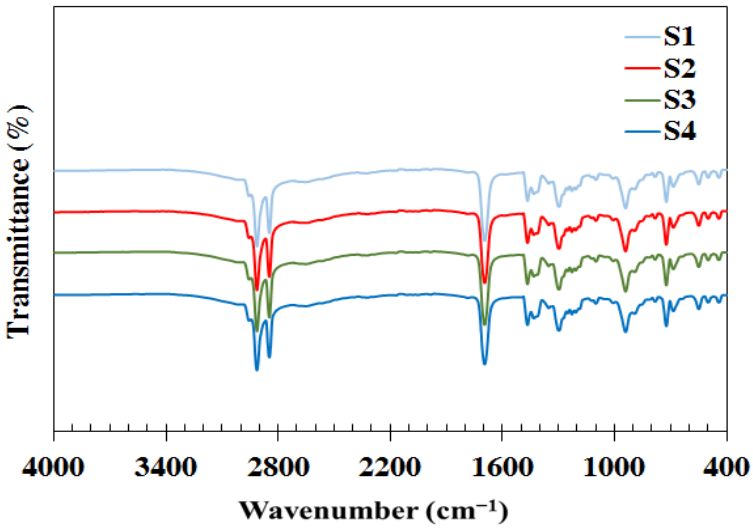

Figure 4-58: FT-IR spectra of SSPCMs after thermal cycling

The absorbance peak for -NH bending vibration around 1580 cm^{-1} is disappeared after thermal cycling. Based on these results, may be during cycling the $–NH_2$ functional group is removed from the reacted PA and interacted with the remaining carboxylic and epoxy functional groups of RGO. Therefore, PA regains its storage capacity and the percentage of the crystalized PA also increases which leads to the higher phase change enthalpy.

4.6 Carbon Nanospheres (CNSs) SSPCM

New carbon-based nanomaterials having highly curved graphitic structures, possessing properly-developed crystalline structures, substantial electrical conductivity, great thermal stability and sufficient oxidation resistance are remarkably attractive for any applications. Graphene materials have drawn much interest because of their exclusive structural, mechanical, thermal and electronic properties and consequently their particular potential use in the industrial products. However, the volume of graphene production is still limited, as well as the cost is considerably higher than that of porous carbon materials.

Therefore, in this research other SSPCMs were prepared as well as graphene composites to compare their energy storage properties.

4.6.1 Characterization of Carbon Nanospheres (CNSs)

Chemical characterization of the CNSs was carried out by FT-IR spectroscopy as shown in Figure 4-59.

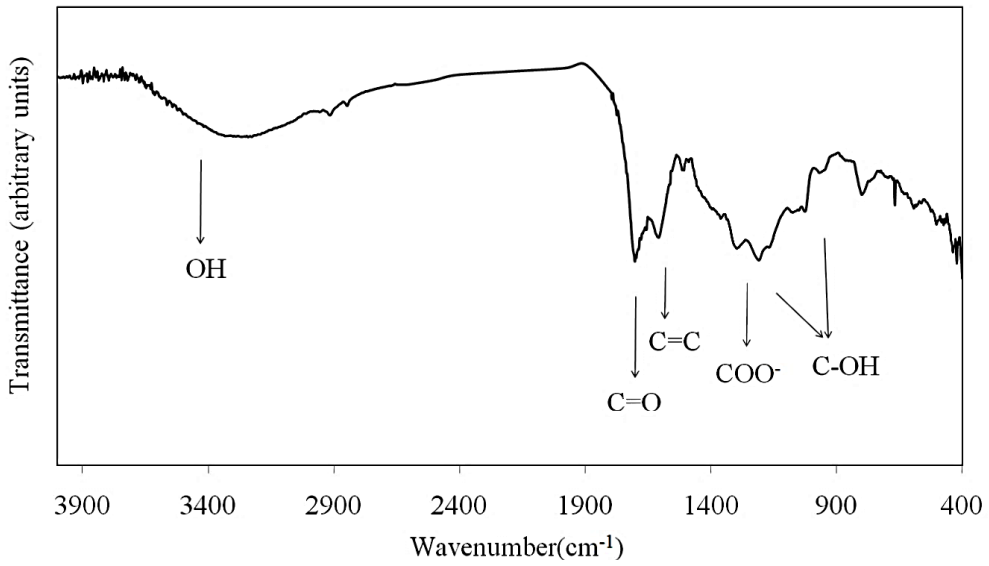

Figure 4-59: FT-IR spectrum of carbon nanospheres (CNSs)

The main absorption band is seen at 3350 cm^{-1} and assigned to O-H group stretching vibrations, 1735 cm^{-1} assigned to C=O stretching of carboxylic and/or carbonyl moiety functional groups, 1620 cm^{-1} to C=C stretching, 2823 cm^{-1} to aliphatic hydrocarbon–CH, 1033 cm^{-1} and 1320 cm^{-1} to C–OH stretching and OH bending vibrations in C–OH, 1361 cm^{-1} to symmetric stretching vibration of the deprotonated carboxyl group $–COO^{-}$, respectively (Song et al., 2011). Fabricated CNSs had a relatively narrow particle size distribution with a median particle diameter of 390.7 nm (90% of the nanospheres distributed from 100 to 450 nm) (Figure 4-60(a)). CNSs had spherical shapes and rough surfaces and specific surface area of CNSs was obtained of 212m^2/g by BET test using nitrogen gas and a pore size diagram of CNSs as shown in Figure 4-60(b).

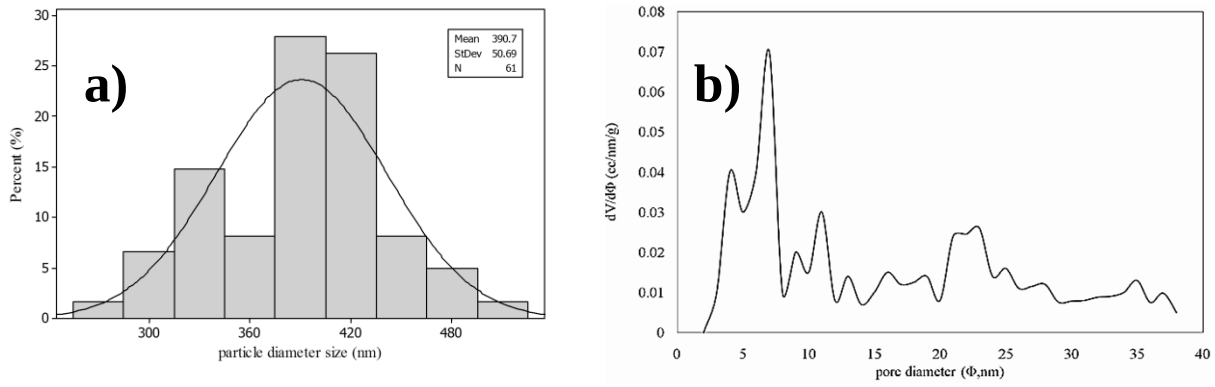

Figure 4-60: a) Particle size distribution b) Pore size distribution curve of CNSs

From Figure 4-60(b), the pore-size distribution is primarily between 3 and 40 nm, further verifying the diversity of the pore-size distribution of the CNSs.Transmission electron microscopy (TEM) was used for observing the large quantity of pores that are homogeneously dispersed within the carbon matrix (Figure 4-61). These results indicated that prepared CNSs have very high specific surface area and porosity to be used as supporting material in composite phase change materials.

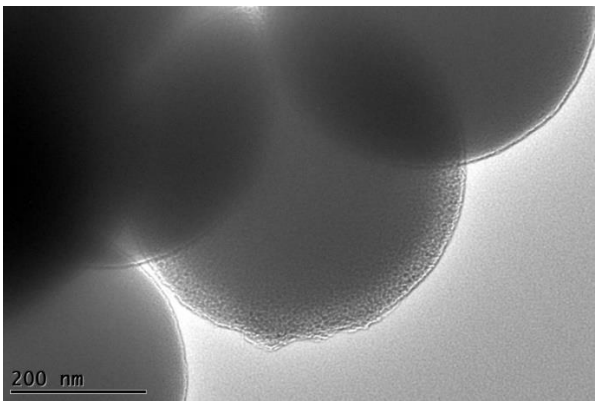

Figure 4-61: TEM image of CNSs

4.6.2 Characterization of the SA/CNSs SSPCM

Figure 4-62 indicates FT-IR spectra of the SA, CNSs and SA/CNSs form-stable PCMs. The bonds at 2915.04 and 2849.43 cm^{-1} are the symmetrical stretching vibration peaks of $–CH_2$ in SA. The peak at 1713 cm^{-1} is the characteristic absorption peak for the stretching vibration of the carbonyl group. The peak at 1470 cm^{-1} is the $–CH_2$ bending

peak, 1415 cm^{-1} represents C-H and C-C bending, 742 cm^{-1} and 723 cm^{-1} corresponds to rocking vibration and bending, which are all characteristics for an aliphatic chain of SA. It is apparent that the FT-IR spectra of PCM1 possesses all primary absorption peaks of the SA without any changes which is suggesting there is absolutely no chemical reaction among functional groups of the SA and CNSs.

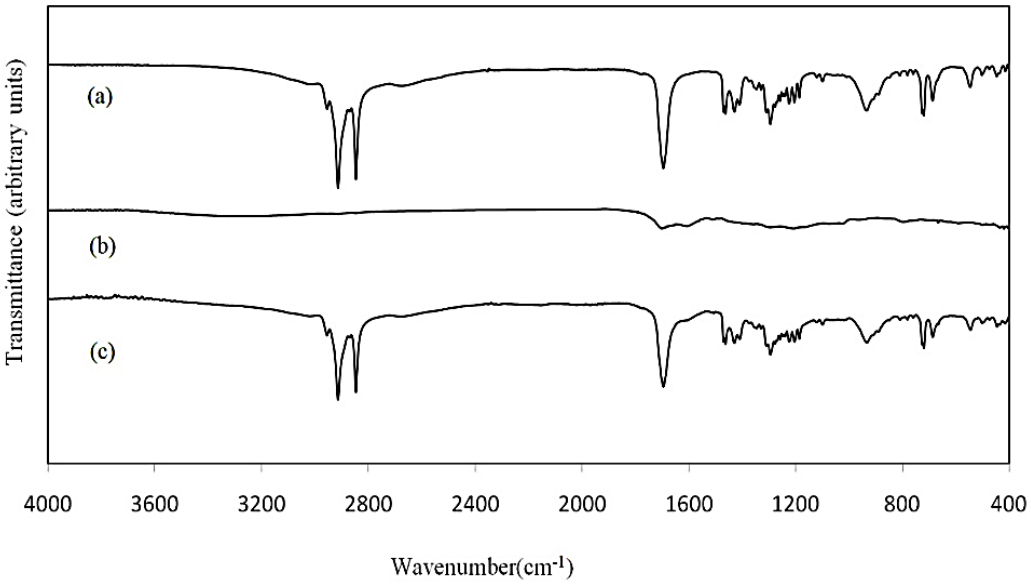

Figure 4-62: FT-IR spectra of (a) SA (b) CNSs (c) SA/CNSs composite PCM

4.6.3 Morphology of the Composites

Figure 4-63 shows the FESEM images of the CNSs and SA/CNSs PCMs with a different mass percentage of CNSs loaded to SA. Figure 4 63 (a) shows homogeneous carbon nanospheres (CNSs) that were prepared by hydrothermal method.

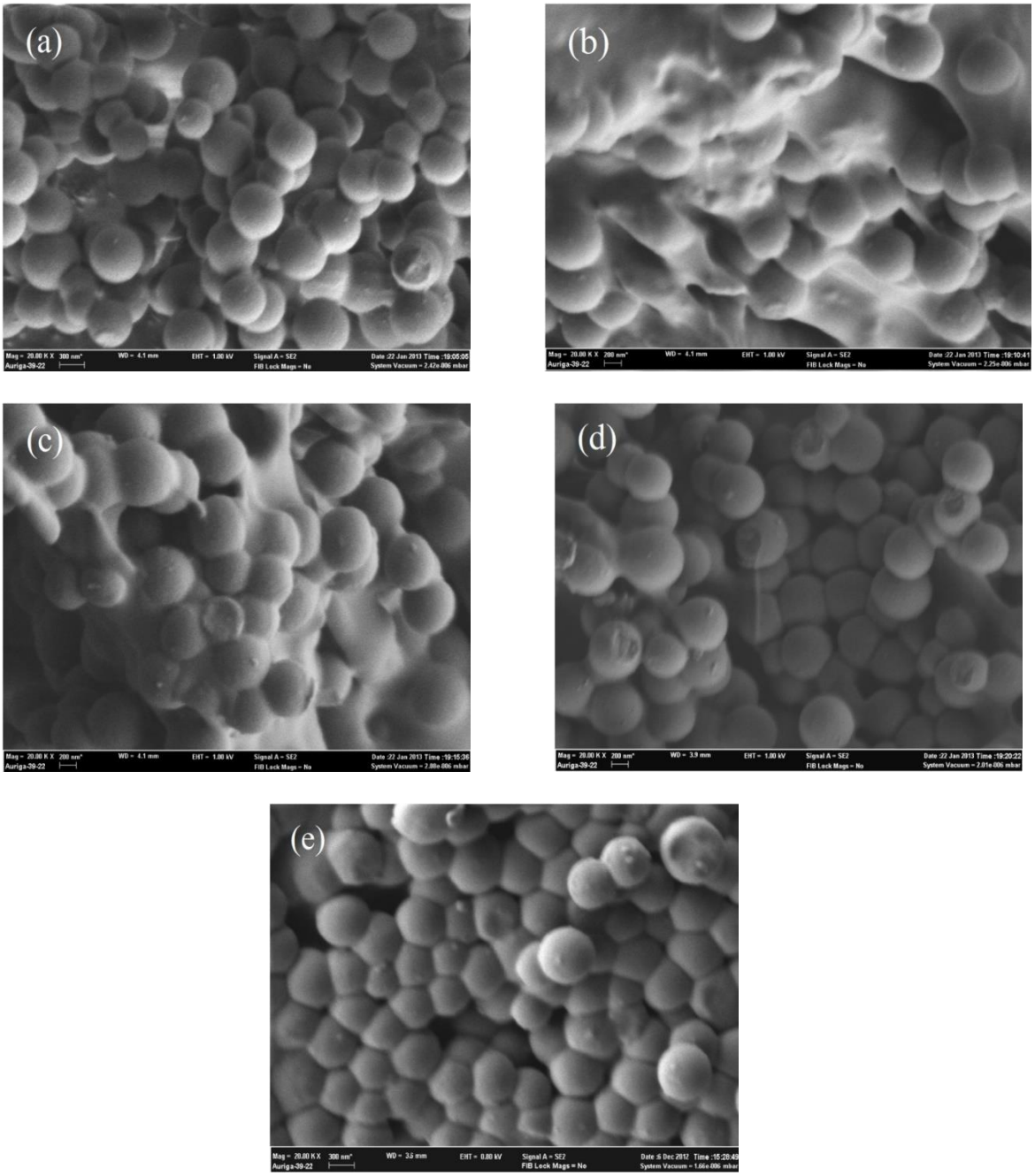

Figure 4-63: SEM images of (a) CNSs (b) PCM1 (c) PCM 2 (d) PCM 3 (e) PCM 4

In Figure 4-63(b) and (c) white areas were observed, as the inordinate SA which was not completely absorbed by CNSs. Figure 4-63(d) and (e) indicate that SA was completely absorbed into the spaces between CNSs, hence the considerable effects on the shape stabilization of composite PCMs. An important factor to increase the impregnation ratio of SA in the composite PCMs is the specific surface area (BET) of supporting material. The specific surface area of prepared CNSs is 212 m^2/g that much higher than

previous supporting materials used in the composite PCMs such as expandable graphite, carbon black and others (Chen et al., 2012; Sarı & Karaipekli, 2009). Therefore, SA will be simply held by the surface tension and it will avoid leakage of SA from composite PCM. The SA/CNSs composite PCM powder that was prepared is shown in Figure 4-64.

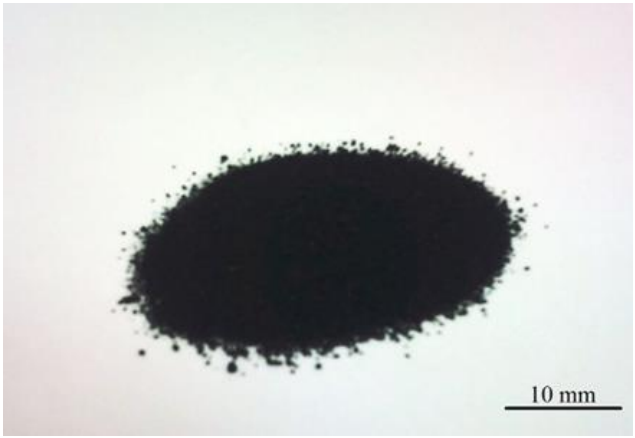

Figure 4-64: The SA/CNSs composite PCM

4.6.4 Thermal properties of SA/CNSs SSPCMs

A differential scanning calorimetry (DSC) analysis was used to evaluate the phase change behavior of the composites after thermal treatment at 80℃ for 1h. Figure 4-65 andFigure 4-66 show the DSC curves for melting and solidification process of SA and composite PCMs.

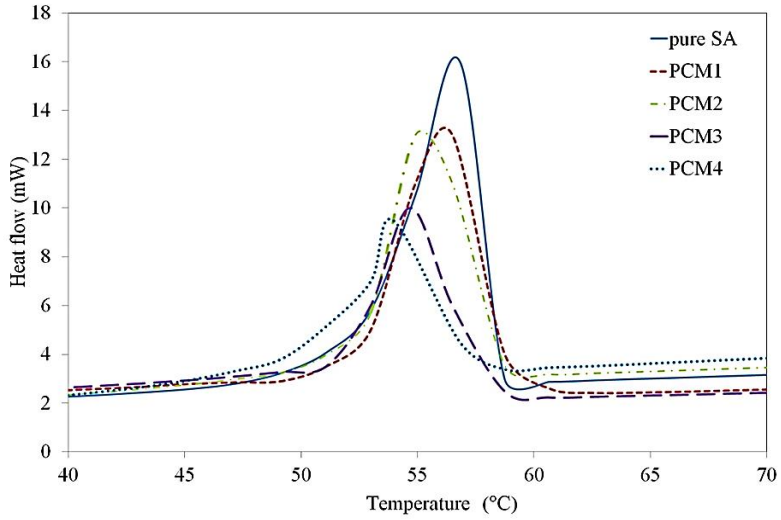

Figure 4-65: Melting DSC curves of SA and PCM1–PCM4.

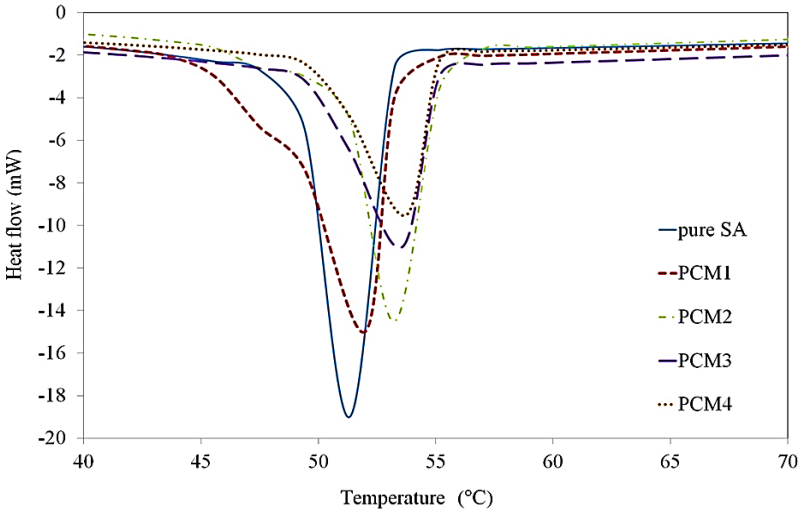

Figure 4-66: Solidifying DSC curves of SA and PCM1–PCM4.

Table 4-18 gives a summary of the characteristic phase change temperatures and the enthalpy calculated based on the heat flow measured during the test. The phase change temperatures of SA and composite PCMs were closed while the melting temperatures were decreased and freezing temperatures were increased in composite PCMs. The results show that the highest subcooling was 5.5℃ for the pure SA and decreased to 0.2℃ for PCM4. As a result, the melting points of the SA/CNSs composite PCMs are almost identical to its solidification point, indicating that negligible subcooling occurs in the composite PCMs. However, compared with pure SA, lower phase change temperatures for all the composites could possibly be due to the interactions between SA and the inner surface of the CNSs and due to the confinement of SA in fine pores. Moreover, SA has a large latent heat of more than 180 kJ/kg, specifically, 184.3 kJ/kg for melting and 189.2 kJ/kg for solidification (on average). The small difference in latent heat between melting and solidification may originate from the low extent of subcooling inherent in SA. For a SA/CNSs composite PCMs, the content of SA will affect its latent heat and the content of CNSs will affect its thermal conductivity. Moreover, the absorption capacity of the CNSs is limited. Therefore, it is necessary to determine the optimum mass ratio of SA to CNSs. As it can be seen in Table 4-18 , the relative errors were calculated for composite

PCMs and results indicated that the highest error was belonged to PCM1 due to the leakage of molten SA had not been absorbed by CNSs during the thermal treatment. The relative errors for PCM2, PCM3 and PCM4 were less than 2% that are negligible for thermal energy storage applications.

Table 4-18: Thermal properties of SA and SA/CNSs SSPCMs

Sample name	SA loading (wt %)	Melting				Solidification	
		T_m (°C)	ΔH_m (kJ/kg)	Calculated value ΔH_{mc} (kJ/kg)[a]	Relative Error (%)[b]	T_f (°C)	ΔH_f (kJ/kg)
SA	100	56.8	184.3	-----	-----	51.3	189.2
PCM 1	89	56.5	152.5	164.02	7.02	52	154.3
PCM 2	80	54.9	145.3	147.44	1.45	53.2	146.2
PCM 3	67	54.7	122.2	123.48	0.97	53.6	122.8
PCM 4	50	53.9	91.8	92.15	0.38	53.7	92.1

Melting temperature : T_m(°C) Freezing temperature : T_f(°C)

Melting latent heat : ΔH_m(kJ/kg) Freezing latent heat : ΔH_f(kJ/kg)

[a] $\Delta H_{mc} = SA(wt\%) \times \Delta H_{SA}$

[b] Relative Error (%) = $\frac{\Delta H_{mc} - \Delta H_m}{\Delta H_{mc}} \times 100$

The CNSs with high and uniform porous structure was capable to minimize seepage of the molten SA that will improve the latent heat of the composite PCMs. Here the PCM1 sample shows the highest latent heat value without any leakage after thermal treatment, which was 82.7% of pure SA.

4.6.5 Dropping Point

Employing high porous materials can solve these problems and may even affect the thermal conductivity of the PCMs depending on the additives that has been utilized. The dropping point of pure SA was 58℃ and was increased significantly with the addition

of CNSs particles as shown in Table 4-19. The capillary and surface tension forces between SA and CNSs may result in a great enhancement in the shape stabilization of the composite PCMs. It can be mentioned that even at a CNSs content of 20 wt%, the shape of the composite can be preserved up to 152.4 ℃, considerably higher than the utilizing temperature range of energy storage systems.

Table 4-19: Shape-stabilized temperatures of the composite PCMs

Sample	Dropping point (℃)
SA	58
PCM 1	90.1
PCM 2	152.4
PCM 3	180.2
PCM 4	250

4.6.6 Thermal Stability

Figure 4-67 shows the TGA curves of SA and the prepared form-stable PCMs. The onset and maximum weight loss temperatures are given in Table 4-20. SA exhibits a one-step weight loss starting at 181.43℃ and the maximum weight loss temperatures at 245.20℃, which is caused by the evaporation of SA.

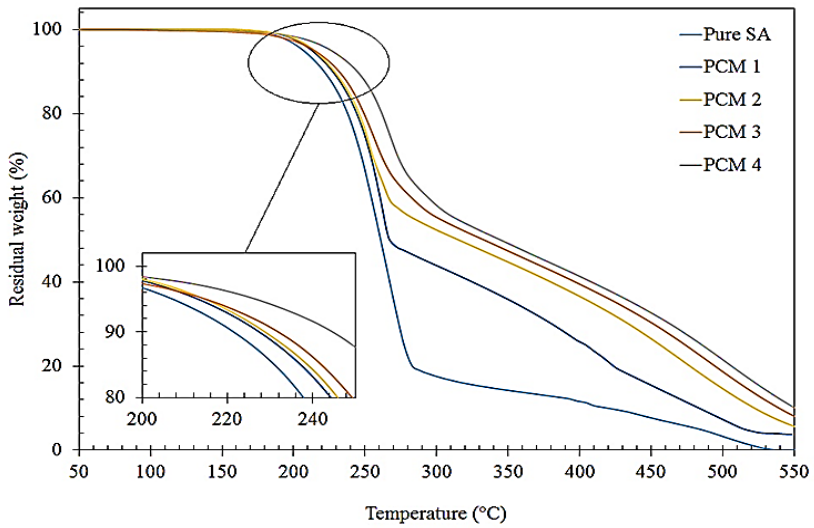

Figure 4-67: TGA curves of the pure SA and PCM1–PCM 4

It is reasonable to believe that SA must first break through the CNSs pores during the heating process and then can evaporate out of the composite. The CNSs particles are compact and rigid enough to protect the absorbed SA from diffusing at the normal boiling point, thus improving the degradation temperature of composite PCMs. The results were listed in Table 4-20 also confirm that the maximum weight loss occurs at a higher temperature for the composite PCMs with a higher content of CNSs. There is no doubt that the composite PCMs achieved higher stability by adding CNSs as a supporting material.

Table 4-20: Decomposition temperatures of the SA and composite PCMs

Sample	Onset decomposition temperature (℃)	Maximum weight loss temperature (℃)
Pure SA	181.4	245.2
PCM 1	187.2	247.7
PCM 2	188.8	248.5
PCM 3	189	250.4
PCM 4	194.1	253.1

4.6.7 Thermal Conductivity

SA has a high latent heat, but a low thermal conductivity that may delay the thermal response to the storage and release of latent heat. Therefore, thermal conductivity enhancement is absolutely required when designing composite PCMs. The thermal conductivity of SA and SA/CNSs composite PCMs are measured at 35 ℃ and results are shown in Table 4-21.

Table 4-21 : Thermal conductivity of SA and SA/CNSs composite PCMs at 35 ℃

Samples	Thermal conductivity(W/m.K)
Pure SA	0.21
PCM 1	0.301
PCM 2	0.381
PCM 3	0.415
PCM 4	0.431

From the data presented in Table 4-21, it can be seen that the thermal conductivities of the SA/CNSs composites clearly improved compared to the pure SA. The maximum enhancement was 105.2% by adding 50 wt% of CNSs and it shows that CNSs has a desirable effect on the thermal conductivity of SA. However, the results also indicated that the thermal conductivity does not increase linearly with increasing CNSs loading. It was suggested that the arrangement of the particle structures in CNSs influences the interaction between SA and CNSs. By comparing PCM1 with PCM2, it can be seen that the enhancement was more due to the virtual heat transfer network made by CNSs particles. At the high CNSs loading, as the content of CNSs is further increased, the increasing of thermal conductivity slows down and exhibits a tendency to approach a limit. As a result, the SA/CNSs composite PCMs achieved a higher thermal conductivity than pure SA.

4.6.8 Thermal Reliability

The SA/CNSs composite PCMs were examined after get exposed to 1000 melting-freezing cycles. The changes of latent heats in composite PCMs following cycling process were considered to determine whether they are thermally reliable.

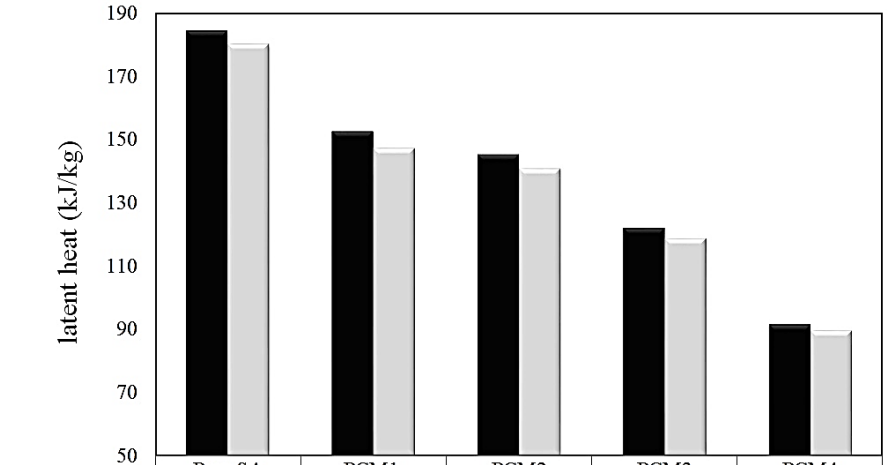

	Pure SA	PCM1	PCM2	PCM3	PCM4
Before cycling	184.3	152.5	145.3	122.2	91.8
After cycling	180.26	147.35	140.85	118.8	89.68

Figure 4-68: The latent heats value of the PCMs before and after 1000 cycles

The composite PCMs had only one phase transition curve with particular onset temperatures as before the cycling. In other words, there were clearly no extra peaks related to chemical disintegration or phase detachment within the composites. Through comparing the latent heat values in Figure 4-68, the maximum change in latent heat capacity was determined as 5.15 kJ/kg for PCM 1 and the minimum was 2.12 kJ/kg for PCM 4 while this value was 4.04 kJ/kg. These results suggested that the changes in the latent heat capacity of the composites after thermal cycling were less than pure SA for PCM2, PCM 3 and PCM4 demonstrate their good thermal reliability. The results indicate that the PCM1 had some leakage during cycling that caused effects on the latent heat capacity of the composites. The thermal cycling results show that the shape stabilization of SA was achieved by adding only 20 wt% of CNSs and there was no leakage of SA after the exposure to 1000 melting-freezing cycles.

4.7 Activated Carbon (AC) SSPCM

In the last decade, development of biomass-based porous carbon materials has become probably the most active areas in the carbon materials science owning to their

exclusive features such as sustainability, environmental friendliness, and continuous accessibility. Up to now, there are few reports about activated carbon SSPCMs and they used commercial products with low porosity (Chen et al., 2012). In our research, ultrahigh specific surface area activated carbon with larger pore volume was synthesized by using rice hull as a biomass-based material. In this study GNPs were used to improve thermal conduction of granular activated carbon and achieve higher thermal conductivity for PA/AC SSPCMs. Additions of GNPs from 1 to 6 wt% were considered to be suitable for thermal conductivity enhancement.

4.7.1 Characterization of Activated Carbon (AC)

In contrast with several earlier reports in which activated carbon with good specific surface area and narrow micro-pore distribution were synthesized by using KOH and carbonaceous precursors such as coals, chars and others (Lillo-Ródenas et al., 2003). We employed chemical activation with NaOH to efficiently produce the AC with ultrahigh specific surface area and enormous pore volumes from rice hull. The suggested procedure is written as follows (Qie et al., 2013):

$$6NaOH+2C\rightarrow 2Na+3H_2+2Na_2CO_3 \quad (4\text{-}4)$$

$$Na_2CO_3+C\rightarrow Na_2O+CO_2 \quad (4\text{-}5)$$

$$2Na+CO_2\rightarrow Na_2O+2CO \quad (4\text{-}6)$$

$$2NaOH+SiO_2\rightarrow Na_2SiO_3+H_2O \quad (4\text{-}7)$$

$$Na_2O+SiO_2\rightarrow Na_2SiO_3 \quad (4\text{-}8)$$

Particularly, the NaOH activation leads to porosity improvement and an increase in surface area, as well as additional advantage that will be the formation of – OH surface functional groups on the carbon surface. Furthermore, through the activation procedure, the silica within the rice hull will react with some sodium hydroxide to make stable sodium silicate salt.

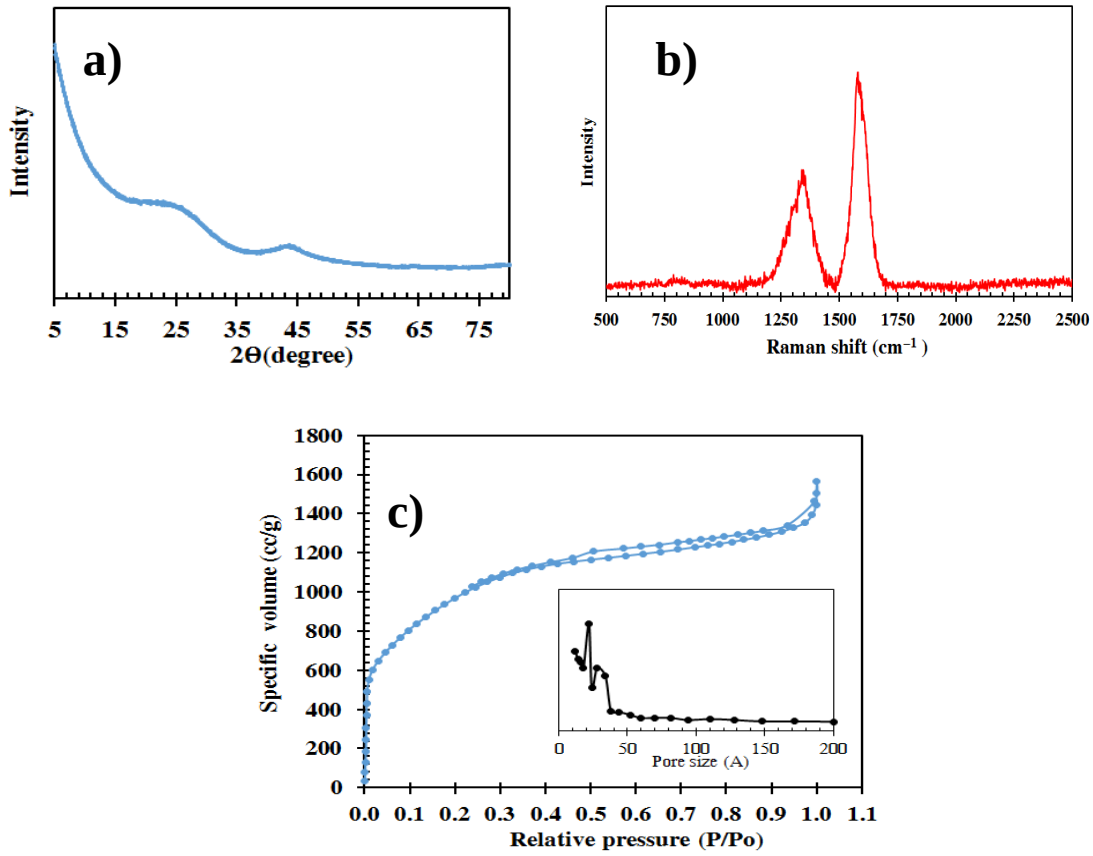

Figure 4-69: (a) XRD (b) Raman spectra (c) Nitrogen adsorption/desorption isotherms of AC. Inset in (c) is the BJH pore size distribution

Figure 4-69(a) demonstrates the common XRD pattern of the activated carbon (AC). Two wide peaks were seen at angle of 24° and 44°, that correspond to the (002) and (100) planes, respectively. The amorphous behavior of activated carbon is discovered (Lv et al., 2012). In addition, no impurity diffractions were discovered, verifying the elimination of primarily inorganic impurities by activation procedure and acid washing. Figure 4-69(b) displays the Raman spectrum of AC which has two obvious peaks at 1341 and 1588 cm^{-1}, that match the D and G bands of disordered and graphitic carbons, respectively. The D and G band ratio of AC (I_{1341}/I_{1588}) was 0.67, indicating the amorphous carbon structure along with a large content of lattice edges or plane defects of AC. The N_2 adsorption-desorption isotherms along with the pore size distribution of the AC material are shown in Figure 4-69(c). Comparable to previous reports, strong N_2 adsorption was seen, that verifies the existence of various pore sizes of micro-, meso- and

macropores (Qie et al., 2013). A surface area of 3900(m^2/g) was determined using the Brunauer-Emmett-Teller (BET) model. The SEM images from Figure 4-70 shows that the AC is extremely porous sample with rough surface areas. The existence of these consistent mesoporous perforation like structures on the surface are mostly responsible for the PCM adsorption onto the AC surface.

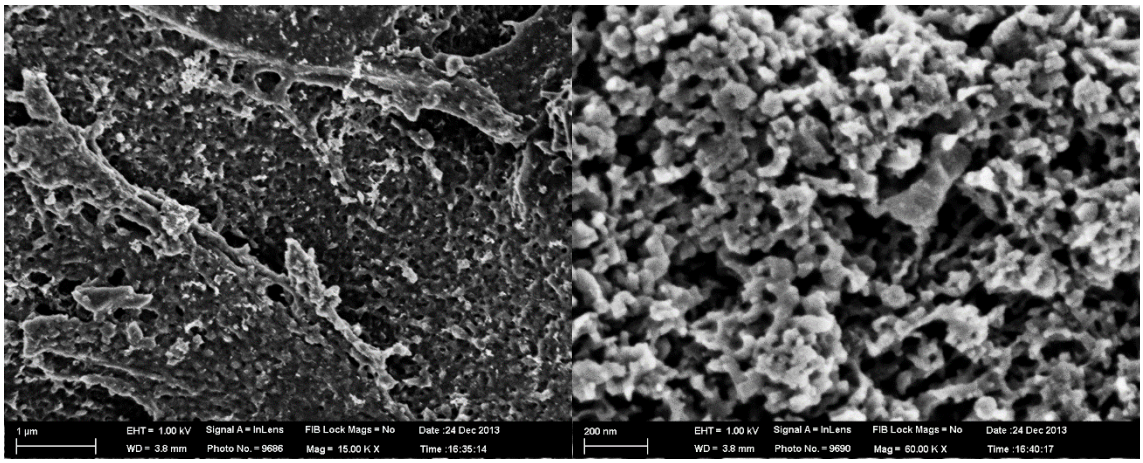

Figure 4-70: SEM images of the prepared AC

4.7.2 Morphology of PA/AC SSPCMs

Figure 4-71 shows the SEM images of S1 to S5. In the images, the white areas represented PA. As shown in Figure 4-71(a), the activated carbon has multiple pores with plenty of internal surfaces that allows those to be simply saturated with the melted PA.

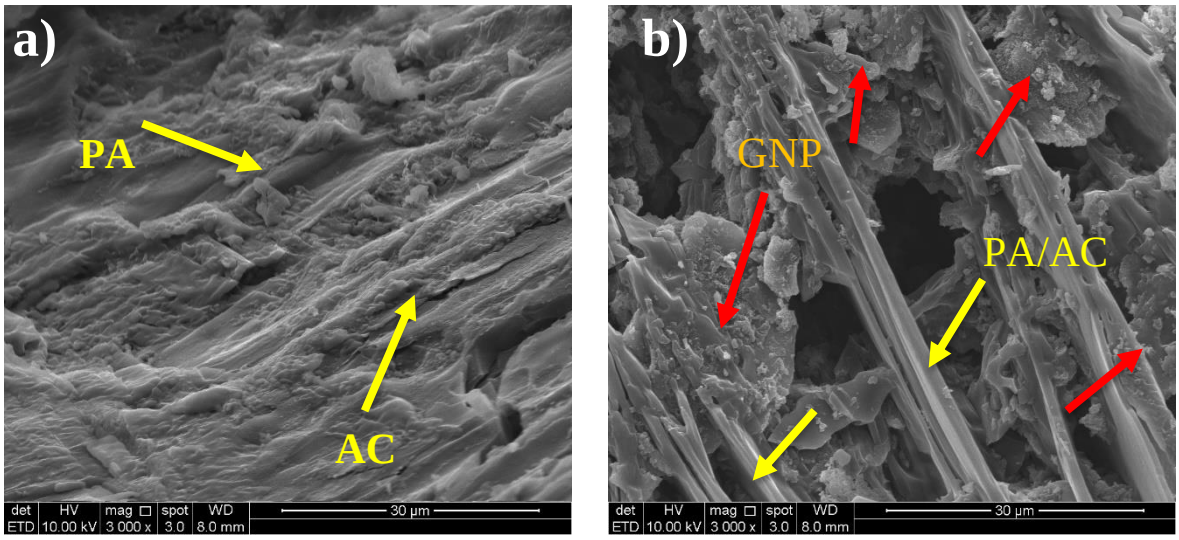

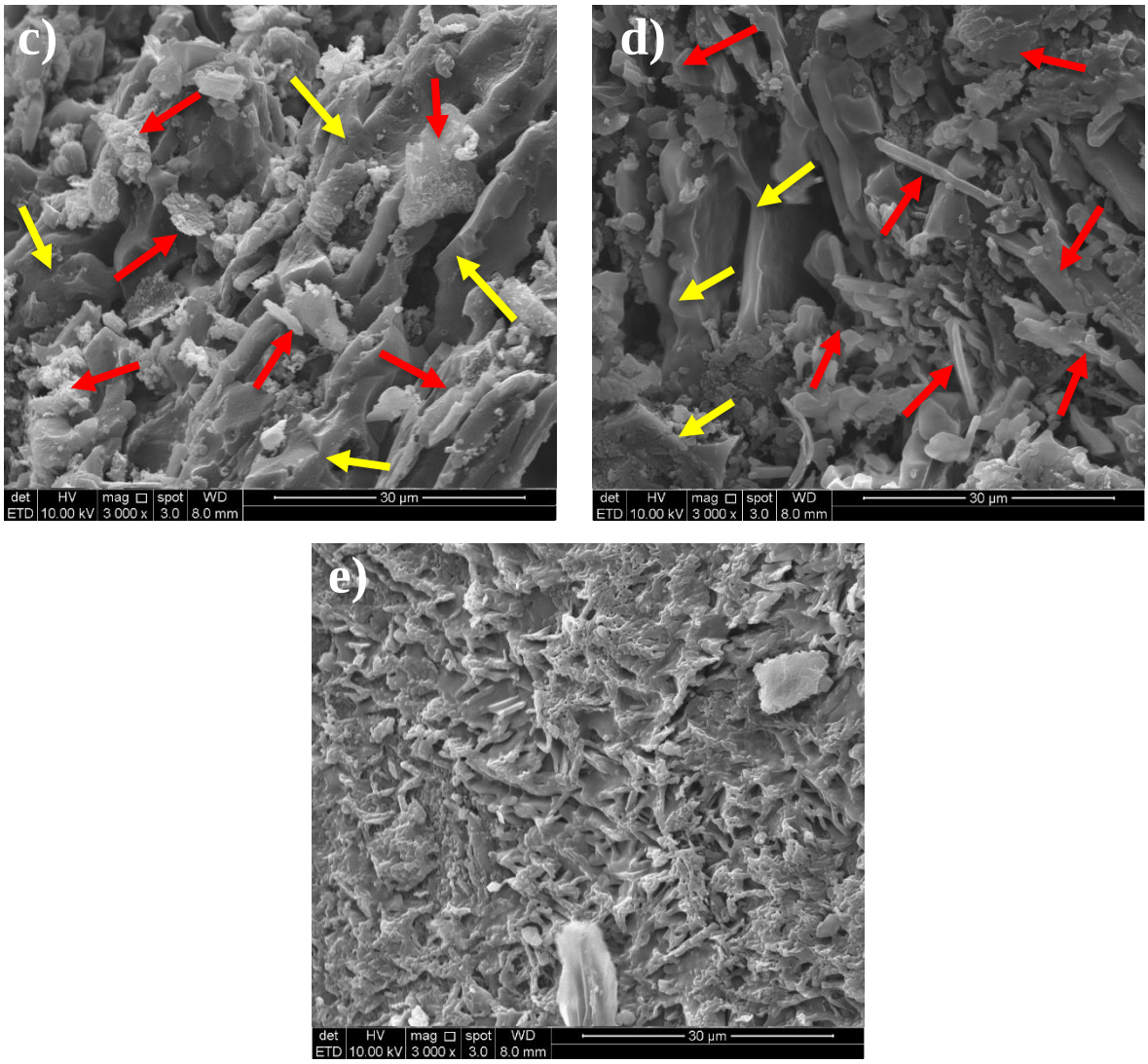

Figure 4-71: SEM images of (a) S1(b) S2 (c) S3 (d) S4 and (e) S5

It can be noticed from the fracture surface of the PA/AC composite that AC network is covered by PA as well as the porous space is almost completely filled up. These micro and nano scale pores of AC collectively draw in PA (as a result of the capillary effect) preventing it from leaking out during melting process. As observed in Figure 4-71(b-e), the GNPs with various mass percentages (1, 2, 4 and 6 wt%) inside the PA/AC composites was adsorbed and distributed in the porous network of the activated carbon. The yellow arrows show the PA/AC network and red arrows show the distribution of GNPs nanosheets in composite PCM. It can be indicated from SEM images that GNPs nanosheets were dispersed homogeneously in PA/AC composite. Figure 4-71(e) shows that the PA/AC network was entirely covered by GNPs nanosheets and provided different morphology.

4.7.3 FT-IR analysis

FT-IR spectra of PA, PA/AC as well as the prepared PA/AC/GNPs form-stable PCMs are represented in Figure 4-72. It can be evidently noticed that all absorption peaks of the primary functional groups of PA can be found in the spectra of the PA/AC SSPCMs with merely a slight shift. No major new absorption peaks took place in the spectra of PA/AC/GNPs composites compared with pure PA, indicating that simply no new chemical bonds generated between PA and the matrix. These results indicate that there should not be significant changes in energy storage properties of composite PCMs during the melting and solidification process.

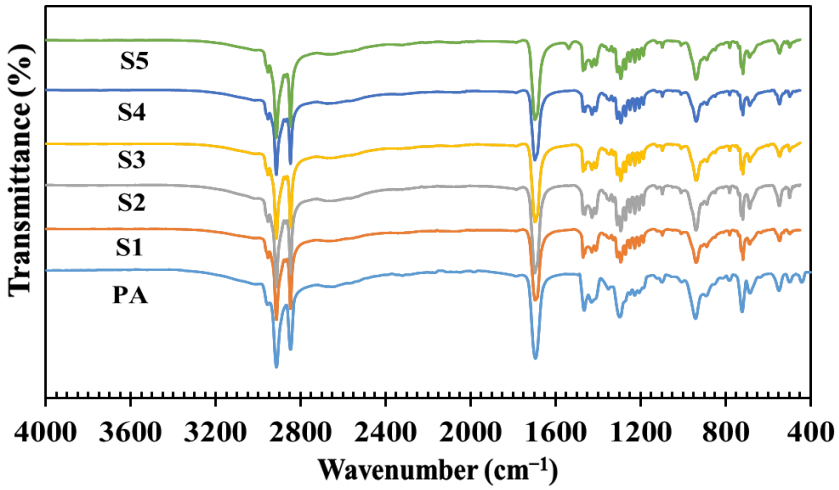

Figure 4-72: FT-IR spectra of PA, PA/AC and PA/AC/GNPs composites

4.7.4 Energy Storage Properties

Figure 4-73 displays the DSC curves of the PA/AC PCMs with different GNPs weight ratio. As found in Table 4-22, the melting point of the PA/AC PCMs was decreased compared to pure PA. The phase transition enthalpy decreased with the reduction in PA weight percentages.

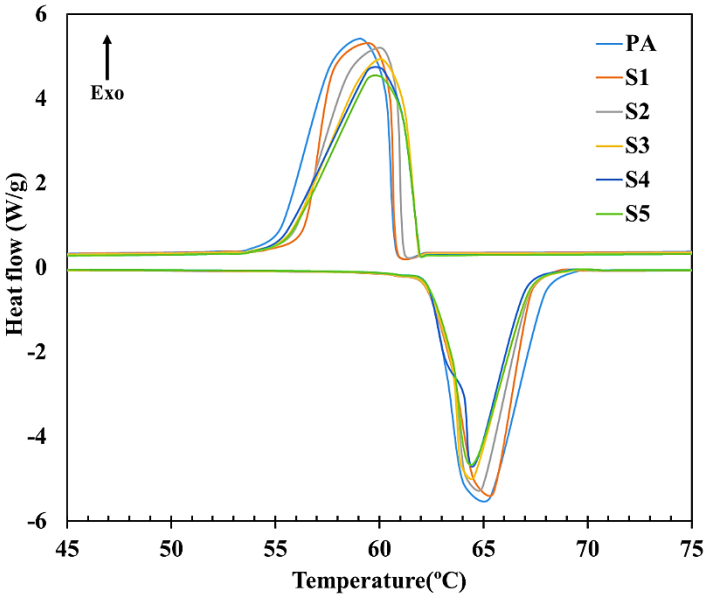

Figure 4-73: DSC curves of PA, PA/AC PCMs with various GNPs weight percentages

The melting and solidifying latent heats are measured to be 202.29 kJ/kg and 205.48 kJ/kg for the PA and 174.98 kJ/kg and 175.31kJ/kg for the S1, respectively. From the calculations, it can be indicated that 86.4 wt% of paraffin wax is loaded in the PA/AC composite and adsorbed by porous structure of the activated carbon while by adding 6wt% of GNPs this value is decreased to 82.63 wt%.The latent heat of melting for the S5 is almost the same as S4 while using higher mass ratio of GNPs. Therefore, it can be indicated that PA was also adsorbed by surface of GNPs as well due to the high specific surface area of GNPs that will help to increase the latent heat of melting and also increase the thermal conductivity.

Table 4-22: Phase transition temperature and enthalpy of PA/AC composite PCMs

Sample name	Palmitic acid (Wt %)	Melting		Solidification	
		Melting peak temperature T_{pm} (℃)	Melting latent heat ΔH_m(kJ/kg)	Freezing Peak temperature T_{pf} (℃)	Freezing latent heat ΔH_f(kJ/kg)
PA	100	65.34	202.29	59.16	205.48
S1	86.4	65.5	174.98	59.6	175.31
S2	85.84	64.95	173.65	60.12	174.29
S3	84.28	64.92	170.51	60.14	171.94
S4	82.76	64.6	167.43	60.15	169.32
S5	82.63	64.5	167.16	60.15	169.11

In realistic applications, the supercooling of PCMs should be considered. Using the DSC measurement leads to Figure 4-74, the level of supercooling was considered as the difference between the melting and solidification peak temperature. From Figure 4-74, we realize that the degree of supercooling in pure PA was larger compared to that in the PA/AC PCMs. This shows that the blending of mesoporous AC with pure PA will positively reduce the degree of supercooling in PCMs. Also it can be seen that by adding GNPs as a nanofliller, the level of supercooling reduced as well. These results indicated that both porous wall of AC and GNPs surface are acting as nucleation agent.

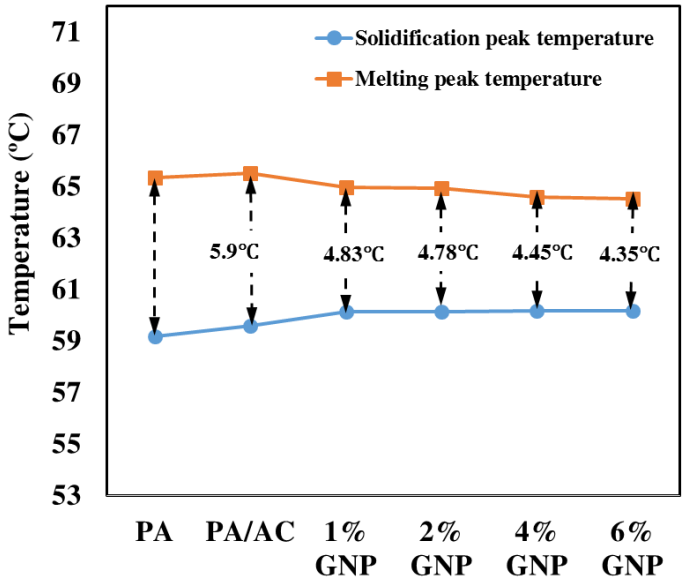

Figure 4-74: Extent of supercooling for PA/AC composites

4.7.5 Thermal Stability

The TGA and DTG curves of PA and S1-S5 are presented in Figure 4-75 (a) and (b), respectively. The charred residue amount at 450 °C as well as the temperature of maximum weight loss are shown in Table 4-23. As observed in Figure 4-75, there is one-step thermal degradation processes. The weight loss of the S1 is larger than those of the PCM1–PCM3 throughout one-step thermal degradation stage. This is simply because of the higher mass of PA inside the S1 compare to that inside S2-S5. As revealed in Figure 4-75, the initial step occurs at a temperature between 200 and 310 °C, related to the thermal degradation of PA molecular chains.

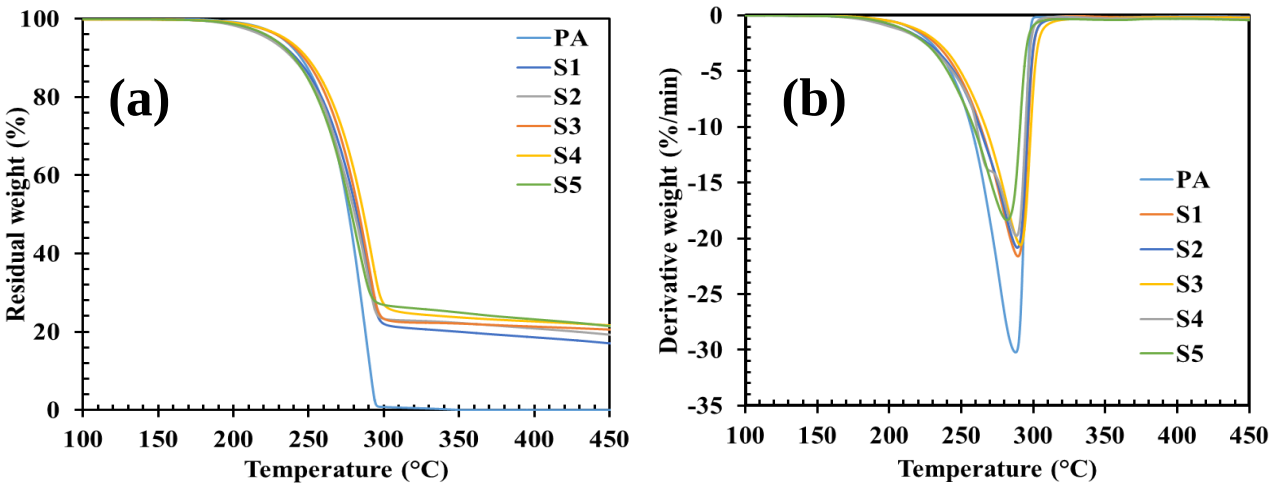

Figure 4-75 : (a) TGA and (b) DTG curves of PA/AC PCMs with various GNPs weight percentages

Consequently, the activated carbon is effective to create carbonaceous layers accumulating on the surface, which makes a physical safety barrier on top of the composites. This protective barrier can restrain the transfer of flammable molecules to the gas phase and the transfer of heat from the flame to the compacted phase. This result suggests that the activated carbon can enhance the thermal stability of the composites.

Table 4-23: TGA results of PA/AC composite PCMs

Sample	Maximum weight loss temperature (℃)	Charred residue amount (%) (450 ℃)
Pure PA	276.32	0
S1	289.12	16.32
S2	289.22	17.59
S3	289.74	18.67
S4	289.48	20.13
S5	278.48	20.85

4.7.6 Form-Stable Properties

The shape-stable property of the PA/AC composite PCMs were examined using hot stage at 91 °C. Shape changes were seen via images as shown in Figure 4-76 .The pure PA started to flow once the temperature reached to its melting point. But there was

clearly no seepage of PA from the surfaces of the composites even when the temperature was more than the melting point of PA. PA is a type of fatty acid that contain long-chains, and also the AC possess an intercross linked network. The capillary force and surface tension caused by the AC network minimal the seepage of liquid PA. As a result, the PA/AC SSPCMs preserve their initial shape after phase change process.

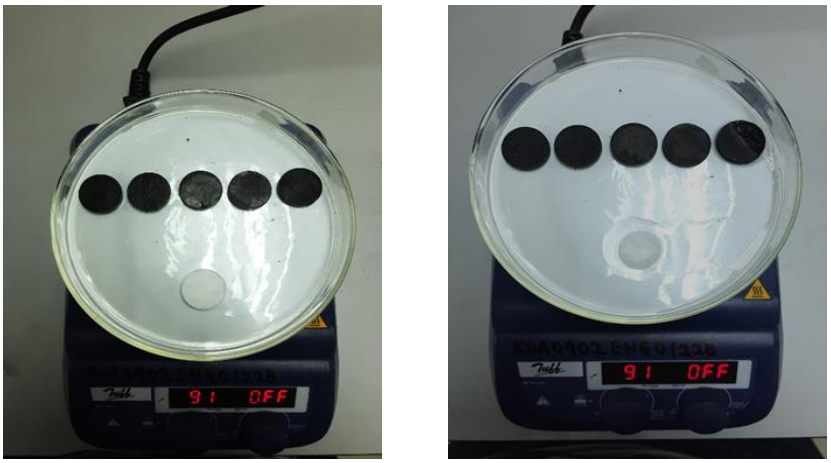

Figure 4-76: PA/AC composites with varying GNPs contents

4.7.7 Thermal conductivity and Thermal Imaging

Table 4-24 shows the thermal conductivity values for PA, PA/AC and SSPCMs loaded with different mass fractions of GNPs. The thermal conductivity of PA/AC composite was almost the same as pure PA and improved when GNPs was loaded into the system. Particularly, NaOH activation leads to porosity improvement. Increase in surface area and an additional effect is the formation of –OH surface functional groups on the carbon surface. The –ONa groups formed on the carbon surface after NaOH activation, which changed into –OH groups by ion exchange reaction once the samples were rinsed with water. Therefore, voids can be made when Na is eliminated, which makes a large number of polar functional groups, including –OH, which makes the carbon surface hydrophilic. These functional groups will affect the thermal conductivity of the activated carbon and for that reason there is not significant enhancement on thermal

conductivity of PA/AC composite. Thermal conductivity of the SSPCMs with 1, 2, 4, and 6 wt% GNPs reached 0.292, 0.334, 0.393 and 0.551 W (m K)$^{-1}$, respectively. These results indicate that thermal conductivity of PA/AC composite was enhanced up to 94.69 % by adding 6wt% GNPs while the enthalpy of melting was decreased only by~ 4%.

Table 4-24: Thermal conductivities of the PA/AC SSPCMs

Sample	wt% GNPs	Thermal conductivity (W/m K)	Thermal conductivity enhancement (%)[(a)]	
			E1	E2
PA	----	0.280	----	----
S1	0	0.283	1.07	----
S2	1	0.292	4.28	3.18
S3	2	0.334	19.28	18.02
S4	4	0.393	40.35	38.86
S5	6	0.551	96.78	94.69

(a)E_1: Thermal conductivity enhancement comparing with PA.
E_2: Thermal conductivity enhancement comparing with PA/AC.

The enhancement of thermal conductivity was also examined by evaluating the thermal images of SSPCMs in melting process and the results are shown in Figure 4-77. The thermal images were taken after the same time by putting the SSPCMs on the hot plate at 100°C.

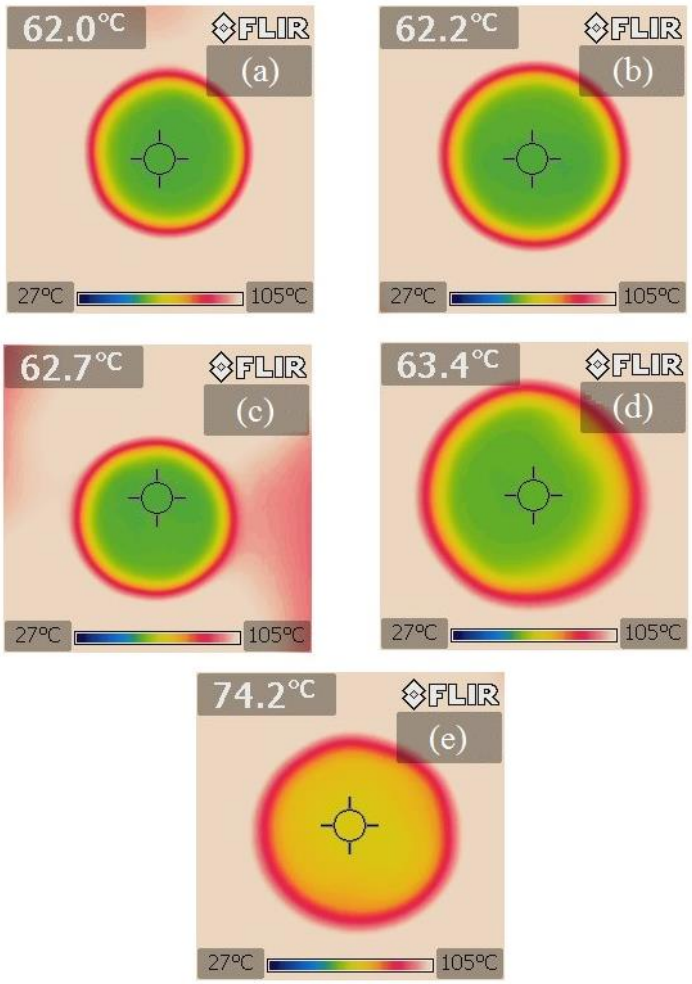

Figure 4-77: IR thermal images of (a) S1 (b) S2 (c) S3 (d) S4 (e) S5

The results demonstrate that after the same time, the temperatures were 62, 62.2, 62.7, 63.4 and 74.2°C for S1, S2, S3, S4 and S5, respectively. It can be seen that the temperature difference between S1 and S5 was about 12.2°C and confirms that thermal conductivity of the PA/AC composite was enhanced significantly by adding GNPs.

4.7.8 Thermal Reliability

Accelerated thermal cycle for 1000 cycles was performed for PA/AC SSPCMs to evaluate their thermal reliability. The melting latent heat of the composite PCMs with different mass percentage of GNPs before and after 1000 thermal cycles is shown in Figure 4-78. The melting latent heat value changes by -1.6%,-1.2%,-0.8%,-0.3% and -0.1% for the S1, S2, S3, S4 and S5, respectively. The small and irregular changes in latent heat appeared at a reasonable level for thermal storage application. Therefore, the

SSPCMs with activated carbon as supporting material possess good thermal reliability as confirmed by the variations in their energy storage capacities.

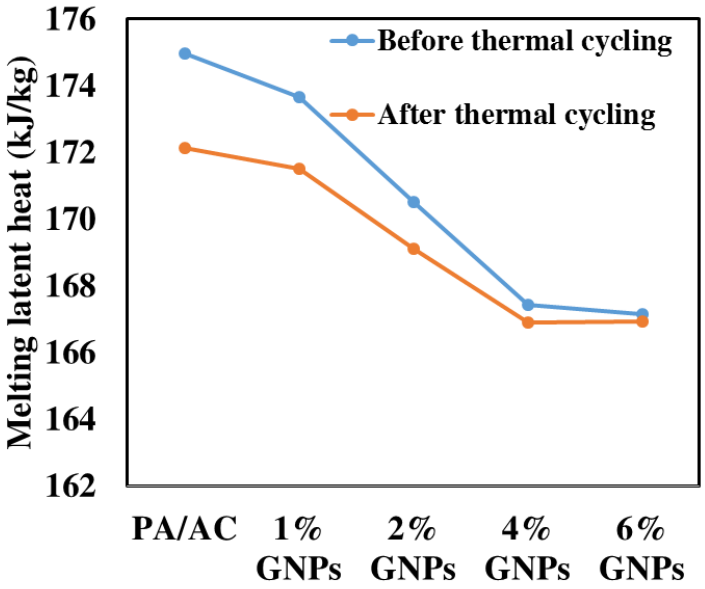

Figure 4-78: Latent heat of composite PCMs before and after thermal cycling

4.8 Comparison of Graphene and Porous Carbon SSPCMs

The entire strategy of choosing the ideal PCM is extremely complicated but crucial for thermal energy storage. The potential PCM should have a suitable melting temperature, desirable heat of fusion and thermal conductivity specified by the practical application. In this project, graphene materials were proposed as a supporting material to enhance the thermal properties of PCMs while some SSPCMs were also prepared by using porous carbon materials for comparison purpose. The research plan thus includes processing of both graphene and porous carbon composites and their characterization for thermal energy storage systems. For each supporting matrix several composites were prepared with different mass percentages. For the comparison, the results were presented based on higher retained PCM (%) or higher thermal conductivity enhancement for each SSPCM and shown in Figure 4-79 and Figure 4-80.

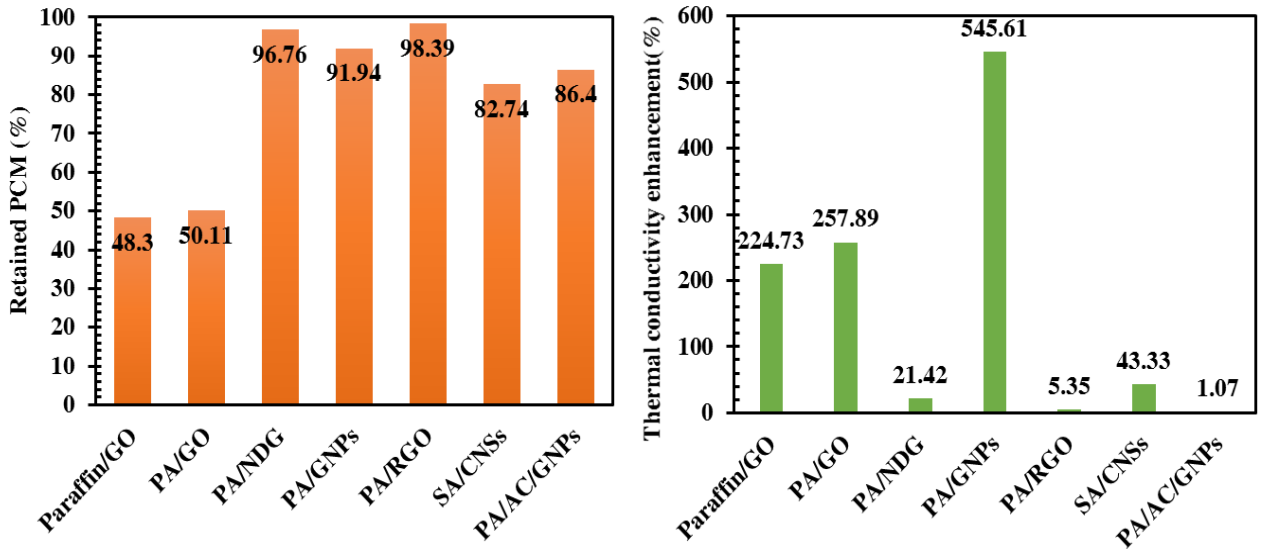

Figure 4-79: Retained PCM and thermal conductivity enhancement based on higher retained PCM

Figure 4-79 shows the results based on higher retained PCM for each composite PCM. It can be clearly seen that PA/RGO SSPCM provides the highest PCM content while the thermal conductivity was enhanced by only 5.35%. PA/GNPs SSPCM indicates the fantastic properties if we consider the highest retained PCM with highest thermal conductivity enhancement. PA/GNPs composite contains of 91.94% PA while the thermal conductivity was increased up to 5.5 times of the PA. The lowest thermal conductivity enhancement was found for PA/AC composite while the paraffin/GO composite reveals the lowest retained PCM with considerable thermal conductivity enhancement.

Figure 4-80 shows the results based on higher thermal conductivity enhancement for each composite PCM. The results indicate that the highest thermal conductivity enhancement (791.22%) was achieved by using GNPs as a supporting materials with retained PCM of 77.99%. However, PA/NDG composite also shows significant thermal conductivity enhancement of 517.85% with higher retained PCM (94.77%) compare to PA/GNPs SSPCM. These results suggested that between the prepared SSPCMs graphene composites including GNPs and NDG had a remarkable thermal conductivity

enhancements with higher PCM content compare to the other SSPCMs. The porous carbon SSPCMs shown acceptable PCM content but they cannot be contrasted with graphene composites when it comes to the thermal conductivity enhancement.

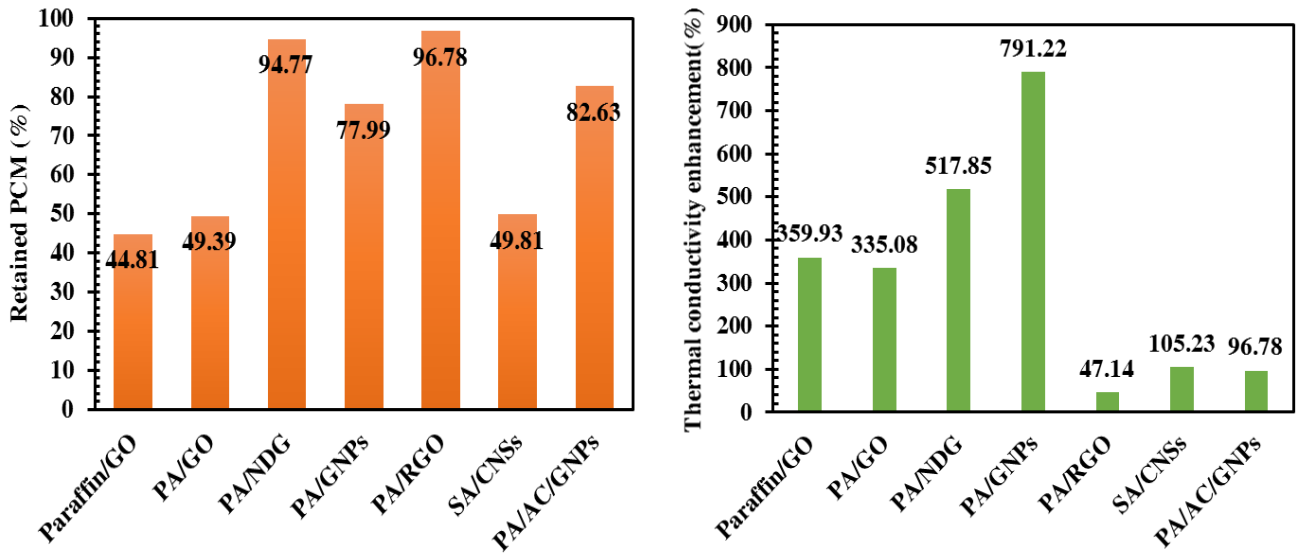

Figure 4-80: Retained PCM and thermal conductivity enhancement based on higher thermal conductivity enhancement

The drastically different characteristics between the thermal conductivities for graphene and porous carbon loaded PCMs are extremely interesting and can shed light on the crucial mechanisms underlying the phenomena of nanoscale heat transfer between graphene flakes. In spite of the primary and practical importance of the information regarding the thermal conductivity of graphene, couple of studies have been reported up to now about the flake-to-flake heat transfer as well as the interfacial thermal resistance, which are truly the dominant factors affecting the efficiency in real applications instead of the superior in-plane monolayer thermal conductivity (Zhou et al., 2013).

For existing applications, graphene will help reduce the amount of additives required for shape-stabilization. With the addition of an appropriate amount of graphene materials at low loading contents, thermal conductivity enhancement and shape-stabilization of PCMs can be simultaneously accomplished while high latent heat is

retained. However, the costs will be higher than porous carbon materials due to the complicated synthesis process of graphene materials. In addition, CNSs and AC SSPCMs deliver outstanding thermal stability with stable melting–freezing enthalpy and exceptional reversibility with their combination of low-cost raw materials, green preparation process and involves minimal cost are believed to have promising potential applications in many energy-related devices.

4.9 Summary

This research looked into the effects of adding graphene materials or porous carbons to enhance the thermal conductivity and shape-stability of organic PCMs. Paraffin and fatty acid -based nanocomposite PCMs filled with carbon nanomaterials of numerous shapes and sizes have been prepared and characterized experimentally. The melting/solidification enthalpies have been found to reduce almost linearly as a result of addition of the carbon nanofillers and their variations are weakly linked with the shape and size of the fillers. The melting/solidification temperatures were slightly changed because of the filler-induced reduction of steric hindrance of the surrounding PCM molecules.

The thermal conductivity of the composite PCMs improves using the carbon additives while graphene materials indicate a greater thermal conductivity improvement than porous carbons as well as higher PCM adsorption.

We found that graphene materials can build thermally percolating network at lower loading ratio, while offering an obviously better thermal conductivity enhancement compare to the porous carbons.

Form the results, we have found the maximum thermal conductivity enhancement of 791.22% for PA/GNPs SSPCM containing 77.99 wt% of PA while the minimum enhancement was belong to PA/AC SSPCM (1.07%) with 86.4wt% of PA. The planar

GNPs, however, outperform significantly all the counterparts due to their geometry-induced low thermal interface resistance. The PA/RGO SSPCM shown maximum mass percentage of retained PCM was about 98.39 wt% and the lowest was 44.81 wt% that was belong to the paraffin/GO SSPCM.

In summary, graphene nanomaterials have been shown to be a promising filler material for preparing nanocomposite PCMs with greatly enhanced thermal conductivity and moderately decreased energy storage capacity, which have great potential in TES applications. Future work is needed to reveal the size- and thickness-dependent performance of graphene nanofillers, in an effort to facilitate optimization or realization of active control of the thermal conductivity of graphene-based nanocomposite PCMs. Moreover, dispersion of graphene nanofillers, owing to their hydrophilic nature in polar solvents like organic PCMs should be further studied. The primary challenge to be addressed is the dispersion and stability of graphene nanofillers in the nanocomposite PCMs upon solid–liquid phase transitions.

CHAPTER 5
CONCLUSION AND RECOMMENDATION

This chapter discusses on the conclusions derived from the results of the experiments and recommends further procedure and experiments which could have been done if limitations in experimental instruments and time were not a factor to conduct further research.

5.1 Conclusion

In this research, SSPCMs were fabricated and characterized to develop new composite materials for thermal energy storage. Composite technology was applied to enhance the thermal conductivity and form stability properties of organic PCMs by using various carbon nanofillers. Among the different nanofillers considered, carbon nanomaterials have been recommended since they have particularly high thermal conductivity and relatively low density. Consequently, this research is focused at evaluating the performance of carbon nanofillers of different shapes and sizes in improving the thermal conductivity and shape stabilizing of organic-based SSPCMs. Following the objective of the work, organic-based SSPCMs filled with carbon nanomaterials of various sizes and shapes have been prepared and characterized experimentally. The melting/solidification enthalpies have been shown to decrease almost linearly due to addition of the carbon nanofillers and their variations are weakly linked to the size and shape of the fillers. The melting/solidification temperatures are slightly changed due to the filler-induced reduction of steric hindrance of the surrounding PCM molecules. Thermal conductivity enhancement has been clearly shown to strongly depend on geometry of the various carbon nanofillers. Among the four graphene fillers, the planar GNPs outperform significantly all the counterparts due to their geometry-induced low thermal interface resistance. The greatest thermal conductivity enhancement of GNP-

based SSPCMs has been measured to be nearly 545% with PCM content of 92wt%.The discrepancy associated with the measured thermal conductivity data of SSPCMs with graphene nanofillers of various sizes and thicknesses reported here and has been found to be remarkable, indicating that the performance of graphene fillers is relied on the control of their size and specific surface area. It has also been found that the very thin graphene of only few layers may not be favorable in serving as thermal conductivity fillers as a result of the presence of greater thermal interface resistance in comparison to larger and thicker GNPs. In summary, the graphene nanofillers have been shown to be a promising filler material for preparing nanocomposite PCMs with greatly enhanced thermal conductivity and moderately decreased energy storage capacity, which have great potential in TES applications.

5.2 Recommendations

The aim of the current research was to explore the improvement of novel SSPCMs for TES applications. Future work is needed to reveal the size- and thickness-dependent performance of graphene nanofillers, in an effort to facilitate optimization, or realization of active control, of the thermal conductivity of graphene-based nanocomposite PCMs. Since graphene is the most thermally conductive material known, it is expected to increase the thermal conductivity of PCMs much more significantly. However, the graphene that we used for this study is fabricated using thermal reduction of graphite oxide, which is not the best type of graphene for thermal conductivity improvement purposes due to the abundance of the oxygen groups and defects. Higher quality graphene fillers might have an even more significant effect on organic phase change materials. Also, the ultimate goal of increasing the thermal conductivity in PCMs is to obtain a higher conversion rate during the storage/release process. The change in this rate after the addition of graphene fillers into the PCM could be investigated in more details. In the literature, there are different theoretical approaches for the analysis of conduction heat

transfer of SSPCMs. In order to understand the validity of the proposed approaches, numerical analyses that are based on those approaches are useful. At present, numerical studies in the literature about this issue are not sufficient to reach a conclusion about the accuracy of the approaches. On the other hand, there is very limited experimental data about conduction heat transfer of SSPCMs and this prevents the systematic comparison of numerical results with experimental findings.

Similar to the case of thermal conductivity, conduction heat transfer of SSPCMs is also dependent on many parameters such as particle volume fraction, particle size, particle material, temperature, and base PCM type. Detailed experimental investigation of the effects of most of these parameters on heat transfer has not been performed yet. Systematic studies about these aspects of SSPCMs on heat transfer will provide valuable information for the optimization of heat transfer enhancement obtained with SSPCMs. In the case of product engineering several improvements and suitable developments can be wished, first of all the test of the SSPCMs by a test rig or by some field tests.

The described results indicate that graphene has the potential to outperform metal nanoparticles and carbon allotropes as filler in materials for thermal management. Some medium temperature application for prepared SSPCMs can be defined as below:

- Off-peak power utilization: Heating hot water and Cooling
- Solar power plants
- Waste heat recovery
- Cooling of heat and electrical engines

In summary, greater effort must be directed to both fundamental and applied investigations of SSPCMs with the aid of advanced experimental and numerical techniques.

APPENDIX

LIST OF PUBLICATIONS RELATED TO THESIS

(1) Mehrali M, Latibari ST, Mehrali M, Metselaar HSC, Silakhori M (2013) Shape-stabilized phase change materials with high thermal conductivity based on paraffin/graphene oxide composite. **Energy Conversion and Management** 67:275-282. **Impact factor: 3.59 (Q1)**

(2) Mehrali M, Latibari ST, Mehrali M, Indra Mahlia TM, Cornelis Metselaar HS (2013) Preparation and properties of highly conductive palmitic acid/graphene oxide composites as thermal energy storage materials. **Energy** 58: 628-634. **Impact factor: 4.15 (Q1)**

(3) Mehrali M, Latibari ST, Mehrali M, Indra Mahlia TM, Cornelis Metselaar HS, et al. (2013) Preparation and characterization of palmitic acid/graphene nanoplatelets composite with remarkable thermal conductivity as a novel shape- stabilized phase change material. **Applied Thermal Engineering** 61: 633-640. **Impact factor: 2.127 (Q1)**

(4) Mehrali M, Latibari ST, Mehrali M, Mahlia TMI, Metselaar HSC. Effect of carbon nanospheres on shape stabilization and thermal behavior of phase change materials for thermal energy storage. **Energy Conversion and Management**.2014; 88:206-13. **Impact factor: 3.59 (Q1)**

(5) Mehrali M, Latibari ST, Mehrali M, Mahlia TMI, Sadeghinezhad E, Metselaar HSC. Preparation of nitrogen-doped graphene/palmitic acid shape stabilized composite phase change material with remarkable thermal properties for thermal energy storage. **Applied Energy**. 2014; 135:339-49. **Impact factor: 5.26 (Q1)**

REFERENCES

Abhat, A. (1983). Low temperature latent heat thermal energy storage: Heat storage materials. *Solar Energy*, 30(4), 313-332.

Agyenim, F., & Hewitt, N. (2010). The development of a finned phase change material (PCM) storage system to take advantage of off-peak electricity tariff for improvement in cost of heat pump operation. *Energy and Buildings*, 42(9), 1552-1560.

Akgün, M., Aydın, O., & Kaygusuz, K. (2008). Thermal energy storage performance of paraffin in a novel tube-in-shell system. *Applied Thermal Engineering*, 28(5–6), 405-413.

Akhavan, O., Abdolahad, M., Esfandiar, A., & Mohatashamifar, M. (2010). Photodegradation of Graphene Oxide Sheets by TiO2 Nanoparticles after a Photocatalytic Reduction. *The Journal of Physical Chemistry C*, 114(30), 12955-12959.

Akhavan, O., Kalaee, M., Alavi, Z. S., Ghiasi, S. M. A., & Esfandiar, A. (2012). Increasing the antioxidant activity of green tea polyphenols in the presence of iron for the reduction of graphene oxide. *Carbon*, 50(8), 3015-3025.

Alkan, C., Sari, A., & Uzun, O. (2006). Poly (ethylene glycol)/acrylic polymer blends for latent heat thermal energy storage. *AIChE journal*, 52(9), 3310-3314.

Amin, N. A. M., Bruno, F., & Belusko, M. (2014). Effective thermal conductivity for melting in PCM encapsulated in a sphere. *Applied Energy*, 122(0), 280-287.

Baetens, R., Jelle, B. P., & Gustavsen, A. (2010). Phase change materials for building applications: A state-of-the-art review. *Energy and Buildings*, 42(9), 1361-1368.

Bai, H., Li, C., Wang, X., & Shi, G. (2011). On the Gelation of Graphene Oxide. *The Journal of Physical Chemistry C*, 115(13), 5545-5551.

Balandin, A. A., Ghosh, S., Bao, W., Calizo, I., Teweldebrhan, D., Miao, F., & Lau, C. N. (2008). Superior thermal conductivity of single-layer graphene. *Nano letters*, 8(3), 902-907.

Becerril, H. A., Mao, J., Liu, Z., Stoltenberg, R. M., Bao, Z., & Chen, Y. (2008). Evaluation of solution-processed reduced graphene oxide films as transparent conductors. *ACS nano*, 2(3), 463-470.

Bershteæin, V., & Egorov, V. (1994). *Differential scanning calorimetry of polymers: physics, chemistry, analysis, technology*: Ellis Horwood, New York.

Birchenall, C. E., & Riechman, A. (1980). Heat storage in eutectic alloys. *Metallurgical Transactions A*, 11(8), 1415-1420.

Bitaraf Haghighi, E., Anwar, Z., Lumbreras, I., Mirmohammadi, S. A., Behi, M., Khodabandeh, R., & Palm, B. (2012). Screening Single Phase Laminar Convective Heat

Transfer of Nanofluids in a Micro-tube. Proceedings of Journal of Physics: Conference Series (pp. 012036).

Brown, K. G., Bicknell-Brown, E., & Ladjadj, M. (1987). Raman-active bands sensitive to motion and conformation at the chain termini and backbones of alkanes and lipids. *The Journal of Physical Chemistry*, 91(12), 3436-3442.

Bundy, F., Bassett, W., Weathers, M., Hemley, R., Mao, H., & Goncharov, A. (1996). The pressure-temperature phase and transformation diagram for carbon; updated through 1994. *Carbon*, 34(2), 141-153.

Cabeza, L., Castell, A., Barreneche, C., De Gracia, A., & Fernández, A. (2011). Materials used as PCM in thermal energy storage in buildings: a review. *Renewable and Sustainable Energy Reviews*, 15(3), 1675-1695.

Cai, Y., Hu, Y., Song, L., Lu, H., Chen, Z., & Fan, W. (2006). Preparation and characterizations of HDPE–EVA alloy/OMT nanocomposites/paraffin compounds as a shape stabilized phase change thermal energy storage material. *Thermochimica acta*, 451(1), 44-51.

Cappella, B., & Dietler, G. (1999). Force-distance curves by atomic force microscopy. *Surface Science Reports*, 34(1–3), 1-104.

Castell, A., Belusko, M., Bruno, F., & Cabeza, L. F. (2011). Maximisation of heat transfer in a coil in tank PCM cold storage system. *Applied Energy*, 88(11), 4120-4127.

Castell, A., Solé, C., Medrano, M., Roca, J., Cabeza, L. F., & García, D. (2008). Natural convection heat transfer coefficients in phase change material (PCM) modules with external vertical fins. *Applied Thermal Engineering*, 28(13), 1676-1686.

Chan, L., Cheung, W., Allen, S., & McKay, G. (2009). Separation of acid-dyes mixture by bamboo derived active carbon. *Separation and Purification Technology*, 67(2), 166-172.

Chen, C., Wang, L., & Huang, Y. (2009). Ultrafine electrospun fibers based on stearyl stearate/polyethylene terephthalate composite as form stable phase change materials. *Chemical Engineering Journal*, 150(1), 269-274.

Chen, Z., Shan, F., Cao, L., & Fang, G. (2012). Synthesis and thermal properties of shape-stabilized lauric acid/activated carbon composites as phase change materials for thermal energy storage. *Solar Energy Materials and Solar Cells*, 102(0), 131-136.

Cheng, W.-l., Zhang, R.-m., Xie, K., Liu, N., & Wang, J. (2010). Heat conduction enhanced shape-stabilized paraffin/HDPE composite PCMs by graphite addition: Preparation and thermal properties. *Solar Energy Materials and Solar Cells*, 94(10), 1636-1642.

Compton, O. C., Dikin, D. A., Putz, K. W., Brinson, L. C., & Nguyen, S. T. (2010). Electrically Conductive "Alkylated" Graphene Paper via Chemical Reduction of Amine-Functionalized Graphene Oxide Paper. *Advanced Materials*, 22(8), 892-896.

Cowie, J. M. (1991). *Polymers: chemistry and physics of modern materials*: CRC Press.

Dincer, I., & Dost, S. (1996). A perspective on thermal energy storage systems for solar energy applications. *International Journal of Energy Research*, 20(6), 547-557.

Dolado, P., Lazaro, A., Marin, J. M., & Zalba, B. (2011). Characterization of melting and solidification in a real scale PCM-air heat exchanger: Numerical model and experimental validation. *Energy Conversion and Management*, 52(4), 1890-1907.

Ehid, R., Weinstein, R. D., & Fleischer, A. S. (2012). The shape stabilization of paraffin phase change material to reduce graphite nanofiber settling during the phase change process. *Energy Conversion and Management*, 57(0), 60-67.

Elgafy, A., & Lafdi, K. (2005). Effect of carbon nanofiber additives on thermal behavior of phase change materials. *Carbon*, 43(15), 3067-3074.

Fahmi, M. Z., & Chang, J.-Y. (2013). Forming double layer-encapsulated quantum dots for bio-imaging and cell targeting. *Nanoscale*, 5(4), 1517-1528.

Fan, L.-W., Fang, X., Wang, X., Zeng, Y., Xiao, Y.-Q., Yu, Z.-T., Xu, X., Hu, Y.-C., & Cen, K.-F. (2013). Effects of various carbon nanofillers on the thermal conductivity and energy storage properties of paraffin-based nanocomposite phase change materials. *Applied Energy*, 110(0), 163-172.

Fang, G., Li, H., Chen, Z., & Liu, X. (2010). Preparation and characterization of stearic acid/expanded graphite composites as thermal energy storage materials. *Energy*, 35(12), 4622-4626.

Fang, G., Li, H., Chen, Z., & Liu, X. (2011). Preparation and properties of palmitic acid/SiO2 composites with flame retardant as thermal energy storage materials. *Solar Energy Materials and Solar Cells*, 95(7), 1875-1881.

Fang, X., Fan, L., Ding, Q., Wang, X., Yao, X., Hou, J., Yu, Z.-T., Cheng, G., Hu, Y., & Cen, K. (2013). Increased thermal conductivity of eicosane-based composite phase change materials in the presence of graphene nanoplatelets. *Energy Fuels*, 27(7), 4041-4047.

Farid, M. M., Khudhair, A. M., Razack, S. A. K., & Al-Hallaj, S. (2004). A review on phase change energy storage: materials and applications. *Energy conversion and management*, 45(9), 1597-1615.

Fernandes, D., Pitié, F., Cáceres, G., & Baeyens, J. (2012). Thermal energy storage: "How previous findings determine current research priorities". *Energy*, 39(1), 246-257.

Ferrari, A. C., & Robertson, J. (2000). Interpretation of Raman spectra of disordered and amorphous carbon. *Physical Review B*, 61(20), 14095-14107.

Frankl, P., & Nowak, S. (2010). *Technology roadmap: solar photovoltaic energy*: OECD/IEA.

Frusteri, F., Leonardi, V., Vasta, S., & Restuccia, G. (2005). Thermal conductivity measurement of a PCM based storage system containing carbon fibers. *Applied thermal engineering*, 25(11), 1623-1633.

Fukuyama, H., & Terai, S. (2008). Preparing and characterizing the active carbon produced by steam and carbon dioxide as a heavy oil hydrocracking catalyst support. *Catalysis Today*, 130(2), 382-388.

Garg, H., Mullick, S., & Bhargava, A. (1985). *Solar thermal energy storage*: Springer.

Geng, D., Yang, S., Zhang, Y., Yang, J., Liu, J., Li, R., Sham, T.-K., Sun, X., Ye, S., & Knights, S. (2011). Nitrogen doping effects on the structure of graphene. *Applied Surface Science*, 257(21), 9193-9198.

Ghosh, S., Bao, W., Nika, D. L., Subrina, S., Pokatilov, E. P., Lau, C. N., & Balandin, A. A. (2010). Dimensional crossover of thermal transport in few-layer graphene. *Nature materials*, 9(7), 555-558.

Goldstein, J. I., Newbury, D. E., Echlin, P., Joy, D. C., Fiori, C., & Lifshin, E. (1981). *Scanning electron microscopy and X-ray microanalysis. A text for biologists, materials scientists, and geologists*: Plenum Publishing Corporation.

Goswami, D. Y., Kreith, F., & Kreider, J. F. (2000). *Principles of solar engineering*: CRC Press.

Guo, H.-L., Su, P., Kang, X., & Ning, S.-K. (2013). Synthesis and characterization of nitrogen-doped graphene hydrogels by hydrothermal route with urea as reducing-doping agents. *Journal of Materials Chemistry A*, 1(6), 2248-2255.

Hasnain, S. M. (1998). Review on sustainable thermal energy storage technologies, Part I: heat storage materials and techniques. *Energy Conversion and Management*, 39(11), 1127-1138.

Hawlader, M., Uddin, M., & Khin, M. M. (2003). Microencapsulated PCM thermal-energy storage system. *Applied energy*, 74(1), 195-202.

Herrmann, U., & Kearney, D. W. (2002). Survey of thermal energy storage for parabolic trough power plants. *Journal of Solar Energy Engineering*, 124(2), 145-152.

Hong, Y., & Xin-shi, G. (2000). Preparation of polyethylene–paraffin compound as a form-stable solid-liquid phase change material. *Solar Energy Materials and Solar Cells*, 64(1), 37-44.

Hu, J., Gao, Q., Wu, Y., & Song, S. (2007). A novel kind of copper–active carbon nanocomposites with their high hydrogen storage capacities at room temperature. *International Journal of Hydrogen Energy*, 32(12), 1943-1948.

Inagaki, M. (2000). *New carbons-control of structure and functions*: Elsevier.

Ismail, K., Alves, C., & Modesto, M. (2001). Numerical and experimental study on the solidification of PCM around a vertical axially finned isothermal cylinder. *Applied Thermal Engineering*, 21(1), 53-77.

Karaipekli, A., & Sarı, A. (2008). Capric–myristic acid/expanded perlite composite as form-stable phase change material for latent heat thermal energy storage. *Renewable Energy*, 33(12), 2599-2605.

Karaipekli, A., & Sarı, A. (2009). Capric–myristic acid/vermiculite composite as form-stable phase change material for thermal energy storage. *Solar Energy*, 83(3), 323-332.

Kaygusuz, K., & Sari, A. (2007). High density polyethylene/paraffin composites as form-stable phase change material for thermal energy storage. *Energy Sources, Part A*, 29(3), 261-270.

Kelly, R. (2000). Latent heat storage in building materials. *AMEC Design*.

Khudhair, A. M., & Farid, M. M. (2004). A review on energy conservation in building applications with thermal storage by latent heat using phase change materials. *Energy conversion and management*, 45(2), 263-275.

Kim, Y., An, T. K., Kim, J., Hwang, J., Park, S., Nam, S., Cha, H., Park, W. J., Baik, J. M., & Park, C. E. (2014). A composite of a graphene oxide derivative as a novel sensing layer in an organic field-effect transistor. *Journal of Materials Chemistry C*, 2(23), 4539-4544.

Krafft, C., Neudert, L., Simat, T., & Salzer, R. (2005). Near infrared Raman spectra of human brain lipids. *Spectrochimica Acta Part A: Molecular and Biomolecular Spectroscopy*, 61(7), 1529-1535.

Kuznik, F., David, D., Johannes, K., & Roux, J.-J. (2011). A review on phase change materials integrated in building walls. *Renewable and Sustainable Energy Reviews*, 15(1), 379-391.

Lee, S.-Y., Shin, H. K., Park, M., Rhee, K. Y., & Park, S.-J. (2014). Thermal characterization of erythritol/expanded graphite composites for high thermal storage capacity. *Carbon*, 68(0), 67-72.

Li, D., Muller, M. B., Gilje, S., Kaner, R. B., & Wallace, G. G. (2008). Processable aqueous dispersions of graphene nanosheets. *Nat Nano*, 3(2), 101-105.

Li, M., Wu, Z., & Kao, H. (2011a). Study on preparation and thermal properties of binary fatty acid/diatomite shape-stabilized phase change materials. *Solar Energy Materials and Solar Cells*, 95(8), 2412-2416.

Li, M., Wu, Z., & Tan, J. (2012). Properties of form-stable paraffin/silicon dioxide/expanded graphite phase change composites prepared by sol–gel method. *Applied Energy*, 92(0), 456-461.

Li, Y., Gao, W., Ci, L., Wang, C., & Ajayan, P. M. (2010). Catalytic performance of Pt nanoparticles on reduced graphene oxide for methanol electro-oxidation. *Carbon*, 48(4), 1124-1130.

Li, Y., Zhu, J., Wei, S., Ryu, J., Sun, L., & Guo, Z. (2011b). Poly(propylene)/Graphene Nanoplatelet Nanocomposites: Melt Rheological Behavior and Thermal, Electrical, and Electronic Properties. *Macromolecular Chemistry and Physics*, 212(18), 1951-1959.

Lillo-Ródenas, M. A., Cazorla-Amorós, D., & Linares-Solano, A. (2003). Understanding chemical reactions between carbons and NaOH and KOH: An insight into the chemical activation mechanism. *Carbon*, 41(2), 267-275.

Liu, M., Saman, W., & Bruno, F. (2012). Review on storage materials and thermal performance enhancement techniques for high temperature phase change thermal storage systems. *Renewable and Sustainable Energy Reviews*, 16(4), 2118-2132.

Lu, Y., Zhang, F., Zhang, T., Leng, K., Zhang, L., Yang, X., Ma, Y., Huang, Y., Zhang, M., & Chen, Y. (2013). Synthesis and supercapacitor performance studies of N-doped graphene materials using o-phenylenediamine as the double-N precursor. *Carbon*, 63(0), 508-516.

Lv, Y., Gan, L., Liu, M., Xiong, W., Xu, Z., Zhu, D., & Wright, D. S. (2012). A self-template synthesis of hierarchical porous carbon foams based on banana peel for supercapacitor electrodes. *Journal of Power Sources*, 209(0), 152-157.

Ma, L., Ning, P., Zhang, Y., & Wang, X. (2008). Experimental and modeling of fixed-bed reactor for yellow phosphorous tail gas purification over impregnated activated carbon. *Chemical Engineering Journal*, 137(3), 471-479.

Mahmoud, S., Tang, A., Toh, C., Al-Dadah, R., & Soo, S. L. (2013). Experimental investigation of inserts configurations and PCM type on the thermal performance of PCM based heat sinks. *Applied Energy*, 112(0), 1349-1356.

Mehling, H., & Cabeza, L. F. (2008). Heat and cold storage with PCM. *Hand book, Publisher Springer, Germany*.

Memon, S. A. (2014). Phase change materials integrated in building walls: A state of the art review. *Renewable and Sustainable Energy Reviews*, 31(0), 870-906.

Mesalhy, O., Lafdi, K., & Elgafy, A. (2006). Carbon foam matrices saturated with PCM for thermal protection purposes. *Carbon*, 44(10), 2080-2088.

Mills, A., Farid, M., Selman, J., & Al-Hallaj, S. (2006). Thermal conductivity enhancement of phase change materials using a graphite matrix. *Applied Thermal Engineering*, 26(14), 1652-1661.

Moeini Sedeh, M., & Khodadadi, J. M. (2013). Thermal conductivity improvement of phase change materials/graphite foam composites. *Carbon*, 60(0), 117-128.

Mohamed, M. M. (2005). Solidification of phase change material on vertical cylindrical surface in holdup air bubbles. *International Journal of Refrigeration*, 28(3), 403-411.

Moreno, P., Miró, L., Solé, A., Barreneche, C., Solé, C., Martorell, I., & Cabeza, L. F. (2014). Corrosion of metal and metal alloy containers in contact with phase change materials (PCM) for potential heating and cooling applications. *Applied Energy*, 125(0), 238-245.

Nakaso, K., Teshima, H., Yoshimura, A., Nogami, S., Hamada, Y., & Fukai, J. (2008). Extension of heat transfer area using carbon fiber cloths in latent heat thermal energy storage tanks. *Chemical Engineering and Processing: Process Intensification*, 47(5), 879-885.

Nkwetta, D. N., & Haghighat, F. (2014). Thermal energy storage with phase change material—A state-of-the art review. *Sustainable Cities and Society*, 10(0), 87-100.

Oró, E., De Gracia, A., Castell, A., Farid, M., & Cabeza, L. (2012). Review on phase change materials (PCMs) for cold thermal energy storage applications. *Applied Energy*, 99, 513-533.

Oya, T., Nomura, T., Tsubota, M., Okinaka, N., & Akiyama, T. (2013). Thermal conductivity enhancement of erythritol as PCM by using graphite and nickel particles. *Applied Thermal Engineering*, 61(2), 825-828.

Özonur, Y., Mazman, M., Paksoy, H. Ö., & Evliya, H. (2006). Microencapsulation of coco fatty acid mixture for thermal energy storage with phase change material. *International Journal of Energy Research*, 30(10), 741-749.

Panchakarla, L. S., Subrahmanyam, K. S., Saha, S. K., Govindaraj, A., Krishnamurthy, H. R., Waghmare, U. V., & Rao, C. N. R. (2009). Synthesis, Structure, and Properties of Boron- and Nitrogen-Doped Graphene. *Advanced Materials*, 21(46), 4726-4730.

Pasquini, C. (2003). Near infrared spectroscopy: fundamentals, practical aspects and analytical applications. *Journal of the Brazilian Chemical Society*, 14(2), 198-219.

Pasupathy, A., Velraj, R., & Seeniraj, R. V. (2008). Phase change material-based building architecture for thermal management in residential and commercial establishments. *Renewable and Sustainable Energy Reviews*, 12(1), 39-64.

Peng, E., Choo, E. S. G., Chandrasekharan, P., Yang, C.-T., Ding, J., Chuang, K.-H., & Xue, J. M. (2012). Synthesis of Manganese Ferrite/Graphene Oxide Nanocomposites for Biomedical Applications. *Small*, 8(23), 3620-3630.

Pillai, K. K., & Brinkworth, B. J. (1976). The storage of low grade thermal energy using phase change materials. *Applied Energy*, 2(3), 205-216.

Pincemin, S., Olives, R., Py, X., & Christ, M. (2008). Highly conductive composites made of phase change materials and graphite for thermal storage. *Solar Energy Materials and Solar Cells*, 92(6), 603-613.

Pitié, F., Zhao, C. Y., Baeyens, J., Degrève, J., & Zhang, H. L. (2013). Circulating fluidized bed heat recovery/storage and its potential to use coated phase-change-material (PCM) particles. *Applied Energy*, 109(0), 505-513.

Qie, L., Chen, W., Xu, H., Xiong, X., Jiang, Y., Zou, F., Hu, X., Xin, Y., Zhang, Z., & Huang, Y. (2013). Synthesis of functionalized 3D hierarchical porous carbon for high-performance supercapacitors. *Energy & Environmental Science*, 6(8), 2497-2504.

Rathod, M. K., & Banerjee, J. (2013). Thermal stability of phase change materials used in latent heat energy storage systems: A review. *Renewable and Sustainable Energy Reviews*, 18(0), 246-258.

Regin, A. F., Solanki, S., & Saini, J. (2008). Heat transfer characteristics of thermal energy storage system using PCM capsules: a review. *Renewable and Sustainable Energy Reviews*, 12(9), 2438-2458.

Renyun, S. J. Z. (2005). Review of Thermal Energy Storage with Metal Phase Change Materials [J]. *Materials Review*, 8, 027.

Ryu, H. W., Woo, S. W., Shin, B. C., & Kim, S. D. (1992). Prevention of supercooling and stabilization of inorganic salt hydrates as latent heat storage materials. *Solar energy materials and solar cells*, 27(2), 161-172.

Salunkhe, P. B., & Shembekar, P. S. (2012). A review on effect of phase change material encapsulation on the thermal performance of a system. *Renewable and Sustainable Energy Reviews*, 16(8), 5603-5616.

Sarı, A. (2004). Form-stable paraffin/high density polyethylene composites as solid–liquid phase change material for thermal energy storage: preparation and thermal properties. *Energy Conversion and Management*, 45(13), 2033-2042.

Sari, A., Kara, A., & Kaygusuz, K. (2008). Fatty acid/expanded graphite composites as phase change material for latent heat thermal energy storage. *Energy Sources, Part A*, 30(5), 464-474.

Sari, A., Karaipekil, A., Akcay, M., Onal, A., & Kavak, F. (2006). Polymer/palmitic acid blends as shape-stabilized phase change material for latent heat thermal energy storage. *ASIAN JOURNAL OF CHEMISTRY*, 18(1), 439-446.

Sarı, A., & Karaipekli, A. (2007). Thermal conductivity and latent heat thermal energy storage characteristics of paraffin/expanded graphite composite as phase change material. *Applied Thermal Engineering*, 27(8), 1271-1277.

Sarı, A., & Karaipekli, A. (2008). Preparation, thermal properties and thermal reliability of capric acid/expanded perlite composite for thermal energy storage. *Materials Chemistry and Physics*, 109(2), 459-464.

Sarı, A., & Karaipekli, A. (2009). Preparation, thermal properties and thermal reliability of palmitic acid/expanded graphite composite as form-stable PCM for thermal energy storage. *Solar Energy Materials and Solar Cells*, 93(5), 571-576.

Sarı, A., Karaipekli, A., & Alkan, C. (2009). Preparation, characterization and thermal properties of lauric acid/expanded perlite as novel form-stable composite phase change material. *Chemical Engineering Journal*, 155(3), 899-904.

Sarier, N., & Onder, E. (2007). Thermal characteristics of polyurethane foams incorporated with phase change materials. *Thermochimica acta*, 454(2), 90-98.

Sharma, A., Tyagi, V. V., Chen, C. R., & Buddhi, D. (2009). Review on thermal energy storage with phase change materials and applications. *Renewable and Sustainable Energy Reviews*, 13(2), 318-345.

Sheng, Z.-H., Shao, L., Chen, J.-J., Bao, W.-J., Wang, F.-B., & Xia, X.-H. (2011). Catalyst-Free Synthesis of Nitrogen-Doped Graphene via Thermal Annealing Graphite Oxide with Melamine and Its Excellent Electrocatalysis. *ACS Nano*, 5(6), 4350-4358.

Shon, J., Kim, H., & Lee, K. (2014). Improved heat storage rate for an automobile coolant waste heat recovery system using phase-change material in a fin–tube heat exchanger. *Applied Energy*, 113(0), 680-689.

Siahpush, A., O'Brien, J., & Crepeau, J. (2008). Phase change heat transfer enhancement using copper porous foam. *Journal of Heat Transfer*, 130(8), 082301.

Siesler, H. W., Ozaki, Y., Kawata, S., & Heise, H. M. (2008). *Near-infrared spectroscopy: principles, instruments, applications*: John Wiley & Sons.

Simpson, D. R. (2008). Biofilm processes in biologically active carbon water purification. *Water research*, 42(12), 2839-2848.

Solomon, G. R., & Velraj, R. (2013). Analysis of the heat transfer mechanisms during energy storage in a Phase Change Material filled vertical finned cylindrical unit for free cooling application. *Energy Conversion and Management*, 75(0), 466-473.

Song, X., Gunawan, P., Jiang, R., Leong, S. S. J., Wang, K., & Xu, R. (2011). Surface activated carbon nanospheres for fast adsorption of silver ions from aqueous solutions. *Journal of Hazardous Materials*, 194(0), 162-168.

Szabó, T., Berkesi, O., Forgó, P., Josepovits, K., Sanakis, Y., Petridis, D., & Dékány, I. (2006). Evolution of surface functional groups in a series of progressively oxidized graphite oxides. *Chemistry of materials*, 18(11), 2740-2749.

Tahan Latibari, S., Mehrali, M., Mehrali, M., Indra Mahlia, T. M., & Cornelis Metselaar, H. S. (2013). Synthesis, characterization and thermal properties of nanoencapsulated phase change materials via sol–gel method. *Energy*, 61, 664-672.

Tahan Latibari, S., Mehrali, M., Mehrali, M., Mahlia, T. M. I., & Metselaar, H. S. C. (2014). Facile Preparation of Carbon Microcapsules Containing Phase-Change Material with Enhanced Thermal Properties. *The Scientific World Journal*, 2014, 5.

Tang, B., Qiu, M., & Zhang, S. (2012). Thermal conductivity enhancement of PEG/SiO< sub> 2</sub> composite PCM by in situ Cu doping. *Solar Energy Materials and Solar Cells*, 105, 242-248.

Tatsidjodoung, P., Le Pierrès, N., & Luo, L. (2013). A review of potential materials for thermal energy storage in building applications. *Renewable and Sustainable Energy Reviews*, 18(0), 327-349.

Tay, N., Bruno, F., & Belusko, M. (2013a). Comparison of pinned and finned tubes in a phase change thermal energy storage system using CFD. *Applied Energy*, 104, 79-86.

Tay, N. H. S., Bruno, F., & Belusko, M. (2013b). Experimental investigation of dynamic melting in a tube-in-tank PCM system. *Applied Energy*, 104(0), 137-148.

Telkes, M. (1952). Nucleation of supersaturated inorganic salt solutions. *Industrial & Engineering Chemistry*, 44(6), 1308-1310.

Teng, T.-P., Cheng, C.-M., & Cheng, C.-P. (2013). Performance assessment of heat storage by phase change materials containing MWCNTs and graphite. *Applied Thermal Engineering*, 50(1), 637-644.

Tong, S. W., Mishra, N., Su, C. L., Nalla, V., Wu, W., Ji, W., Zhang, J., Chan, Y., & Loh, K. P. (2014). High-Performance Hybrid Solar Cell Made from CdSe/CdTe Nanocrystals Supported on Reduced Graphene Oxide and PCDTBT. *Advanced Functional Materials*, 24(13), 1904-1910.

Trp, A. (2005). An experimental and numerical investigation of heat transfer during technical grade paraffin melting and solidification in a shell-and-tube latent thermal energy storage unit. *Solar Energy*, 79(6), 648-660.

Tyagi, V. V., & Buddhi, D. (2007). PCM thermal storage in buildings: a state of art. *Renewable and Sustainable Energy Reviews*, 11(6), 1146-1166.

Velraj, R., Seeniraj, R. V., Hafner, B., Faber, C., & Schwarzer, K. (1997). Experimental analysis and numerical modelling of inward solidification on a finned vertical tube for a latent heat storage unit. *Solar Energy*, 60(5), 281-290.

Velraj, R., Seeniraj, R. V., Hafner, B., Faber, C., & Schwarzer, K. (1999). HEAT TRANSFER ENHANCEMENT IN A LATENT HEAT STORAGE SYSTEM. *Solar Energy*, 65(3), 171-180.

Verdonck, E., Schaap, K., & Thomas, L. C. (1999). A discussion of the principles and applications of modulated temperature DSC (MTDSC). *International journal of pharmaceutics*, 192(1), 3-20.

Wang, J., Xie, H., & Xin, Z. (2009a). Thermal properties of paraffin based composites containing multi-walled carbon nanotubes. *Thermochimica Acta*, 488(1–2), 39-42.

Wang, W., Yang, X., Fang, Y., & Ding, J. (2009b). Preparation and performance of form-stable polyethylene glycol/silicon dioxide composites as solid–liquid phase change materials. *Applied Energy*, 86(2), 170-174.

Wang, W., Yang, X., Fang, Y., Ding, J., & Yan, J. (2009c). Enhanced thermal conductivity and thermal performance of form-stable composite phase change materials by using β-Aluminum nitride. *Applied Energy*, 86(7), 1196-1200.

Wang, W., Yang, X., Fang, Y., Ding, J., & Yan, J. (2009d). Preparation and thermal properties of polyethylene glycol/expanded graphite blends for energy storage. *Applied Energy*, 86(9), 1479-1483.

Wang, Y., Shao, Y., Matson, D. W., Li, J., & Lin, Y. (2010). Nitrogen-Doped Graphene and Its Application in Electrochemical Biosensing. *ACS Nano*, 4(4), 1790-1798.

Wang, Y., Tang, B., & Zhang, S. (2013). Single-Walled Carbon Nanotube/Phase Change Material Composites: Sunlight-Driven, Reversible, Form-Stable Phase Transitions for Solar Thermal Energy Storage. *Advanced Functional Materials*, 23(35), 4354-4360.

Wang, Z. (2000). Transmission electron microscopy of shape-controlled nanocrystals and their assemblies. *The Journal of Physical Chemistry B*, 104(6), 1153-1175.

Wen, D., & Ding, Y. (2004). Effective Thermal Conductivity of Aqueous Suspensions of Carbon Nanotubes (Carbon Nanotube Nanofluids). *Journal of Thermophysics and Heat Transfer*, 18(4), 481-485.

Wu, N., She, X., Yang, D., Wu, X., Su, F., & Chen, Y. (2012). Synthesis of network reduced graphene oxide in polystyrene matrix by a two-step reduction method for superior conductivity of the composite. *Journal of Materials Chemistry*, 22(33), 17254-17261.

Wu, S., Zhu, D., Zhang, X., & Huang, J. (2010). Preparation and Melting/Freezing Characteristics of Cu/Paraffin Nanofluid as Phase-Change Material (PCM). *Energy & Fuels*, 24(3), 1894-1898.

Xia, L., Zhang, P., & Wang, R. (2010). Preparation and thermal characterization of expanded graphite/paraffin composite phase change material. *Carbon*, 48(9), 2538-2548.

Xiao, M., Feng, B., & Gong, K. (2002). Preparation and performance of shape stabilized phase change thermal storage materials with high thermal conductivity. *Energy Conversion and Management*, 43(1), 103-108.

Xiao, X., Zhang, P., & Li, M. (2013). Preparation and thermal characterization of paraffin/metal foam composite phase change material. *Applied Energy*, 112(0), 1357-1366.

Yin, H., Gao, X., Ding, J., & Zhang, Z. (2008). Experimental research on heat transfer mechanism of heat sink with composite phase change materials. *Energy Conversion and Management*, 49(6), 1740-1746.

Yinping, Z., & Yi, J. (1999). A simple method, the-history method, of determining the heat of fusion, specific heat and thermal conductivity of phase-change materials. *Measurement Science and Technology*, 10(3), 201.

Yuan, D., Chen, J., Zeng, J., & Tan, S. (2008). Preparation of monodisperse carbon nanospheres for electrochemical capacitors. *Electrochemistry Communications*, 10(7), 1067-1070.

Zalba, B., Marín, J. M., Cabeza, L. F., & Mehling, H. (2003). Review on thermal energy storage with phase change: materials, heat transfer analysis and applications. *Applied thermal engineering*, 23(3), 251-283.

Zeng, J.-L., Zhu, F.-R., Yu, S.-B., Xiao, Z.-L., Yan, W.-P., Zheng, S.-H., Zhang, L., Sun, L.-X., & Cao, Z. (2013). Myristic acid/polyaniline composites as form stable phase change materials for thermal energy storage. *Solar Energy Materials and Solar Cells*, 114(0), 136-140.

Zhang, D., Zhou, J., Wu, K., & Li, Z. (2005). Granular phase changing composites for thermal energy storage. *Solar Energy*, 78(3), 471-480.

Zhang, J., Zhang, X., Wan, Y., Mei, D., & Zhang, B. (2012a). Preparation and thermal energy properties of paraffin/halloysite nanotube composite as form-stable phase change material. *Solar Energy*, 86(5), 1142-1148.

Zhang, L., Zhu, J., Zhou, W., Wang, J., & Wang, Y. (2011). Characterization of polymethyl methacrylate/polyethylene glycol/aluminum nitride composite as form-stable phase change material prepared by in situ polymerization method. *Thermochimica Acta*, 524(1), 128-134.

Zhang, P., Hu, Y., Song, L., Lu, H., Wang, J., & Liu, Q. (2009). Synergistic effect of iron and intumescent flame retardant on shape-stabilized phase change material. *Thermochimica Acta*, 487(1–2), 74-79.

Zhang, Y., Ding, J., Wang, X., Yang, R., & Lin, K. (2006a). Influence of additives on thermal conductivity of shape-stabilized phase change material. *Solar Energy Materials and Solar Cells*, 90(11), 1692-1702.

Zhang, Y., & Faghri, A. (1996). Heat transfer enhancement in latent heat thermal energy storage system by using the internally finned tube. *International Journal of Heat and Mass Transfer*, 39(15), 3165-3173.

Zhang, Y., Ma, H.-L., Zhang, Q., Peng, J., Li, J., Zhai, M., & Yu, Z.-Z. (2012b). Facile synthesis of well-dispersed graphene by γ-ray induced reduction of graphene oxide. *Journal of Materials Chemistry*, 22(26), 13064-13069.

Zhang, Y., Xu, X., Di, H., Lin, K., & Yang, R. (2006b). Experimental study on the thermal performance of the shape-stabilized phase change material floor used in passive solar buildings. *Journal of solar energy engineering*, 128(2), 255-257.

Zhang, Y. P., Lin, K. P., Yang, R., Di, H. F., & Jiang, Y. (2006c). Preparation, thermal performance and application of shape-stabilized PCM in energy efficient buildings. *Energy and Buildings*, 38(10), 1262-1269.

Zhang, Z., Zhang, N., Peng, J., Fang, X., Gao, X., & Fang, Y. (2012c). Preparation and thermal energy storage properties of paraffin/expanded graphite composite phase change material. *Applied Energy*, 91(1), 426-431.

Zhao, C.-Y., Zhou, D., & Wu, Z. (2011). Heat transfer of phase change materials (PCMs) in porous materials. *Frontiers in Energy*, 5(2), 174-180.

Zhong, Y., Zhou, M., Huang, F., Lin, T., & Wan, D. (2013). Effect of graphene aerogel on thermal behavior of phase change materials for thermal management. *Solar Energy Materials and Solar Cells*, 113(0), 195-200.

Zhou, M., Lin, T., Huang, F., Zhong, Y., Wang, Z., Tang, Y., Bi, H., Wan, D., & Lin, J. (2013). Highly conductive porous graphene/ceramic composites for heat transfer and thermal energy storage. *Advanced Functional Materials*, 23(18), 2263-2269.